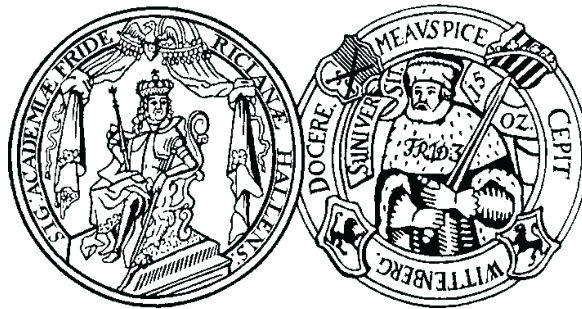# Simulation of the electronic transport through organometallic molecules

Doktorarbeit

zur Erlangung des akademischen Grades
doctor rerum naturalium (Dr. rer. nat.)

vorgelegt der

Institut für Physik
der Naturwissenschaftlichen Fakultät II.
der Martin-Luther-Universität Halle-Wittenberg

von
Volodymyr Maslyuk
geboren am 14. August 1979 in Uzhhorod (Ukraine)

Gutachterin bzw. Gutachter:

1. Prof. Dr. Ingrid Mertig
2. Prof. Dr. Andrei Postnikov
3. PD Dr. Arthur Ernst

Halle/Saale, July 6, 2009

Contents

List of abbreviations

AFM	antiferromagnetism, or antiferromagnetic
ASA	atomic sphere approximation
B3LYP	three-parametric mixture of the Hartree-Fock, Vosko-Wilk-Nusair and Becke exchange and the Lee-Yang-Parr and Vosko-Wilk-Nusair correlation functionals
CA	Ceperley and Alder exchange-correlation functional
DFT	density functional theory
DOS	density of states
DW	domain wall
DZP	double-ζ polarized basis set
EPR	electron paramagnetic resonance
ESR	electron spin resonance
FLAPW	full-potential linearized augmented plane wave
FM	ferromagnetism, or ferromagnetic
FWHM	full width at half maximum
GF	Green's function
GGA	generalized gradient approximation
GTO	Gaussian-type orbital
HOMO	highest occupied molecular orbital
KKR	Korringa-Kohn-Rostoker
LANL2DZ	Los Alamos National Laboratory 2-double-ζ basis set
LCAO	linear combination of atomic orbitals
LDA	local density approximation
LMTO	linear muffin-tin orbital
LUMO	lowest unoccupied molecular orbital
MP2	Møller-Plesset perturbation theory of second order
NEGF	non-equilibrium Green's function
NEXAFS	near-edge X-ray absorption fine structure
PBE	Perdew-Burke-Ernzerhof exchange-correlation functional
PES	photoemission spectroscopy
PW	plane wave
RPES	resonant photoemission spectroscopy
SCF	self-consistent field
SIC	self-interaction correction
SPC	spin polarization of the conductance
STM	scanning tunneling microscopy
STO	Slater-type orbital

TZP   triple-ζ polarized basis set
VBH   von Barth and Hedin exchange-correlation functional
UHV   ultra-high vacuum

1 Introduction

The tremendous development of electronics and semiconductor industries has been amazingly governed by Moore's law, which states that the number of transistors that could be incorporated in a single integrated circuit was rising at a very swift rate. Nowadays, the silicon-based devices are close to insurmountable barriers related to strong influence of quantum effects in forthcoming miniaturization of transistors. One of the ways to overcome this problem is the use of single molecule-based devices, or single molecular wires, to perform signal and information processing. For example, a classical illustration for the possibility of making molecular components with the same functionality as semiconductor devices is the donor-insulator-acceptor molecular diode proposed by Aviram and Ratner in 1974 [1]. On the other hand, the small size of the molecules and the involved quantum effects allows also to think of new logic elements with unforeseen properties.

Therefore, the investigations of electronic transport through nanoscale devices containing only several atoms are becoming one of the most fascinating branches of modern solid state physics. This direction was initialized after the development of the scanning tunnelling microscope (STM) [2] technique, and at present comprises a multitude of applications in physics, chemistry and biology. The theoretical description of the electronic transport in nanoscale systems starts from the famous Kubo [3, 4, 5], Keldysh [6, 7] and Landauer [8, 9] publications. Now, the electronic transport can be successfully described in the framework of the non-equilibrium Green's function (NEGF) method which is based on both the Keldysh [7] and the Landauer-Büttiker [8] formalisms.

The efficient combination of NEGF and density functional theory (DFT) methods is specially designed to simulate the transport characteristics of systems with small numbers of atoms. First principles investigations become very important in physics, chemistry, materials science and biology. The quantum-chemical simulations of molecular and solid systems allow not only to perform a clear interpretation of experimental results, but also help to understand the underlying physical phenomena. In addition, the great theoretical experience in molecular and solid state physics gives the opportunity to search for new phenomena and properties. For example, de Groot et al. [10] introduced the concept of half-metallicity on the basis of band structure calculations in NiMnSb and PtMnSb semi-Heusler phases. Where, due to the ferromagnetic decoupling, one of the spin subbands is metallic, whereas the Fermi level falls into a gap of the other subband. Therefore, it is not surprising that the NEGF+DFT combination shows also amazing result related to simulations of tunnel junctions [11, 12], STM [13] and electron-phonon interactions in molecules and atomic wires [14, 15].

Nowadays, the theoretical and experimental communities pay enormous attention to the fascinating possibility to control the electrical current through manipulation of the spin of the electrons. This spintronic direction in combination with molecular electronics has recently shown spin valves effect in carbon nanotubes [16], large magneto-resistance of octane and tricene molecules [17], molecular spintronic switching [18] and spin-filtering [19, 20]. Nevertheless, it also opens some new questions. In order to manipulate the electron spin in magnetic molecular materials, one has to determine non-collinear magnetic ground states experimentally or theoretically. Moreover, the simulations of the electronic transport characteristics of non-collinear systems need additional resources and techniques.

The *ab initio* calculations of electronic and magnetic properties of non-collinear systems are based on a fully unconstrained approach implemented via the full-potential linearized augmented plane-wave (FLAPW) method [21] or the projector augmented-wave (PAW) method [22] or the linear combination of atomic orbitals (LCAO) method [23]. Unconstrained and constrained non-collinear calculations are also performed within the atomic sphere approximation (ASA) by using a real-space linearized muffin-tin orbital (LMTO) method [24, 25, 26] and the Korringa-Kohn-Rostoker (KKR) method [27, 28, 29]. The last two methods are also successfully applied for electronic transport calculations [30, 31]. Nevertheless, the plane wave (PW) or LCAO based methods have no considerable success in this field. The problem is strongly connected to the absence of the constrained non-collinear procedure which allows to define the direction of the magnetic moment on a given atom. Furthermore, the NEGF method is not generalized for a non-orthogonal basis set and a non-collinear systems with translation invariance.

In this thesis we combine the theoretical development of non-collinear magnetism for the LCAO scheme and NEGF method, and apply the theory to realistic systems. Here we mainly concentrate on organometallic molecules which could be considered as key constituents of molecular spintronics. Namely, we investigate metal-benzene sandwich structures and metallophthalocyanines. Metallophthalocyanines can be successfully grown as ordered films on various substrates and are promising materials for technological applications. The sandwich molecules, in turn, show ferromagnetism and half-metallicity which is extremely interesting from fundamental point of view.

The thesis is divided into two parts. The first one is organized in the second chapter and contains a short introduction to the *ab initio* simulations, explains the main theoretical tools used by the physical and chemical communities. The second part collects our results and is split into four chapters.

In the third chapter, we discuss the fully unconstrained non-collinear LCAO method and introduce a novel on-site constraint method for the nonorthogonal basis set. Our method allows to fix the direction of the magnetic moment on any atom and accelerates the self-consistent field procedure drastically. The theory was successfully implemented in the SIESTA [32, 33, 34] code and applied for investigations of different magnetic configurations in monoatomic Mn and Fe chains and in a Mn_3 molecular cluster.

The fourth chapter is devoted to the extensive study of electronic and magnetic properties of metallophthalocyanines (MetPc, Met=Co,Cu) and metal-benzene (MetBz,

Met=Sc-Co, Bz=C_6H_6) molecules and wires that have potential for applications in the field of spintronics.

In the fifth chapter, we restate and generalize the non-equilibrium Green's function method for non-collinear systems with translation invariance. Additionally, we show the unique procedure how to obtain the components of the transmission spectra for non-collinear systems with arbitrary magnetized electrodes. The generalized NEGF method was applied to perfect and defected graphene layers and monoatomic Fe wire with different magnetization in electrodes.

Finally, the sixth chapter shows transport properties investigation of the organo-metallic wires. We concentrate on $V_n Bz_{n+1}$, $n = 1 - 4$ chains connected to Co(001) electrodes. And we show that the $V_n Bz_{n+1}$, $n \geq 3$ chains can work like spin-filters with 80% polarization of the spin-current. In the end, we analyze the formation of the domain walls in the $V_4 Bz_5$ molecule coupled to cobalt electrodes with antiparallel magnetization.

2 Fundamentals

2.1 Many-body problem

Many problems of condensed matter physics can be solved if the electronic structure of atoms, molecules and solids is determined exactly. The starting point of investigating the electronic properties of the system is to solve the Schrödinger equation.

So, if a quantum system has n electrons and N nuclei with spatial coordinates $\vec{r}$ and $\vec{R}$, respectively, we can write the Schrödinger equation:

$$\mathcal{H}\Phi(\vec{r_1}, ..., \vec{r_n}, \vec{R}_1, ..., \vec{R}_N) = E\Phi(\vec{r_1}, ..., \vec{r_n}, \vec{R}_1, ..., \vec{R}_N), \tag{2.1}$$

where the $\mathcal{H}$ is the Hamiltonian, Ψ is the many-body wave-function and E is a total energy.

The Hamiltonian for the solid system is given by

$$
\begin{aligned}
\mathcal{H} &= T_{ion} + T_{el} + V_{ion-ion} + V_{el-el} + V_{el-ion} \\
&= -\sum_{I=1}^{N} \frac{\hbar^2}{2M_I} \nabla_{\vec{R}_I}^2 - \sum_{i=1}^{n} \frac{\hbar^2}{2m} \nabla_{\vec{r}_i}^2 + \frac{1}{4\pi\epsilon_0} \sum_{I=1}^{N} \sum_{I>I'}^{N} \frac{Z_I Z_{I'}}{|\vec{R}_I - \vec{R}_{I'}|} \\
&\quad + \frac{1}{4\pi\epsilon_0} \sum_{i=1}^{n} \sum_{i'>i}^{n} \frac{e^2}{|\vec{r}_i - \vec{r}_{i'}|} - \frac{1}{4\pi\epsilon_0} \sum_{I=1}^{N} \sum_{i=1}^{n} \frac{Z_I e}{|\vec{r}_i - \vec{R}_I|},
\end{aligned}
\tag{2.2}
$$

where ϵ_0 is the dielectric constant, n, m, e and $\vec{r_i}$ represent the number, mass, charge and position of an electron and N, M_I, Z_I and $\vec{R}_I$ are the number, mass, charge and position of the nuclei.

The first two terms are the kinetic energy contributions from the nuclei (T_{ion}) and the electrons (T_{el}). The last three terms are Coulombic potential energy arising from the ion-ion ($V_{ion-ion}$) and electron-electron (V_{el-el}) repulsions and ion-electron attraction (V_{el-ion}).

Due to a huge number of the particles (about 10^{23} in one cm^3) involved in the interaction, equation (2.1) can not be solved analytically nor numerically up to now. To overcome this problem, different levels of approximations are used. The first one allows to investigate the motion of the electrons independent of that of the nuclei (Born-Oppenheimer approximation). The next is related to the exchange-correlation energy functional representation.

2.2 Born-Oppenheimer approximation

First attempts to introduce simplifications where suggested in 1927. Born and Oppenheimer's mathematical treatment indicated that the true molecular wave function is adequately approximated as $\Phi(\vec{r_i}, \vec{R_I}) = \Psi_{el}(\vec{r_i}, \vec{R_I})\Lambda_{ion}(\vec{R_I})$. The concept behind comes from the fact that the mass of a nucleus is much larger than the mass of an electron ($M \sim 10^3 \times m$) and one can neglect all the quantum effects due to the motion of the nuclei. This assumption breaks the Schrödinger equation down into two sub-equations, one for the electrons and one for the nuclei:

$$[T_{el} + V_{el-el} + V_{el-ion}] \Psi_{el} = \varepsilon_{el}\Psi_{el} \tag{2.3}$$

$$\left[T_{ion} + V_{ion-ion} + \varepsilon_{el}(\{\vec{R_i}\})\right] \Lambda_{ion} = E\Lambda_{ion}, \tag{2.4}$$

where $\varepsilon_{el}(\{\vec{R_I}\})$ is the ground state energy of the electronic cloud for a given nuclear configuration $\{\vec{R_I}\}$. The electronic properties of the system are found by solving the first Schrödinger equation (2.3), where atomic coordinated $\vec{R_I}, I = 1, N$ are involved as parameters. Once it's done, the second equation (2.4) can be used to describe the motion of the nuclei.

However, solving the Schrödinger equation (2.3) is still quite complicated since the many-electron wave-function contains $3n$ variables - $\vec{r_i}$, $i = 1, n$.

2.3 Density functional theory

In the late 1920s, Thomas and Fermi [35, 36] suggested to use the electron density as the central unknown variable instead of the many-electron wave-function. Nevertheless, due to certain shortcomings their method cannot describe the properties of molecules or solids quantitatively. It was only almost forty years later that Hohenberg and Kohn proposed a powerful theory [37] which is based on the original idea of Thomas and Fermi and made a significant progress in the electronic structure theory. They developed a method to determine the ground state density exactly which in turn determines the many body Hamiltonian and therefore all properties of the system. This method is now usually called density functional theory (DFT) and is based on two famous theorems:

1st Hohenberg-Kohn theorem states that a given ground-state electron density cannot arise from two different external potentials, unless the two differ by a constant.

2nd Hohenberg-Kohn theorem states that the ground-state energy can be obtained variationally, the density that minimizes the total energy is than the exact ground-state density.

The density, here, can be defined as:

$$\rho(\vec{r}) = \left\langle \Psi \middle| \sum_{i=1}^{n} \delta(\vec{r} - \vec{r}_i) \middle| \Psi \right\rangle, \qquad (2.5)$$

where Ψ is a many-body wave function. Based on this, the ground state energy is obtained as a functional of the density

$$E[\rho(\vec{r})] = \left\langle \Psi \middle| \mathcal{H}[\rho(\vec{r})] \middle| \Psi \right\rangle = \left\langle \Psi \middle| T_{el}[\rho(\vec{r})] + V_{el-el}[\rho(\vec{r})] + V_{ext}[\rho(\vec{r})] \middle| \Psi \right\rangle. \qquad (2.6)$$

$F[\rho] = T_{el}[\rho] + V_{el-el}[\rho]$ is an universal functional of the electron density. It is the same expression for all systems and independent from the external potential V_{ext} which combines the ion-electron attraction potential V_{el-ion} and the potentials due to external electric and magnetic fields.

The second theorem is of great importance because it leads to a variational principle, which can be used to minimize the energy functional:

$$E[\rho_0(\vec{r})] = \min_{\rho(\vec{r})}(E[\rho(\vec{r})]) \leq E[\rho(\vec{r})], \qquad (2.7)$$

Therefore, the ground state energy can be obtained as follows:

$$\frac{\delta E[\rho(\vec{r})]}{\delta \rho(\vec{r})} - \mu \frac{\delta \left(\int \rho(\vec{r}) d\vec{r} - N \right)}{\delta \rho(\vec{r})} = 0, \qquad (2.8)$$

where μ is a Lagrange multiplier taking care of the particle conservation in the system and usually is referred to as a chemical potential. The important physical conditions which have to be satisfied here are that $\int \rho(\vec{r}) d\vec{r} = N$ and that the electron density is positive $\rho(\vec{r}) \geq 0$.

Solving Eq.(2.8) leads to the following Euler-Lagrange equation:

$$\mu = \frac{\delta E[\rho(\vec{r})]}{\delta \rho(\vec{r})} = V_{ext} + \frac{\delta T[\rho(\vec{r})]}{\delta \rho(\vec{r})} + \frac{\delta V_{el-el}[\rho(\vec{r})]}{\delta \rho(\vec{r})}, \qquad (2.9)$$

where the last two terms are the variation of the universal functional with respect to the density $\rho(\vec{r})$.

The practical application of the density functional theory started after the publication of the Kohn and Sham paper in 1965 [38] by mapping the full interacting system onto a virtual non-interacting system. For this, the kinetic energy functional $T[\rho(\vec{r})]$ is split into a term T reflecting the kinetic energy of noninteracting particles (which is known) and E_c which stands for the rest. A similar procedure applies for the potential energy which contains two terms: the classic part or Coulomb interaction, V_H, and the unknown quantum part E_x. Therefore, the functional $E[\rho(\vec{r})]$ is a sum of known quantities, the kinetic energy T and Coulomb (Hartree) energy E_H, and the unknown E_c and E_x functionals which incorporate all the many-body effects of the original system:

$$E[\rho(\vec{r})] = T[\rho(\vec{r})] + E_H[\rho(\vec{r})] + \int V_{ext}[\rho(\vec{r})]d\vec{r} + E_{xc}[\rho(\vec{r})], \qquad (2.10)$$

where $E_{xc} = E_c + E_x$.

Based on this, the Hamiltonian of the real system is usually termed Kohn-Sham Hamiltonian and is of the form:

$$\mathcal{H}_{KS} = \underbrace{-\frac{\hbar}{2m}\nabla^2}_{T} + \underbrace{\frac{e^2}{2\pi\varepsilon_0}\int\frac{\rho(\vec{r'})d\vec{r'}}{|\vec{r}-\vec{r'}|}}_{V_H} + V_{xc} + V_{ext} \qquad (2.11)$$

where $V_{xc} = \delta E_{xc}[\rho(\vec{r})]/\delta\rho(\vec{r})$ is the exchange-correlation potential.

The Schrödinger equation is then replaced by the Kohn-Sham equation:

$$\mathcal{H}_{KS}\Psi_i(\vec{r}) = \varepsilon_i\Psi_i(\vec{r}), \qquad (2.12)$$

$$\rho(\vec{r}) = \sum_{i=1}^{n}\Psi_i(\vec{r})\Psi_i^*(\vec{r}). \qquad (2.13)$$

Here, $\Psi_i(\vec{r})$ is a single particle wave function and ε_i the corresponding energy eigenvalue.

Since the Kohn-Sham Hamiltonian depends on the density $\rho(\vec{r})$ an iterative procedure can be used

$$\rho_{initial}(\vec{r}) \rightarrow \mathcal{H}_{KS} \rightarrow \{\Psi_i(\vec{r})\} \rightarrow \rho(\vec{r}) \rightarrow \mathcal{H}_{KS} \rightarrow ... \qquad (2.14)$$

to obtain a density which is consistent with the Hamiltonian.

In the case of spin-polarized systems, the original derivation of the Hohenberg-Kohn theorem leads to analytical problems. Von Barth and Hedin [39] showed that the uniqueness of the potential for the same ground state density $\rho(\vec{r})$ is not guaranteed. Capelle and Vignale [40], and Eschrig and Pickett [41] found this nonuniqueness much "richer" than the "rivial" additive constant. Nevertheless, Kohn et al. [42] estimated that the practical consequences for spin-density-functional calculations are not significant. Surprisingly, the Hohenberg-Kohn theorem of unpolarized (charge-only) DFT is thus considerably stronger than its counterpart in spin-DFT.

The generalization of the single-particle equations to spin systems or/and an external magnetic field requires the consideration of the magnetization density as fundamental variable in addition to the electron density:

$$E[\rho_0(\vec{r}), m_0(\vec{r})] = \min_{\rho(\vec{r}), m(\vec{r})}(E[\rho(\vec{r}), m(\vec{r})]) \leq E[\rho(\vec{r}, m(\vec{r}))], \qquad (2.15)$$

The formulation suggested by von Barth and Hedin [39] based on the analogy with the true four component local spin-density matrix:

$$\rho^{\sigma\sigma'}(\vec{r}) = \sum_{i=1}^{n}\Psi_i^{\sigma}(\vec{r})\Psi_i^{\sigma'*}(\vec{r}), \qquad (2.16)$$

where σ or σ' are the indices that define the mixture of the spins in the two component Pauli wave functions $\hat{\Psi}_i(\vec{r})$. Applying this ansatz to the variational principle yields the following Kohn-Sham equations:

$$\sum_{\sigma'} \left(\frac{\hbar}{2m} \nabla^2 \delta^{\sigma\sigma'} + \frac{e^2}{2\pi\varepsilon_0} \int \frac{\rho(\vec{r'})d\vec{r'}}{|\vec{r}-\vec{r'}|} \delta^{\sigma\sigma'} + V_{ext}^{\sigma\sigma'} + \frac{\delta E_{xc}}{\delta\rho^{\sigma\sigma'}(\vec{r})} \right) \Psi_i^{\sigma'}(\vec{r}) = \varepsilon_i \Psi_i^\sigma(\vec{r}), \quad (2.17)$$

where $V_{ext}^{\sigma\sigma'}$ is an external potential including the external magnetic field $\vec{B}(\vec{r})$, $\delta^{\sigma\sigma'}$ is a δ-function and the the exchange-correlation potential $\frac{\delta E_{xc}}{\delta\rho^{\sigma\sigma'}(\vec{r})}$ contains the functional dependence on the magnetization density.

2.3.1 Local density approximation

A first suggestion about the exchange-correlation energy was made by Kohn and Sham in their original paper [38] which than was generalized for spin-polarized systems by von Barth and Hedin [39]. The idea is to approximate E_{xc} by the exchange-correlation energy of a homogeneous electron gas with the same electron and magnetization density:

$$E_{xc}^{LDA}[n(\vec{r}), |\vec{m}(\vec{r})|] = \int n(\vec{r})\epsilon_{xc}\Big(n(\vec{r}), |\vec{m}(\vec{r})|\Big)d\vec{r}, \qquad (2.18)$$

where ϵ_{xc} is the exchange-correlation energy per particle of a homogeneous spin-polarized electron gas and is a function of $n(\vec{r})$ and $\vec{m}(\vec{r})$ at a particular point of space. This means that ϵ_{xc} depends only on the magnitude of the magnetization $|\vec{m}(\vec{r})|$ in every point of space. Therefore, $\vec{V}_{xc}(\vec{r})$ and $\vec{m}(\vec{r})$ are always collinear.
ϵ_{xc} can be obtained by a fitting procedure of data derived from quantum-mechanical many-body calculations. Most commonly used approximations are von Barth and Hedin (VBH) [39], Vosko-Wilk-Nusair (VWN) [43], Ceperley and Alder (CA) [44] and Perdew and Zunger (PZ) [45] parametrizations. Despite its simplicity, LDA provides an accurate enough description, but there are also cases where it fails or shows large discrepancies.

2.3.2 Generalized gradient approximation

It was found that LDA is valid only for systems with density slowly varying in space and fails when the density varies sharply. An improvement to this can be made by considering the gradient of the electron density, the so-called Generalized Gradient Approximation (GGA). Symbolically it can be written as:

$$E_{xc}^{GGA}[n(\vec{r}), \vec{m}(\vec{r})] = \int n(\vec{r})\epsilon_{xc}\Big(n(\vec{r}), \vec{m}(\vec{r}), \nabla n(\vec{r}), \nabla\vec{m}(\vec{r})\Big)d\vec{r}. \qquad (2.19)$$

Many forms of such functionals have been suggested [46, 47, 48, 49, 50, 51, 52]. Practically in all cases, GGA leads to improved bond angles, lengths, and energies but the self-consistent valence electron density in an atom is still too diffuse.

The question of how to improve the exchange-correlation approximation led to two points of view. The first approach retains the correct features of LDA and combines them with the most energetically important features of a gradient-corrected nonlocality. The Perdew, Burke, and Ernzerhof (PBE) functionals [52] are of this type. The second direction assumes that density functional theory is of "semi-empirical" nature. Therefore, a reasonable form of the functional can be developed and the parameters can be fitted to known experimental data. For example, 15 adjustable parameters were refined against data from a test set containing 407 atomic and molecular systems [53]. Another way within this point of view is the construction of hybrid exchange-correlation functionals which are a superposition of different exchange and correlation functionals.

2.3.3 Hybrid schemes

The way to combine different exchange and correlation functionals starts from combination of Becke exchange [50] and Lee-Yang-Parr correlation [51]. It surprised many that this coupling outperformed correlated *ab initio* methods in calculations of atomization energies [54]. In 1992, Becke suggested [55] to construct an exchange-correlation functional as a combination of the Hartree-Fock exchange and DFT-based exchange and correlation functionals by using 3 parameters:

$$E_{xc} = (1-a)(E_x^{VWN} + bE_x^{Becke}) + aE_x^{HF} + (1-c)E_c^{VWN} + cE_c^{LYP}, \qquad (2.20)$$

where a, b and c are semi-empirical coefficients to be determined by an appropriate fit to experimental data, E_x^{HF} is a Hartree-Fock exact exchange and E_x^{VWN} and E_c^{VWN} are a Vosko-Wilk-Nusair exchange and correlation functional, respectively. After several years it became one of the most popular semi-empirical hybrid functionals. Notwithstanding enormous criticism [56], it is now widely used for investigations of organic and organometallic compounds.

Since the construction of the hybrid exchange-correlation functional is just an approximation, one must in the end compare the results of calculations for realistic systems with experimental data.

2.4 Linear combination of the atomic orbitals

One way to solve the Kohn-Sham equations (2.12) is to find a suitable basis set for the expansion of the wave function. In 1928, Finkelstein and Holowitz suggested to describe the molecular orbital of the H_2^+ ion as a linear combination of atomic orbitals. Then, in 1929, Sir John Lennard-Jones used the same technique for the valence-shells of diatomic molecules of the first main row of the periodic table [57]. A generalization of LCAO for spin-polarised many-electron systems was introduced by Roothaan in 1951 [58]. He represented the many-electron wave-function as a linear combination of

a complete set of unknown functions, called basis functions. Thus, for every system we can write:

$$\Psi(\vec{r}) = \sum c_i \chi_i(\vec{r}), \tag{2.21}$$

where $\{\chi_i(\vec{r})\}$ is a complete set of functions and the c_i's are the expansion coefficients that are to be found by the self-consistent field (SCF) procedure. Since the $\{\chi_i(\vec{r})\}$ form a complete set, this expansion is valid. In principle, the expansion of the wave functions should be infinite, but in practice it is truncated.

2.4.1 Slater type of the basis set

One of the first sets of basis functions was introduced by John C. Slater in 1930 [59]. Slater-type orbitals (STO) are of the form:

$$g^{STO}(r) = \frac{(2\zeta/a_0)^{n+1/2}}{[(2n)!]^{1/2}} r^{n-1} e^{-\zeta r/a_0} Y_{lm}(\Theta, \phi), \tag{2.22}$$

where the n, m and l are the quantum numbers, $Y_{lm}(\Theta, \phi)$ are real spherical harmonics, r is the distance of the electron from the atomic nucleus. The parameter ζ is called orbital exponent and is related to the effective charge of the nucleus.

Slater-type orbitals are the most natural basis functions in atomic structure computations because of the hydrogen-like exponentials. Nevertheless, from a computational point of view the STOs have the severe shortcoming that most of the required integrals needed in the course of the SCF procedure must be calculated numerically which drastically decreases the speed of a computation.

2.4.2 Gaussian basis set

Therefore, Boys proposed in 1950 [60] the use of Gaussian-type orbitals (GTO). A cartesian Gaussian orbital centered on an atom μ is defined as:

$$g^{GTO}(r) = N x_\mu^i y_\mu^j z_\mu^k e^{-\alpha r_\mu^2} \quad \text{with} \quad N = \left(\frac{2\alpha}{\pi}\right)^{3/4} \left[\frac{(8\alpha)^{i+j+k} i! j! k!}{(2i)!(2j)!(2k)!}\right], \tag{2.23}$$

where i, j and k are non-negative integers and α is a positive orbital exponent. Note, a cartesian GTO has no principal quantum number n. Any orbital (whether $1s$ or $2s$ or ...) is represented by a linear combination of several Gaussians with different orbital exponent.

An alternative to the cartesian Gaussians are spherical Gaussians, which are of the form:

$$g^{GTO}(r) = N r_\mu^{n-1} e^{-\alpha r_\mu^2} \frac{1}{\sqrt{2}} (Y_l^{m*} \pm Y_l^m), \tag{2.24}$$

where the Y_l^m are complex spherical harmonics.

In comparison to a Slater orbital, a Gaussian function gives a poor representation of atomic orbitals for small values r_μ, therefore it is very important to use a linear

combination of several functions. Consequently, in calculations with GTO's, many more integrals are involved than in a corresponding STO calculation, however evaluation of integrals takes much less computation time. Their essential feature is the fact that a product of two three-dimensional Gaussian functions equals another Gaussian around a shifted center. Thus all three- and four-center two-electron integrals are always reduced to two-center integrals.

2.4.3 Numerical basis set and pseudopotential

Very often, systems with a large number of atoms or electrons have to be treated. In such a case the calculations of the electronic properties takes a lot of time. Sometimes it is reasonable to separate the electrons on every atom into core electrons and valence electrons. Thus, it is possible to evaluate the total energy as the sum of core- and valence-electron energies. This approach, introduced in 1930s, is called the valence-electron approximation.

In the so-called pseudopotential approach the core electrons are decoupled from the rest of the system and substituted by an effective potential, which reproduces the same valence states. The pseudopotential (V_{psI}) for every atom I can be generated individually and then stored and used during the calculations. Consider a system comprising a set of nuclei N. The Kohn-Sham equation (2.17) can be rewritten as:

$$\sum_{\sigma'} \left[\left(\frac{\hbar}{2m} \nabla^2 + \frac{e^2}{2\pi\varepsilon_0} \int \frac{\tilde{\rho}(\vec{r'})d\vec{r'}}{|\vec{r} - \vec{r'}|} + \sum_{I=1}^{N} V_{psI} \right) \delta^{\sigma\sigma'} + V_{ext}^{\sigma\sigma'} + V_{xc}^{\sigma\sigma'}(\vec{r}) \right] \tilde{\Psi}_i^{\sigma'}(\vec{r}) = \tilde{\varepsilon}_i \tilde{\Psi}_i^{\sigma}(\vec{r}),$$

(2.25)

the wave function with a tilde have been introduced to indicate that the SCF solution of these equations is limited to valence electrons.

A very useful approximation is used in the SIESTA [32, 33, 34] package. A combination of norm-conserving pseudopotentials [61] and a numerical basis set allows one to work with huge systems and predict their electronic properties in a very fast way. In comparison to Slater (2.22) and Gaussian (2.23) orbitals, the numerical basis set is extended only up to certain cutoff radii [62] which can be unique for every shell. In this case, the matrices are sparse and small in size, and therefore decrease the time of the calculations. These numerical orbitals, known as pseudo-atomic orbitals, are eigenfunctions of the atomic pseudo-Hamiltonian in a spherical box [62, 63]. Within the so-called "split-valence" method [64], the basis set can be constructed in such ways that one (single-ζ), two (double-ζ) and more orbitals per l quantum channel are used
.

The norm-conserving pseudopotentials are of semi-local form (a different radial potential $V_{Il}(r)$ for each angular momentum l of the atom I). For every atom I potential is transformed into the fully nonlocal form as proposed by Kleinman and Bylander [65]:

$$V_{psI}(r) = V_I^{local}(r) + V_I^{KB}(r) \qquad (2.26)$$

$$V_I^{KB}(r) = \sum_{l=0}^{l_{max}^{KB}} \sum_{m=-l}^{l} \sum_{n=1}^{N_l^{KB}} |\chi_{Ilnm}^{KB}\rangle \epsilon_{Iln}^{KB} \langle \chi_{Ilnm}^{KB}| \qquad (2.27)$$

$$\epsilon_{Iln}^{KB} = \langle \varphi_{Iln}|V_{Il} - V_I^{local}|\varphi_{Iln}\rangle^{-1}, \qquad (2.28)$$

where $V_I^{local}(r)$ and $V_I^{KB}(r)$ are local and non-local potentials, the χ_{Ilnm}^{KB} are the Kleinman-Bylander projectors, which obey the relation

$$\chi_{Ilnm}^{KB}(r) = [V_{Il}(r) - V_I^{local}(r)]\psi_{Ilnm}(r). \qquad (2.29)$$

Atomic pseudo-orbitals $\psi_{Ilnm}(r)$ are the solutions of the radial Schrödinger equation for the potentials $V_{Il}(r)$. Since, $V_{Il}(r) - V_I^{local}(r)$ is zero outside a pseudopotential radius r_I^{core}, the functions $\chi_{Ilnm}^{KB}(r)$ are also zero there. The $V_I^{local}(r)$ can be arbitrary, but must join the semi-local potential $V_{Il}(r)$ beyond the pseudopotential core radius r_I^{core}. In the SIESTA package, the local part of the pseudopotential is optimized for matter of transferability with the scheme suggested by Vanderbilt [66].

It should be noted that the choice of the core radii for the pseudopotential and the cut-off radii for the basis set depend on the system.

3 Non-collinear magnetism in LCAO methods

In magnetically non-collinear system, the direction of the spin is not uniform along an artificially given z axis in spin-space. The Hamiltonian and the density matrix can not be separated into two independent spin-up and spin-down matrices like for a collinear system. In this chapter we derive the Hamiltonian, the overlap matrix and the density matrix for a non-collinear system. We also show the features of a fully unconstrained non-collinear LCAO method and introduce a novel procedure enabling to fix the direction of the magnetic moment on an atom which was implemented in the SIESTA [32, 33, 34] code. However, for our implementation based on the density functional theory, there is no restriction on its usage of our constraint method with the Hartree-Fock level simulation as well. It is known that the density functional and Hartree-Fock schemes are different approaches from the theoretical point of view. But, in practical applications they are profoundly similar. The theory below is written in the general case and is valid for any non-orthogonal basis set.

3.1 Wave function

In non-collinear representation the wave function of the system $\hat{\Psi}_{n\vec{q}}(\vec{r})$ for state n and q-point $\vec{q}$ is a two-component ($\Psi_{n\vec{q}}^{\sigma}(\vec{r})$, $\sigma = \{+, -\}$) spinor [39] and can be written as a linear combination of atomic orbitals or basis functions $\phi_{\mu I_\mu}$ centered on the atomic positions d_μ

$$\hat{\Psi}_{n\vec{q}}(\vec{r}) = \begin{bmatrix} \Psi_{n\vec{q}}^{+}(\vec{r}) \\ \Psi_{n\vec{q}}^{-}(\vec{r}) \end{bmatrix} = \frac{1}{\sqrt{N_u}} \sum_u \sum_{\mu, I_\mu} e^{i\vec{q}(\vec{r}-\vec{R}_u-\vec{d}_\mu)} \hat{c}_{n\vec{q}\mu I_\mu} \phi_{\mu I_\mu}(\vec{r} - \vec{R}_u - \vec{d}_\mu), \qquad (3.1)$$

where $\vec{R}_u$ is the vector between the first unit cell and unit cell u, N_u is the number of unit cells which are taken into account, μ is the index of the atom within one unit cell and I_μ is the index of the basis function situated on an atom μ. The two-component spinors $\hat{c}_{n\vec{q}\mu I_\mu} = \{c_{n\vec{q}\mu I_\mu}^{+}, c_{n\vec{q}\mu I_\mu}^{-}\}$ are the expansion coefficients. In the collinear case this spinor can have only two representations

$$\hat{c}_{n\vec{q}\mu I_\mu}^{+} = \begin{pmatrix} c_{n\vec{q}\mu I_\mu}^{+} \\ 0 \end{pmatrix} \quad \text{or} \quad \hat{c}_{n\vec{q}\mu I_\mu}^{-} = \begin{pmatrix} 0 \\ c_{n\vec{q}\mu I_\mu}^{-} \end{pmatrix}. \qquad (3.2)$$

And, as one can see later, the wave function $\hat{\Psi}_{n\vec{q}}(\vec{r})$ is related to the spin-up state if $\hat{c}_{n\vec{q}\mu I_\mu} = \hat{c}_{n\vec{q}\mu I_\mu}^{+}$, and to the spin-down state if $\hat{c}_{n\vec{q}\mu I_\mu} = \hat{c}_{n\vec{q}\mu I_\mu}^{-}$ for all basis functions μI_μ.

3.2 Density and density matrix

Since each one-electron state in a non-collinear magnet is described with two-component spinor function, the density in every point $\vec{r}$ can be expressed by a 2×2 local spin-density matrix [39]:

$$\hat{\rho}(\vec{r}) = \sum_{n,\vec{q}} f_{n\vec{q}} \hat{\Psi}_{n\vec{q}}(\vec{r}) \otimes \hat{\Psi}^\dagger_{n\vec{q}}(\vec{r}) = \begin{pmatrix} \rho^{11}(\vec{r}) & \rho^{12}(\vec{r}) \\ \rho^{21}(\vec{r}) & \rho^{22}(\vec{r}) \end{pmatrix}, \tag{3.3}$$

where $f_{n\vec{q}} = f(\varepsilon_{n\vec{q}} - \varepsilon_F)$ is the Fermi-Dirac distribution function, which gives the occupation of each state $n\vec{q}$ (ε_F is the Fermi energy), and translational symmetry [34] was taken into account.

The basic difference between collinear and non-collinear magnets is the absence in the non-collinear case of a natural spin-quantization axis common for the whole system. Nevertheless, we can assume that in every point $\vec{r}$ a unitary transformation, $\hat{U}(\vec{r})$, exist, which diagonalize the density matrix locally, i.e.,

$$\begin{pmatrix} \tilde{\rho}^1(\vec{r}) & 0 \\ 0 & \tilde{\rho}^2(\vec{r}) \end{pmatrix} = \hat{U}(\vec{r}) \begin{pmatrix} \rho^{11}(\vec{r}) & \rho^{12}(\vec{r}) \\ \rho^{21}(\vec{r}) & \rho^{22}(\vec{r}) \end{pmatrix} \hat{U}^\dagger(\vec{r}) = \hat{U}(\vec{r})\hat{\rho}(\vec{r})\hat{U}^\dagger(\vec{r}). \tag{3.4}$$

The explicit form of the density matrix can be obtained, if we combine Eq. (3.1) and Eq. (3.3)

$$\begin{aligned} \hat{\rho}(\vec{r}) &= \sum_{\mu I_\mu} \sum_{\nu I_\nu} \sum_u \phi_{I_\mu}(\vec{r} - \vec{d}_\mu) \phi_{I_\nu}(\vec{r} - \vec{R}_u - \vec{d}_\nu) \\ &\quad \times \sum_{n,\vec{q}} e^{-i\vec{q}\cdot(\vec{d}_\mu - \vec{R}_u - \vec{d}_\nu)} f_{n\vec{q}} \left[\hat{c}_{n\vec{q}\mu I_\mu} \otimes \hat{c}^\dagger_{n\vec{q}\nu I_\nu} \right] \\ &= \sum_{\mu,I_\mu} \sum_{\nu,I_\nu} \sum_u \hat{P}_{\mu I_\mu, u\nu I_\nu} \phi_{I_\mu}(\vec{r} - \vec{d}_\mu) \phi_{I_\nu}(\vec{r} - \vec{R}_u - \vec{d}_\nu), \end{aligned} \tag{3.5}$$

where $\hat{P}_{\mu I_\mu, u\nu I_\nu}$ is the element $\mu I_\mu, u\nu I_\nu$ of the density matrix:

$$\hat{P}_{\mu I_\mu, u\nu I_\nu} = \sum_{\vec{q}} \hat{D}_{\vec{q}\mu I_\mu \nu I_\nu} e^{-i\vec{q}\cdot(\vec{d}_\mu - \vec{R}_u - \vec{d}_\nu)}, \quad \text{with} \tag{3.6}$$

$$\begin{aligned} \hat{D}_{\vec{q}\mu I_\mu \nu I_\nu} &= \sum_n f_{n\vec{q}} \hat{c}_{n\vec{q}\mu I_\mu} \otimes \hat{c}^\dagger_{n\vec{q}\nu I_\nu} \\ &= \sum_n f_{n\vec{q}} \begin{pmatrix} c^+_{n\vec{q}\mu I_\mu}(c^+_{n\vec{q}\nu I_\nu})^* & c^+_{n\vec{q}\mu I_\mu}(c^-_{n\vec{q}\nu I_\nu})^* \\ c^-_{n\vec{q}\mu I_\mu}(c^+_{n\vec{q}\nu I_\nu})^* & c^-_{n\vec{q}\mu I_\mu}(c^-_{n\vec{q}\nu I_\nu})^* \end{pmatrix}. \end{aligned} \tag{3.7}$$

Here we introduce a $\vec{q}$-dependent density matrix $\hat{D}_{\vec{q}}$ which does not depend on the phase shift and is quadratic. In case of a molecule calculation $\hat{P}_{\mu I_\mu \nu I_\nu} = \hat{D}_{\mu I_\mu \nu I_\nu}$.

From Eqs. (3.6) and (3.7), one can see that the $\vec{q}$-dependent density matrix $\hat{\mathbf{D}}_{\vec{q}}$ is a Hermitian matrix, but the spin-block $\hat{\mathbf{D}}_{\vec{q}\mu I_\mu \nu I_\nu}$ and, consequently, $\hat{\mathbf{P}}_{\vec{q}\mu I_\mu, u\nu I_\nu}$ are non-Hermitian quantities with respect to the spin-indices (σ and $\sigma' = \{+, -\}$):

$$\mathbf{D}^{\sigma\sigma'}_{\vec{q}\mu I_\mu \nu I_\nu} = \left(\mathbf{D}^{\sigma'\sigma}_{\vec{q}\nu I_\nu \mu I_\mu}\right)^* \tag{3.8}$$

$$\mathbf{D}^{\sigma\sigma'}_{\vec{q}\mu I_\mu \nu I_\nu} \neq \left(\mathbf{D}^{\sigma'\sigma}_{\vec{q}\mu I_\mu \nu I_\nu}\right)^* \quad \Rightarrow \quad \mathbf{P}^{\sigma\sigma'}_{\vec{q}\mu I_\mu, u\nu I_\nu} \neq \left(\mathbf{P}^{\sigma'\sigma}_{\vec{q}\mu I_\mu, u\nu I_\nu}\right)^*. \tag{3.9}$$

3.3 Schrödinger equation

The expectation value of non-relativistic and time-independent Schrödinger operator can be expressed as:

$$\langle \hat{\Psi}_{n\vec{q}} | \hat{\mathcal{H}} | \hat{\Psi}_{n\vec{q}} \rangle = \varepsilon_{n\vec{q}} \langle \hat{\Psi}_{n\vec{q}} | \hat{\Psi}_{n\vec{q}} \rangle, \tag{3.10}$$

where

$$\hat{\mathcal{H}} = \hat{\mathcal{T}} + \hat{V}_H + \hat{V}_{xc} + \hat{V}_{ext} = (\mathcal{T} + V_H)\hat{I} + \hat{V}_{xc} + \hat{V}_{ext} \tag{3.11}$$

is the Hamiltonian of the system, which includes the kinetic energy operator ($\mathcal{T} = -\frac{1}{2}\nabla^2$), the Hartree ($V_H$), exchange-correlation ($\hat{V}_{xc}$) and the external ($\hat{V}_{ext}$) potentials, and $\hat{I}$ is the unit matrix.

Here it should be noted that, in general, we can use the hybrid exchange-correlation potential which contains the mixture of the Hartree-Fock exact exchange with the DFT exchange and correlation potentials. Also, the equation (3.11) can be extended with extra corrections like SIC [67] or LDA+U [68, 69] for strongly correlated electrons or with the spin-orbit interaction [70] term etc. But in all these cases, the potential in every point of the space is a 2×2 matrix and a construction of the non-collinear potential from the local spin-density matrix or from the electron wave functions is an independent problem. In the present work, we consider only the local density and the generalized gradient approximations.

3.3.1 Exchange-correlation potential

It is well known that LDA and GGA functionals do well describe collinear systems, in which the system has a common spin-quantization axis. However, a special procedure is needed for non-collinear exchange-correlation potential calculations.

The LDA functional only needs local information to calculate the exchange and correlation potential. Therefore, at any point we can determine the unitary transformation $\hat{\mathbf{U}}(\vec{r})$ and transform the local spin-density matrix (using the Eq. (3.4)) to the diagonal form where the exchange-correlation potential can be expressed in terms $\delta E_{xc}/\delta\tilde{\rho}^i$, $i = 1, 2$ and follow the standard scheme. Then, we transform the potential back to the global frame. So, in total, the procedure looks like:

$$\hat{\rho}(\vec{r}) \xrightarrow{\hat{\mathbf{U}}(\vec{r})} \tilde{\rho}^1(\vec{r}), \tilde{\rho}^2(\vec{r}) \rightarrow \text{diag}\{\tilde{V}_{xc}[\tilde{\rho}^1(\vec{r}), \tilde{\rho}^2(\vec{r})]\} \xrightarrow{\hat{\mathbf{U}}^\dagger(\vec{r})} \hat{V}_{xc}(\vec{r}). \tag{3.12}$$

In case of GGA the procedure is slightly complicated due to the functional dependence on the gradient of the electron spin-density $\nabla \hat{\rho}(\vec{r})$. In our case, we use the procedure suggested by García-Suárez and co-workers [73]. Here, we have to mention, that it is equivalent to the Knöpfle and co-workers' implementation [74]. So, the local spin-density at a given $\vec{r}$ and $\vec{r} + \vec{dr}$ points are transformed to the local diagonal form by using the same transformation matrix $\hat{\mathbf{U}}(\vec{r})$. Here, the assumption was made that the transformation matrices which diagonalize the local spin-density at point $\vec{r}$ and all points around are very similar. Then, we compute the gradients $\nabla \tilde{\rho}^1(\vec{r})$ and $\nabla \tilde{\rho}^2(\vec{r})$ and the collinear exchange-correlation potential $\tilde{V}_{xc}^1$ and $\hat{V}_{xc}^2$. And, finally, we transform the potential back to the global frame. In general, we can present the procedure as:

$$
\begin{aligned}
\hat{\rho}(\vec{r}), \hat{\rho}(\vec{r} + \vec{dr}) \quad &\xrightarrow{\hat{\mathbf{U}}(\vec{r})} \quad \tilde{\rho}^1(\vec{r}), \tilde{\rho}^2(\vec{r}), \tilde{\rho}^1(\vec{r} + \vec{dr}), \tilde{\rho}^2(\vec{r} + \vec{dr}) \\
&\rightarrow \quad \tilde{\rho}^1(\vec{r}), \tilde{\rho}^2(\vec{r}), \nabla \tilde{\rho}^1(\vec{r}), \nabla \tilde{\rho}^2(\vec{r}) \\
&\rightarrow \quad \mathrm{diag}\{\hat{V}_{xc}[\tilde{\rho}^1(\vec{r}), \tilde{\rho}^2(\vec{r}), \nabla \tilde{\rho}^1(\vec{r}), \nabla \tilde{\rho}^2(\vec{r})]\} \\
&\xrightarrow{\hat{\mathbf{U}}^{\dagger}(\vec{r})} \quad \hat{V}_{xc}(\vec{r}).
\end{aligned}
\tag{3.13}
$$

Alternatively, following the Kübler *et al.* [71, 72] notations, we can identify $\hat{\mathbf{U}}$ with the spin-$\frac{1}{2}$ rotation matrix

$$
\hat{\mathbf{U}}(\vec{r}) = \hat{\mathbf{U}}(\theta(\vec{r}), \varphi(\vec{r})) = \begin{pmatrix} \cos(\frac{\theta(\vec{r})}{2}) \exp(\frac{i\varphi(\vec{r})}{2}) & \sin(\frac{\theta(\vec{r})}{2}) \exp(-\frac{i\varphi(\vec{r})}{2}) \\ -\sin(\frac{\theta(\vec{r})}{2}) \exp(\frac{i\varphi(\vec{r})}{2}) & \cos(\frac{\theta(\vec{r})}{2}) \exp(-\frac{i\varphi(\vec{r})}{2}) \end{pmatrix}.
\tag{3.14}
$$

In such case, using Eq. (3.4), the local spin-density matrix is equal

$$
\hat{\rho}(\vec{r}) = \left[\tilde{\rho}^1(\vec{r}) + \tilde{\rho}^2(\vec{r})\right] \hat{I} + \left[\tilde{\rho}^1(\vec{r}) - \tilde{\rho}^2(\vec{r})\right] \hat{\sigma}_z'(\vec{r})
\tag{3.15}
$$

and the single-particle exchange-correlation potential matrix can be written in the form

$$
\hat{V}_{xc}(\vec{r}) = V_{xc}^0(\vec{r}) \hat{I} + \Delta V_{xc}^0(\vec{r}) \hat{\sigma}_z'(\vec{r}),
\tag{3.16}
$$

where $\hat{\sigma}_z'(\vec{r})$ is the z-component of the Pauli spin matrix in a coordinate system which is rotated by the polar angles $\theta(\vec{r})$ and $\varphi(\vec{r})$ with respect to the global coordinate system

$$
\hat{\sigma}_z'(\vec{r}) = \begin{pmatrix} \cos[\theta(\vec{r})] & \sin[\theta(\vec{r})] e^{-i\varphi(\vec{r})} \\ \sin[\theta(\vec{r})] e^{i\varphi(\vec{r})} & -\cos[\theta(\vec{r})] \end{pmatrix}.
\tag{3.17}
$$

$\hat{I}$ is a unit 2×2 matrix and the potentials $V_{xc}^0(\vec{r})$ and $\Delta V_{xc}^0(\vec{r})$ are given as

$$
V_{xc}^0(\vec{r}) = \frac{1}{2}\left[\frac{\delta E_{xc}}{\delta \tilde{\rho}^1} + \frac{\delta E_{xc}}{\delta \tilde{\rho}^2}\right] \quad \text{and} \quad \Delta V_{xc}^0(\vec{r}) = \frac{1}{2}\left[\frac{\delta E_{xc}}{\delta \tilde{\rho}^1} - \frac{\delta E_{xc}}{\delta \tilde{\rho}^2}\right].
\tag{3.18}
$$

Now, taking into account that the sum in the first brackets of the Eq.(3.15) is a local charge density $n(\vec{r})$ and the difference in the second brackets corresponds to the magnetization density $m(\vec{r})$, in the local coordinate system we can rewrite the expression for the spin-density matrix by using the Pauli spin matrices $\hat{\sigma}_i$, $i = x, y, z$
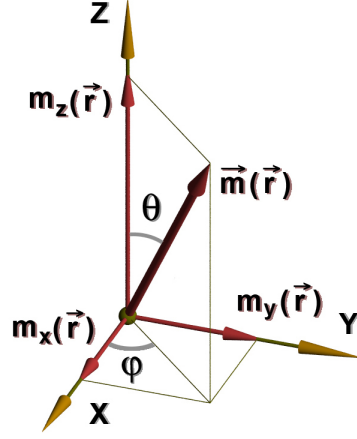
Figure 3.1: The local magnetic density vector $\vec{m}(\vec{r})$ can be defined in terms of $\theta = \theta(\vec{r})$ and $\varphi = \varphi(\vec{r})$ polar angles and its Cartesian components $m_x(\vec{r})$, $m_y(\vec{r})$ and $m_z(\vec{r})$.

$$\rho(\vec{r}) = \frac{1}{2}\hat{I} \cdot n(\vec{r}) + \frac{1}{2}\sum_{k=x,y,z}\vec{\sigma}_k \cdot \vec{m}(\vec{r}) = \frac{1}{2}\begin{pmatrix} n(\vec{r}) + m_z(\vec{r}) & m_x(\vec{r}) - im_y(\vec{r}) \\ m_x(\vec{r}) + im_y(\vec{r}) & n(\vec{r}) - m_z(\vec{r}) \end{pmatrix}. \quad (3.19)$$

Here, we introduced the Cartesian components (see Fig. 3.1) $m_x(\vec{r})$, $m_y(\vec{r})$ and $m_z(\vec{r})$ of the local magnetization density vector $\vec{m}(\vec{r})$ in the global coordinate system:

$$
\begin{aligned}
m_x(\vec{r}) &= m(\vec{r})\sin[\theta(\vec{r})]\cos[\varphi(\vec{r})] & (3.20) \\
m_y(\vec{r}) &= m(\vec{r})\sin[\theta(\vec{r})]\sin[\varphi(\vec{r})] & (3.21) \\
m_z(\vec{r}) &= m(\vec{r})\cos[\theta(\vec{r})]. & (3.22)
\end{aligned}
$$

3.3.2 Hamilton and overlap matrices

The Hamilton $\hat{\mathbf{H}}_{\vec{q}}$ and the overlap $\hat{\mathbf{S}}_{\vec{q}}$ matrices can be obtained from Eq.(3.10) if we rewrite it by using the wave function expression (3.1):

$$\sum_{\mu I_\mu \nu I_\nu} \hat{c}^\dagger_{n\vec{q}\mu I_\mu} \hat{\mathbf{H}}_{\vec{q}\mu I_\mu \nu I_\nu} \hat{c}_{n\vec{q}\nu I_\nu} = \varepsilon_{n\vec{q}} \sum_{\mu I_\mu \nu I_\nu} \hat{c}^\dagger_{n\vec{q}\mu I_\mu} \hat{\mathbf{S}}_{\vec{q}\mu I_\mu \nu I_\nu} \hat{c}_{n\vec{q}\nu I_\nu}, \quad \text{or} \quad (3.23)$$

$$\sum_{\mu I_\mu} \hat{c}^\dagger_{n\vec{q}\mu I_\mu} \left[\sum_{\nu I_\nu} \left(\hat{\mathbf{H}}_{\vec{q}\mu I_\mu \nu I_\nu} - \varepsilon_{n\vec{q}} \hat{\mathbf{S}}_{\vec{q}\mu I_\mu \nu I_\nu} \right) \hat{c}_{n\vec{q}\nu I_\nu} \right] = 0. \quad (3.24)$$

Here

$$\hat{\mathbf{H}}_{\vec{q}\mu I_\mu \nu I_\nu} = \sum_u e^{-i\vec{q}(\vec{d}_\mu - \vec{R}_u - \vec{d}_\nu)} \hat{\mathbf{H}}_{\mu I_\mu, u\nu I_\nu}, \tag{3.25}$$

$$\hat{\mathbf{S}}_{\vec{q}\mu I_\mu \nu I_\nu} = \sum_u e^{-i\vec{q}(\vec{d}_\mu - \vec{R}_u - \vec{d}_\nu)} \hat{\mathbf{S}}_{\mu I_\mu, u\nu I_\nu}, \quad \text{with} \tag{3.26}$$

$$\mathbf{H}^{\sigma\sigma'}_{\mu I_\mu, u\nu I_\nu} = \langle \phi_{\mu I_\mu} | (\mathbf{T} + V_H + V_{ext}) \delta^{\sigma\sigma'} + V^{\sigma\sigma'}_{xc} | \phi_{u\nu I_\nu} \rangle, \tag{3.27}$$

$$\mathbf{S}^{\sigma\sigma'}_{\mu I_\mu, u\nu I_\nu} = \langle \phi_{\mu I_\mu} | \delta^{\sigma\sigma'} | \phi_{u\nu I_\nu} \rangle, \tag{3.28}$$

where $\delta^{\sigma\sigma'}$ is the Kronecker's delta and

$$\phi_{\mu I_\mu} = \phi_{\mu I_\mu}(\vec{r} - \vec{d}_\mu), \qquad \phi_{u\nu I_\nu} = \phi_{\nu I_\nu}(\vec{r} - \vec{R}_u - \vec{d}_\nu). \tag{3.29}$$

Finally, for every $\vec{q}$ point we have a set of equations:

$$\sum_{\nu I_\nu} \left(\hat{\mathbf{H}}_{\vec{q}\mu I_\mu \nu I_\nu} - \varepsilon_{n\vec{q}} \hat{\mathbf{S}}_{\vec{q}\mu I_\mu \nu I_\nu} \right) \hat{c}_{n\vec{q}\nu I_\nu} = 0. \tag{3.30}$$

Note, that if the exchange-correlation potential $\hat{V}_{xc}$ is spin-diagonal in every point of space (i.e. the system has a common spin-quantization axis), the solution of the Schödinger equation (3.30) can be found from two independent equations

$$\sum_{\nu I_\nu} \left(\mathbf{H}^\sigma_{\vec{q}\mu I_\mu \nu I_\nu} - \varepsilon^\sigma_{n\vec{q}} \mathbf{S}^\sigma_{\vec{q}\mu I_\mu \nu I_\nu} \right) c^\sigma_{n\vec{q}\nu I_\nu} = 0 \tag{3.31}$$

which describe "spin-up" electrons with $\sigma = +$ and "spin-down" electrons with $\sigma = -$. Here, the eigenvalues $\varepsilon^\sigma_{n\vec{q}}$ and eigenvectors $c^\sigma_{n\vec{q}\nu I_\nu}$ are related only to the certain spin-direction $\sigma = \{+, -\}$.

3.4 Fully unconstrained non-collinear magnetism in the LCAO method

Up to this point, no approximations were made. The local spin-density and the potential of the system have spatial variation of spin directions, and we have imposed no constraints like in those methods based on an atomic sphere approximation for the crystal potential [24, 25, 29]. Taking into account that the non-collinear LCAO is a full-potential method, we can easily combine it with the relaxation or *ab initio* molecular dynamics tasks, making it a promising tool for investigations of magnetic systems from first principles.

An extra feature of the unconstrained non-collinear LCAO method, which was not mentioned in literature before, is related to the spin orientational degree of freedom for every atomic orbital. The atomic orbitals in the collinear system have one common magnetization direction, and they can look either "up" or "down". In the non-collinear
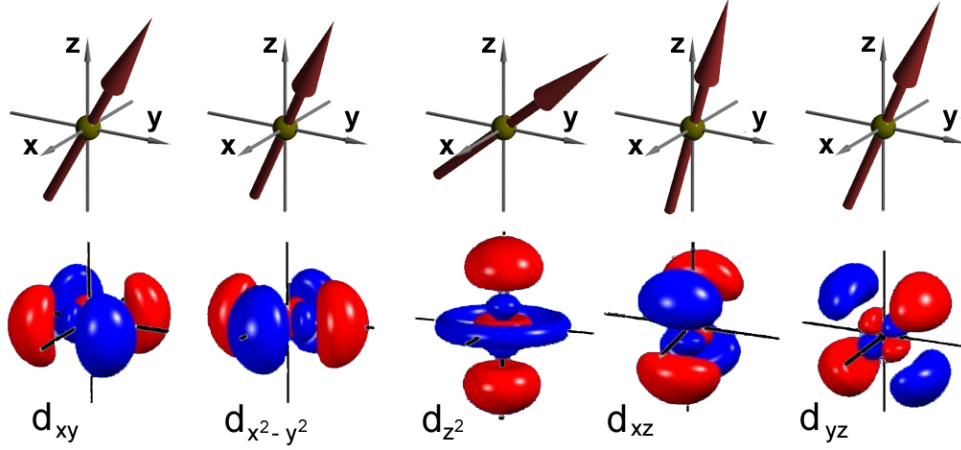
Figure 3.2: Fully unconstrained LCAO method allows to have different magnetization axis for every atomic orbital.

case, every atomic orbital can have an arbitrary magnetization direction (see Fig. 3.2). Moreover, there is no restriction to have different quantization axes for different basis functions μI_μ for every $n\vec{q}$ state, because the expansion coefficients $\hat{c}_{n\vec{q}\mu I_\mu}$ are, in general, arbitrary spinors, and their product $\hat{c}_{n\vec{q}\mu I_\mu} \otimes \hat{c}^\dagger_{n\vec{q}\mu I_\mu}$ can yield an arbitrary magnetization direction. The physical meaning of the off-diagonal element of the density matrix $\hat{\mathbf{P}}_{u\mu I_\mu \nu I_\nu}$ is not clear. In a collinear system they are responsible for the charge and magnetic moment situated in the overlap region between basis functions $\phi_{I_\mu}(\vec{r} - \vec{d_\mu})$ and $\phi_{I_\nu}(\vec{r} - \vec{R_u} - \vec{d_\nu})$. But for a non-collinear system, $\hat{\mathbf{P}}_{u\mu I_\mu \nu I_\nu}$ is not a Hermitian quantity [see Eqs. (3.7) and (3.9)], therefore it cannot correspond to the charge and magnetic moment in the same manner.

Finally, despite the absence of approximations, the method has restrictions related to the impossibility to fix the direction of the magnetic moment per atom. Moreover, the definition of magnetic moments on the atom is not clear, in comparison to LMTO or KKR methods. Therefore, we can summarize the main problems of the fully unconstrained non-colliner LCAO method

a) the magnetic moment on the atom is ambiguous;

b) as a consequence, it is impossible to fix the direction of the magnetic moment per atom;

c) therefore, it is not clear how to use the method for the treatment of spin excitations;

d) the method is very time consuming.

The last problem is related to a lack of efficient mixing scheme during the self-consistent procedure. The local spin-density matrix at every point $\vec{r}$ of the SCF step N is mixed with the density matrices from the previous steps $N-1$, $N-2$,... with very small

mixing weight (which is standart for magnetic systems). This, as a result, implies a small variation of the direction of the local magnetic moment $\vec{m}(\vec{r})$ from one SCF iteration to another, and consequently very many iterations are needed to rotate the local density in the spin space toward the converged result.

3.5 On-site constraint for the non-collinear LCAO method

There is no unique definition of "atomic charge" or "atomic magnetic moment" in a molecule or in a solid, even when the accurate wave functions are obtained. Many numerous schemes were proposed to attribute a part of the electron density to individual atoms, but none of them can satisfy the wide class of systems. Formally, we can separate these schemes into two groups: (a) partitioning of the space around the atomic sites and analysis of the electron distribution over these finite volumes, and (b) manipulations with basis functions or density matrices.

To the first set belong the approximations based on a spherical potential [26, 27, 28] and Bader partitioning scheme [83, 84]. In both cases the volume of the atom is defined in an individual way (depends on the scheme), and the charge or magnetic moment of the atom results from integration of the electronic spin-density over this volume. Despite the simplicity of the approach, a problem arises of ambiguous volume definition. The second group contains different types of orbital population analyses.

The one of the first population analyses was developed by Mulliken [85, 86]. It uses the fact that the basis functions that span the one-electron orbital space are normally atom centered functions, which enable the assignment of electrons to atoms. According to Mulliken's formulation, the charge related to the basis function μ can be defined in terms of the density matrix $D_{\mu\nu}$ and the overlap matrix $S_{\mu\nu}$ as

$$Q_\mu = D_{\mu\mu}S_{\mu\mu} + \frac{1}{2}\sum_{\nu\neq\mu}\left(D_{\mu\nu}S_{\mu\nu} + D_{\nu\mu}S_{\nu\mu}\right). \tag{3.32}$$

It is the so-called gross Mulliken population which means that every basis function μ gives the charge that equals the net population (first term) plus one-half of the overlap populations between this function and all other basis functions (second term). The simple formulation and easy application for molecules and crystals maked it widespread. Unfortunately, as has been repeatedly mentioned in the literature [86], the Mulliken analysis varies drastically with the basis set and shows no convergence as the size of the basis set is increased. The reason of these problems stems from different partitioning of the space because of the modified overlap matrix when using different basis functions. Nevertheless, up to now, no better scheme for the systems with translation invariance has been found. If one wants to use the Löwdin [87] scheme or natural atomic populations [88], etc, one has to take into account the $\vec{q}$ dependence of the density and overlap matrices which makes the application of these methods very difficult and computationally expensive. Therefore, we will concentrate on the Mulliken

population analysis, assuming that deficiency of the non-orthogonality of the basis set could be solved in an other way, for example with the LoProp [89] method or with Distributed Multipole Analysis [90].

First, we rewrite Eq. (3.32) for periodic systems with non-collinear magnetization by using the $\vec{q}$-dependent density matrix (3.7) and overlap matrix (3.26):

$$
\hat{\mathbf{Q}}_{\mu I_\mu} = \sum_{\vec{q}} \left[\hat{\mathbf{D}}_{\vec{q}\mu I_\mu \mu I_\mu} \hat{\mathbf{S}}_{\vec{q}\mu I_\mu \mu I_\mu} + \frac{1}{2} \sum_{\nu I_\nu \neq \mu I_\mu} \left(\hat{\mathbf{D}}_{\vec{q}\mu I_\mu \nu I_\nu} \hat{\mathbf{S}}_{\vec{q}\mu I_\mu \nu I_\nu} + \hat{\mathbf{D}}_{\vec{q}\nu I_\nu \mu I_\mu} \hat{\mathbf{S}}_{\vec{q}\nu I_\nu \mu I_\mu} \right) \right] .
$$

One can see that $\hat{\mathbf{Q}}_{\mu I_\mu}$ is a Hermitian matrix, and we always can assume that there is a unitary transformation $\hat{\mathbf{U}}_{\mu I_\mu}$ which can diagonalize it. Therefore, in analogy to the local spin-density matrix $\hat{\rho}(\vec{r})$ we can write

$$
\hat{\mathbf{Q}}_{\mu I_\mu} = \hat{\mathbf{U}}^\dagger_{\mu I_\mu} \begin{pmatrix} n+m & 0 \\ 0 & n-m \end{pmatrix}_{\mu I_\mu} \hat{\mathbf{U}}_{\mu I_\mu} = \begin{pmatrix} n+m_z & m_x - im_y \\ m_x + im_y & n - m_z \end{pmatrix}_{\mu I_\mu} , \quad (3.33)
$$

where n and m are the charge and magnetization density related to the basis function μI_μ in the local coordinate system and m_x, m_y and m_z are the components of the magnetization density vector $\vec{m}$ of the same basis function in the global coordinate system.

It is reasonable to be closer to the Mulliken formulation and construct the density matrix in the way that every element describes the electronic charge and the magnetization vector related to the overlap region between the basis functions μI_μ and $u\nu I_\nu$. Thus, taking into account that the overlap matrix element $\hat{\mathbf{S}}_{\mu I_\mu, u\nu I_\nu}$ is equal to $\hat{\mathbf{S}}_{\nu I_\nu, u\mu I_\mu}$ (equivalence by translation [34] must be considered) we can define the new density matrix in the way that

$$
\hat{\mathbf{Q}}_{\mu I_\mu} = \sum_u \sum_{\nu I_\nu} \hat{\tilde{\mathbf{P}}}_{\mu I_\mu, u\nu I_\nu} \hat{\mathbf{S}}_{\mu I_\mu, u\nu I_\nu}, \quad \text{where} \tag{3.34}
$$

$$
\hat{\tilde{\mathbf{P}}}_{\mu I_\mu, u\nu I_\nu} = \frac{1}{2} \sum_{\vec{q}} \left[\hat{\mathbf{D}}_{\vec{q}\mu I_\mu \nu I_\nu} e^{-i\vec{q}\cdot(\vec{d}_\mu - \vec{R}_u - \vec{d}_\nu)} + \hat{\mathbf{D}}_{\vec{q}\nu I_\nu \mu I_\mu} e^{-i\vec{q}\cdot(\vec{d}_\nu + \vec{R}_u - \vec{d}_\mu)} \right], \tag{3.35}
$$

and taking into account that $\hat{\mathbf{D}}_{\vec{q}}$ of Eq. (3.8) is hermitian,

$$
\tilde{\mathbf{P}}^{\sigma\sigma'}_{\mu I_\mu, u\nu I_\nu} = \frac{1}{2} \sum_{\vec{q}} \left[\mathbf{D}^{\sigma\sigma'}_{\vec{q}\mu I_\mu \nu I_\nu} e^{-i\vec{q}\cdot(\vec{d}_\mu - \vec{R}_u - \vec{d}_\nu)} + \left(\mathbf{D}^{\sigma'\sigma}_{\vec{q}\mu I_\mu \nu I_\nu} e^{-i\vec{q}\cdot(\vec{d}_\mu - \vec{R}_u - \vec{d}_\nu)} \right)^* \right]
$$

$$
= \frac{1}{2} \left[\mathbf{P}^{\sigma\sigma'}_{\mu I_\mu, u\nu I_\nu} + \left(\mathbf{P}^{\sigma'\sigma}_{\mu I_\mu, u\nu I_\nu} \right)^* \right] = \left(\tilde{\mathbf{P}}^{\sigma'\sigma}_{\mu I_\mu, u\nu I_\nu} \right)^* . \tag{3.36}
$$

In this case, the local spin-density $\hat{\rho}(\vec{r})$ can be determined via the new density matrix

$$\hat{\rho}(\vec{r}) \;=\; \sum_{\mu I_\mu} \sum_{\nu I_\nu} \sum_u \hat{\tilde{\mathbf{P}}}_{\mu I_\mu, u\nu I_\nu} \phi_{I_\mu}(\vec{r} - \vec{d}_\mu) \phi_{I_\nu}(\vec{r} - \vec{R}_u - \vec{d}_\nu),$$

$$=\; \sum_{\mu I_\mu} \sum_{\nu I_\nu} \sum_u \hat{\rho}_{\mu I_\mu, u\nu I_\nu}(\vec{r}), \qquad (3.37)$$

where $\hat{\rho}_{\mu I_\mu, u\nu I_\nu}(\vec{r})$ is the local spin-density related to the overlap between basis functions μI_μ and $u\nu I_\nu$

Up to now, no assumption was made and we are still working on the level of the fully unconstrained non-collinear LCAO. The magnetization direction of the local spin-density matrix $\hat{\rho}(\vec{r})$ can be different in every point of space and defined by the superposition of the local spin-densities $\hat{\rho}_{\mu I_\mu, u\nu I_\nu}(\vec{r})$, which, individually, have a magnetization axis defined by the $\hat{\tilde{\mathbf{P}}}_{\mu I_\mu, u\nu I_\nu}$.

Now, taking into account that the main contribution to the charge and magnetic moment of the atom μ stems from the atomic block of the density matrix, we can define our on-site constraint for the non-collinear LCAO method. It is based on two assumptions:

1) all elements of the density matrix $\hat{\tilde{\mathbf{P}}}_{\mu I_\mu, u\nu I_\nu}$ related to the site μ and all its transitionary invariant replicas have a common magnetization direction;

2) off-diagonal elements of the density matrix related to the overlap between sites μ and ν ($\nu \neq \mu$) have a magnetization direction which is in the plane created by the magnetic moments related to atomic blocks μ and ν.

The first statement is very close to the constraint in methods with spherical potential where the magnetization direction is common for the whole sphere [26, 29]. So, we can find the magnetic moment $\vec{m}_{\mu'} = (m_x, m_y, m_z)_{\mu'}$ and its direction $(\Theta_{\mu'}, \varphi_{\mu'})$ for atomic blocks related to the site μ including all equivalent atoms due to translations:

$$\hat{\mathbf{Q}}_{\mu'} = \begin{pmatrix} n + m_z & m_x - im_y \\ m_x + im_y & n - m_z \end{pmatrix}_{\mu'} = \sum_u \sum_{\substack{\mu I_\mu \nu I_\nu \\ \mu = \nu}} \hat{\tilde{\mathbf{P}}}_{\mu I_\mu, u\nu I_\nu} \hat{\mathbf{S}}_{\mu I_\mu, u\nu I_\nu} \qquad (3.38)$$

$$\cos(\Theta_{\mu'}) \;=\; \frac{m_z}{\sqrt{m_x^2 + m_y^2 + m_z^2}} \qquad (3.39)$$

$$\cos(\varphi_{\mu'}) \;=\; \frac{m_x}{\sqrt{m_x^2 + m_y^2}}. \qquad (3.40)$$

Note, we use the prime in order to distinguish among the matrix $\hat{\mathbf{Q}}_{\mu'}$ related to the atomic block of the atom μ and matrix $\hat{\mathbf{Q}}_\mu$ describing the electronic charge and the magnetic moment related to the atom μ

$$\hat{\mathbf{Q}}_\mu \;=\; \sum_u \sum_{\mu I_\mu \nu I_\nu} \hat{\tilde{\mathbf{P}}}_{\mu I_\mu, u\nu I_\nu} \hat{\mathbf{S}}_{\mu I_\mu, u\nu I_\nu}. \qquad (3.41)$$

Then, we can transform every element of the density matrix related to the site μ ($\nu = \mu$) to the local frame and drop off-diagonal elements:

$$\hat{\tilde{\mathbf{P}}}_{\mu I_\mu, u\nu I_\nu} = \hat{\mathbf{U}}^\dagger(\theta_{\mu'}, \varphi_{\mu'}) \begin{pmatrix} \tilde{\mathbf{P}}^+_{\mu I_\mu, u\nu I_\nu} & \delta \\ \delta^\dagger & \tilde{\mathbf{P}}^-_{\mu I_\mu, u\nu I_\nu} \end{pmatrix} \hat{\mathbf{U}}(\theta_{\mu'}, \varphi_{\mu'}) \qquad (3.42)$$

$$= \hat{\mathbf{U}}^\dagger(\theta_{\mu'}, \varphi_{\mu'}) \begin{pmatrix} \tilde{\mathbf{P}}^+_{\mu I_\mu, u\nu I_\nu} & 0 \\ 0 & \tilde{\mathbf{P}}^-_{\mu I_\mu, u\nu I_\nu} \end{pmatrix} \hat{\mathbf{U}}(\theta_{\mu'}, \varphi_{\mu'}). \qquad (3.43)$$

With the second assumption, we try to avoid the "memory" effect in the density matrix. It doesn't make sense for small systems, like two atomic molecule. But, for systems where the spiral state is the ground state and for large systems it could be important.

3.6 Application of the on-site constraint non-collinear LCAO method

The on-site constraint was successfully implemented in the SIESTA code. Optionally, we allow

- to switch between fully unconstrained and constrained non-collinear calculations;

- to fix the direction of the magnetic moment for any site μ;

- to have different mixing weights $w_{density}$ for the density matrix in the local frame and w_{angles} for the angles (Θ_μ, φ_μ) determining the magnetization directions on every site μ;

- to have different convergence criteria for the density matrix elements ($\hat{\tilde{\mathbf{P}}}_{\mu I_\mu, u\nu I_\nu}$) and for the angles ($\Theta_\mu$, φ_μ).

After the implementations, comprehensive tests were performed. The first verification criteria was based on the reproduction of any spin-polarized calculations for different systems (clusters, surfaces and bulks). Then, we proved that the system is invariant with respect to rotations in spin space. Here, identical results where obtained for any uniform rotation $\hat{\mathbf{U}}$ applied to the system with arbitrary angles Θ and φ. Technically, every step of the SCF procedure was verified along the path

$$\hat{\mathbf{U}}\hat{\rho}(\vec{r})\hat{\mathbf{U}}^\dagger \xrightarrow{Eqs.(3.25),(3.27)} \{\hat{\mathbf{U}}\hat{\mathbf{H}}_{\vec{q}\mu I_\mu \nu I_\nu}\hat{\mathbf{U}}^\dagger\} \xrightarrow{Eq.(3.24)} \{\varepsilon_{n\vec{q}}\}, \{\hat{\mathbf{U}}^\dagger \hat{c}_{n\vec{q}\mu I_\mu}\}$$
$$\xrightarrow{Eqs.(3.7),(3.36)} \{\hat{\mathbf{U}}\hat{\tilde{\mathbf{P}}}_{\mu I_\mu, u\nu I_\nu}\hat{\mathbf{U}}^\dagger\} \xrightarrow{Eq.(3.37)} \hat{\mathbf{U}}\hat{\rho}(\vec{r})\hat{\mathbf{U}}^\dagger, \qquad (3.44)$$

where $\varepsilon_{n\vec{q}}$ and $\hat{c}_{n\vec{q}\mu I_\mu}$ are the eigenvalues and eigenvectors of the initial system. In the end, we use our on-site constraint method for monoatomic Fe and Mn nanowires and three-atomic Mn cluster.
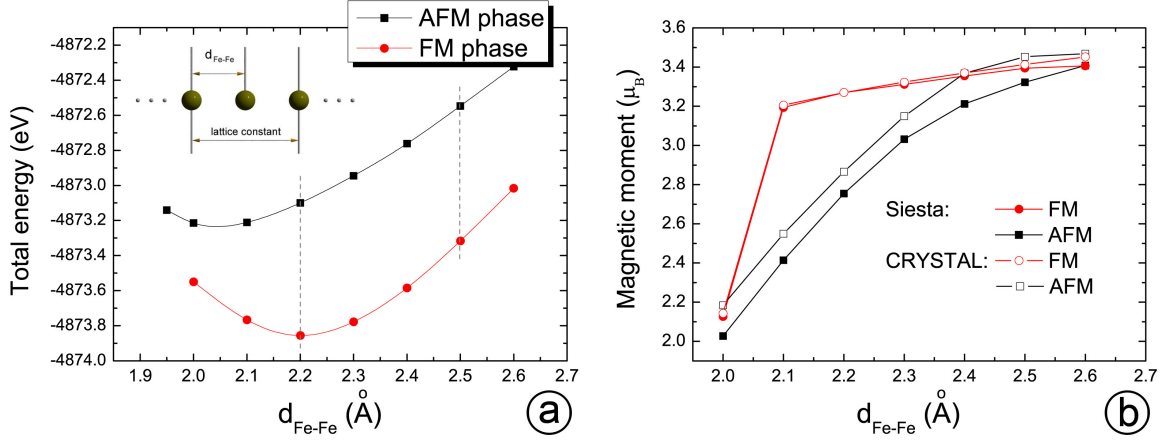
Figure 3.3: (a) Total energy of the monoatomic Fe chain as a function of the Fe-Fe interatomic distance. The red line corresponds to the FM phase and the black line refers to the AFM phase. (b) Dependence of the iron atom magnetic moment from the Fe-Fe bond length for FM and AFM phases. CRYSTAL (FM - line with open circles and AFM - line with open squares) and SIESTA (FM - line with solid circles and AFM - line with solid squares) calculations.

3.6.1 1D chains

The choice of iron and manganese chains was based on their different phases in the ground state. As you can see later, the iron nanowire is a one-dimensional ferromagnet (FM) and the manganese wire is an antiferromagnet (AFM).

The investigation of infinite ideal monoatomic chains were performed by using the LDA scheme with Ceperley-Alder [44] parametrization for electron exchange and correlation. The pseudopotentials for atomic elements were generated according to the procedure of Troullier and Martins [75] with $3p$ semicore states. The electronic configurations and the cutoff radii (in a.u.), in the $s/p/d/f$ order are $3p^6 4s^1 3d^7 4f^0$ and $1.62/1.64/1.50/1.70$ for Fe, $3p^6 4s^1 3d^7 4f^0$ and $1.68/1.90/1.66/1.80$ for Mn. The non-linear exchange-correlation correction [76] was included. The core-correction radii are 0.8 and 1.0 a.u for Fe and Mn, respectively. We have found that the basis sets with double-ζ for $3p/4s/4p$ shells and triple-ζ for $3d$ give reasonable results for both materials. For the real space grid, we set a uniform mesh corresponding to an energy cutoff of 400 Ry.

Two atoms in the unit cell were considered for both wires to describe the ferromagnetic and antiferromagnetic phases with the same cell. We chose 25 Å for the spacing between chains along x and y axes. One q point in the plane perpendicular to the wire and 96 q points along the wire were used for all calculations. All spin-polarized data obtained with the SIESTA code were compared with all-electron LCAO calculations
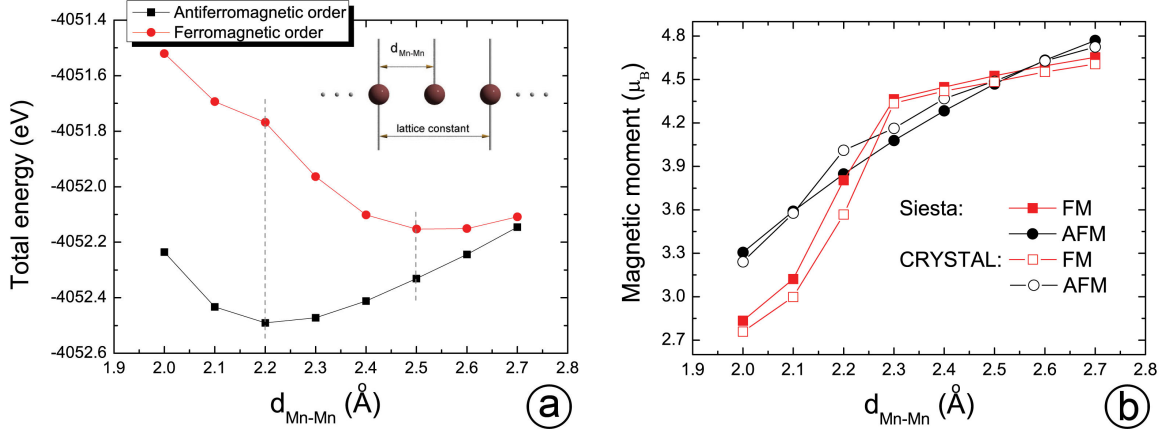
Figure 3.4: (a) Dependence of the total energy of the Mn chain from the Mn-Mn bond length for FM (red line) and AFM (black line) phases. (b) Magnetic moment of the manganese atom for FM and AFM pases as a function of the bond length obtained with SIESTA and CRYSTAL codes. FM - red line (open squares - CRYSTAL, solid squares - SIESTA), AFM - black line (open circles - CRYSTAL, solid circles - SIESTA).

using the CRYSTAL package [77] with the polarized valence triple-ζ (TZVP) basis set for Fe and Mn atoms [78].

The dependence of the total energy of the iron chain from the interatomic distance is shown in Fig. 3.3(a) for ferromagnetic (red line) and antiferromagnetic (black line) phases. As one can see, the wire is a one-dimensional ferromagnet and the energetically preferable structure corresponds to the bond distance d_{Fe-Fe}=2.2 Å, which agrees well with other theoretical calculations, for example 2.28 Å (Ref. [79]) and 2.25 Å (Refs. [80, 81]). The AFM phase is energetically less preferable within the whole bond length range. The magnetic moment of the iron atom is 3.27 μ_B in the FM ground state. It is increasing with stretching of the wire (see Fig. 3.3(b)). The AFM phase has smaller magnetic moment 2.86 μ_B at d_{Fe-Fe}=2.2 Å. The jump of the value of the Fe magnetic moment about d_{Fe-Fe}=2.05 Å is related to a low-spin/high-spin transition and agrees with data obtained in Ref. [82]. As one can see in Fig. 3.3(b), the SIESTA results and all electron calculations (CRYSTAL codes) agree well. They give practically the same magnetic moments on the iron atoms for both phases. The maximal difference between these methods is for the AFM phase and is equal to 0.16 μ_B at d_{Fe-Fe}=2.00 Å.

In contrast to the iron chain, the manganese wire is a 1D antiferromagnet. The dependence of the FM, AFM phases and the magnetic moment on the manganese atom from the Mn-Mn bond distance is shown in Fig. 3.4. The ferromagnetic phase shows a low-spin/high-spin transition. There is a jump of the value of the Mn magnetic moment from 3.1 μ_B at d_{Mn-Mn}=2.1 Å to 4.4 μ_B at d_{Mn-Mn}=2.3 Å. The magnetic moment increases monotonically with increasing Mn-Mn distances and is going to be
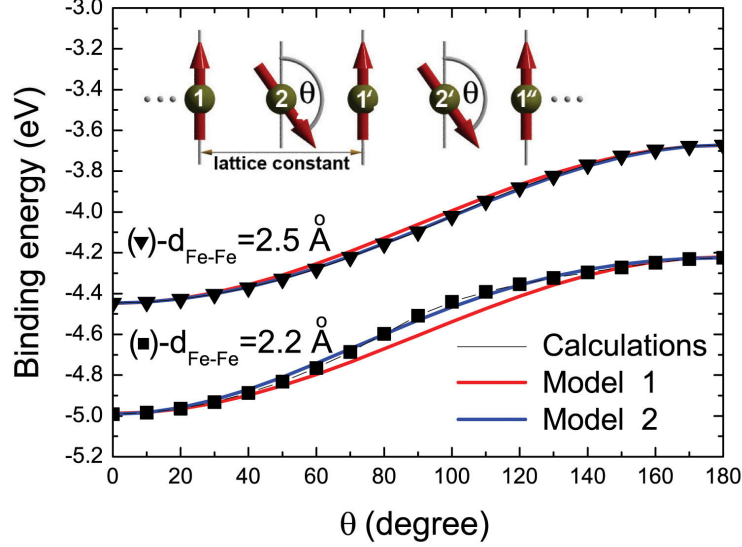
Figure 3.5: The binding energy of the one-dimensional Fe wire as a function of the direction of the magnetic moment on the second atom defined with polar angle Θ for the different interatomic distances (black line with squares - d_{Fe-Fe}=2.2 Å, black line with down-triangles - d_{Fe-Fe}=2.5 Å). Black lines - calculations, red lines - Model 1 and blue lines - Model 2 (see details in the text).

very close to the free atomic configuration ($5\mu_B$). It is also observed that SIESTA and CRYSTAL results are very similar (see Fig. 3.4(b)).

The transition between FM and AFM phases was investigated by varying only the direction of the magnetic moment of the second atom from 0° (FM phase) to 180° (AFM phase). The procedure was applied for both wires with different interatomic distances which are marked with dash lines in Fig. 3.3(a) and 3.4(a). The *ab initio* data are shown in Fig. 3.5 for the Fe wire and in Fig. 3.6 for the Mn wire. The binding energy of the wire was obtained as a difference between its total energy and two total energies of the free standing $3d$ atoms.

The orientational energy dependence (Figs. 3.5 and 3.6) can be interpreted in terms of a classical spin-system with an effective Hamiltonian. The magnetic state of N atoms can be characterized by the array of vectors $\vec{\mathbf{S}} = \{\vec{S}_i\}_{i=1,...,N}$, where $\vec{S}_i = S_i\vec{e}_i$ is the magnetic moment of a particular atom labeled by index i. S_i is the magnitude of the magnetic moment and $\vec{e}_i$ is the unit vector defining its direction. The energy of a classical spin-system can be described within the framework of a model Hamiltonian, the simplest of which is the classical Heisenberg model

$$H^{eff}(\{\vec{S}_i\}) = H^{(0)} + H^{(2)}(\{\vec{S}_i\}), \qquad (3.45)$$

which takes only the pairwise ($H^{(2)}(\{\vec{S}_i\})$) interaction between spins at lattice sites i and j into account. However, the second order approximation is not always sufficient
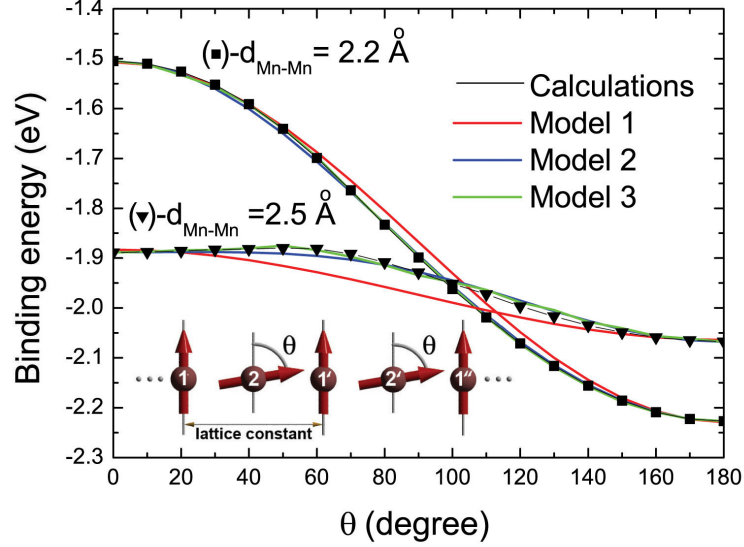
Figure 3.6:   The binding energy of the Mn wire as a function of the polar angle Θ which defines the magnetic moment direction on the second atom for the different interatomic distances (black line with squares - d_{Mn-Mn}=2.2 Å, black line with down-triangles - d_{Mn-Mn}=2.5 Å). Black lines - calculations, red lines - Model 1, blue lines - Model 2 and green lines - Model 3 (see details in the text).

to describe the energy of a magnetic system [21]. Therefore, the Heisenberg model can be extended with a fourth order spin-interaction $H^{(4)}(\{\vec{S}_i\})$ [91, 92] term which can improve the quality of the mapping of the energy from the first principles calculations to the spin-model. We can rewrite the Eq. (3.45) as

$$H^{eff}(\{\vec{S}_i\}) \quad = \quad H^{(0)} + H^{(2)}(\{\vec{S}_i\}) + H^{(4)}(\{\vec{S}_i\}), \qquad (3.46)$$

with

$$H^{(2)}(\{\vec{S}_i\}) \quad = \quad -2 \cdot \sum_{ij,i>j} J_{ij}(\vec{S}_i \cdot \vec{S}_j) \qquad (3.47)$$

$$H^{(4)}(\{\vec{S}_i\}) \quad = \quad -4 \cdot \sum_{\substack{ijkl \\ i>j,k>l}} Q_{ijkl}(\vec{S}_i \cdot \vec{S}_j)(\vec{S}_k \cdot \vec{S}_l), \qquad (3.48)$$

where J_{ij} are a exchange coefficients between atoms labeled by i and j, and the parameters Q_{ijkl} are related to a four-spin exchange interaction between atoms i, j, k and l.

Three models with different effective Hamiltonians for the description of the mono-atomic chains were used. The first one is the classical Heisenberg model. The next model assumes, that the longitudinal fluctuations of the moments can not be neglected, i.e., the magnitudes of the moments, M_i, can not be considered independent of the

orientational state, $\{e_i\}_{i=1,...,N}$. And the third model extends the second one with the fourth order spin-interaction terms. Taking into account that the value of the magnetic moment and its direction on the atoms i, $(i = 1, 2)$ is the same as on the atoms i', i'', ... (see insets in Fig. 3.5 and Fig. 3.6) we can write the following effective Hamiltonians:

$$\text{Model 1:} \quad H_I^{eff} = H_0 - 2J_{12}(\vec{e}_1 \cdot \vec{e}_2); \tag{3.49}$$

$$\text{Model 2:} \quad H_{II}^{eff} = H_0 - 2J_{12}(\vec{S}_1 \cdot \vec{S}_2) - 4J_{11}(\vec{S}_1 \cdot \vec{S}_1); \tag{3.50}$$

$$\text{Model 3:} \quad H_{III}^{eff} = H_{II}^{eff} - 4K_{11}(\vec{S}_1 \cdot \vec{S}_1)^2 - 2K_{12}(\vec{S}_1 \cdot \vec{S}_2)^2$$
$$- 4Q_{1112}(\vec{S}_1 \cdot \vec{S}_1)(\vec{S}_1 \cdot \vec{S}_2). \tag{3.51}$$

Here, we use a simplified notation for the biquadratic terms $K_{11} = Q_{1111}$ and $K_{12} = Q_{1212}$. Also, we have to note, that because of the choice of the cell the parameters J_{11}, J_{12}, K_{11}, K_{12} and Q_{1112} combine all long range interactions between correspondent atoms. Namely, $J_{12} \equiv J_{12} + J_{12'} + J_{12''} + ... + J_{1'2} + J_{1''2} + ...$, where the primes are related to the number of the cell.

The unknown parameters for different wires and different bond length were determined by fitting the binding energy of the orientational states obtained from first principles

Table 3.1: Calculated exchange interaction parameters of three different effective Hamiltonians (H_I^{eff}, H_{II}^{eff} and H_{III}^{eff}) for Fe and Mn monoatomic wires and two interatomic distances 2.2 Å and 2.5 Å. All data are given in units of meV.

Parameter	H_0	J_{11}	J_{12}	K_{11}	K_{12}	Q_{1112}
$d_{Fe-Fe} = 2.2$ Å						
H_I^{eff}	-4604.47		191.88			
H_{II}^{eff}, H_{III}^{eff}	-4525.94	-0.06	19.73			
$d_{Fe-Fe} = 2.5$ Å						
H_I^{eff}	-4060.33		193.78			
H_{II}^{eff}, H_{III}^{eff}	-2624.69	61.72	14.32			
$d_{Mn-Mn} = 2.2$ Å						
H_I^{eff}	-1857.87		-180.46			
H_{II}^{eff}	-1592.10	4.63	-12.24			
H_{III}^{eff}	-1034.66	14.79	-12.04	0.00	0.09	0.00
$d_{Mn-Mn} = 2.5$ Å						
H_I^{eff}	-1963.55		-45.29			
H_{II}^{eff}	-6864.82	-60.39	-0.68			
H_{III}^{eff}	-5605.08	-44.95	-1.08	0.00	0.01	0.00

calculations to the Eqs. (3.49)-(3.51). The fitting procedure is based on the least square method with the help of the CERN library subroutine FUMILI [93]. The results are shown in Figs. 3.5 and 3.6 and the exchange interaction parameters are collected in Table 3.1.

As one can see, the Heisenberg model (H_I^{eff}) gives quite satisfactory results for the relaxed Fe and Mn wires (d=2.2 Å) and fails for the elongated chains (d=2.5 Å). A better description can be obtained if one uses the extended Heisenberg model (H_{II}^{eff}), where the magnitude of the magnetic moment is taken into account. In this case, we can describe the intermediate region between FM and AFM phases for both wires in the correct way. In addition Model 2 describes the local minimum at $\Theta = 0°$ for the Mn wire with $d_{Mn-Mn} = 2.5$ Å (see Fig. 3.6). It is based on the changes of the magnituge of the magnetic moment, which is practically constant in the range from $\Theta = 0°$ to $\Theta = 60°$ and equals 4.49 μ_B. Then the value decreases to 4.47 μ_B. So small changes of the magnetic moment are important because of the small energy difference between the FM and the AFM phases (0.08 eV) and the small curvature of the curve around $\Theta = 0°$. The use of the fourth order spin-interaction terms in Eq. (3.51) is not improving the fit of the *ab initio* data. Moreover, the two parameters K_{11} and Q_{1112} are not sensitive during the fitting procedure.

3.6.2 Molecular trimer

The next application of our on-site constraint non-collinear LCAO method was the Mn_3 cluster. The investigations were performed with the same basis set and pseudo-potential as for Mn monoatomic wire. We have used both LDA and GGA exchange-correlation potentials.

The previous GGA based theoretical works [94, 95, 96, 97, 98] show that the ferro-magnetic ordering is energetically preferable for the Mn_3 cluster. On the other hand, the LDA [98, 99] calculations give antiferromagnetic ordering in the ground state with a total magnetic moment of 5 μ_B. Our calculations give good agreement with previous theoretical works.

We found that the FM structure is more stable then the AFM one with the a total magnetic moment of 15.0 μ_B for GGA with PBE [52] parametrization and LDA cal-culations with CA [44] parametrization. The AFM phase is more preferable for the VBH [39] exchange-correlation potential (LDA). The dependence of the Mn_3 binding energy on the Mn-Mn bond distance is shown in Fig. 3.7 for calculations with CA exchange-correlation potential. We consider the equilateral triangle of Mn atoms. We found two phases with ferromagnetic ordering and one with antiferromagnetic order-ing. The FM phase at small Mn-Mn distances has a small magnetic moment (3 μ_B on each atom). Then, there is a phase transition from low-spin to high-spin phase at $d_{Mn-Mn} = 2.45$ Å. The high-spin phase is characterized by a total magnetic moment 15 μ_B. The energy minimum corresponds to the bond distance 2.77 Å and agrees well with 2.8 Å [96], 2.9 Å [95] and 2.82 Å [94]. The full relaxation of the cluster destroys the equilateral triangle, like in [98], and conserves the same magnetic moments but different Mn-Mn bond distances (one 2.76 Å and two 2.77 Å).
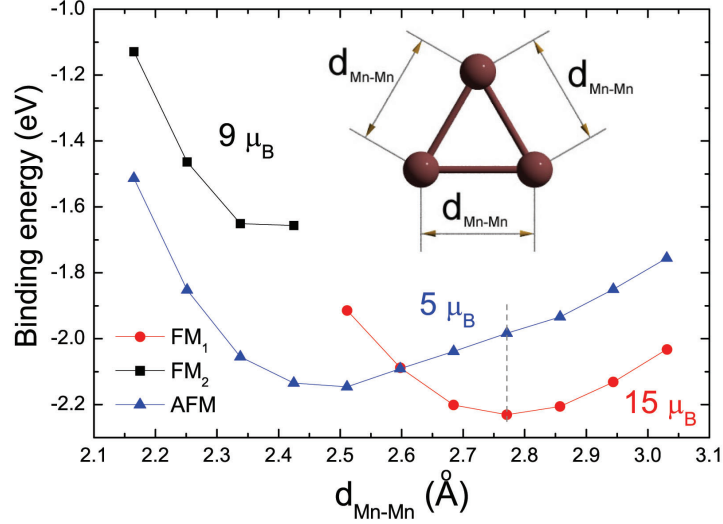
Figure 3.7: The dependence of the binding energy of the Mn_3 cluster from the Mn-Mn bond length. Red curve (FM_1) - hight-spin ferromagnetic phase, black curve (FM_2) - low-spin ferromagnetic phase and blue curve (AFM) - antiferromagnetic phase.

The antiferromagnetic phase has a minimum at 2.5 Å. The same Mn-Mn distance was obtained in [96], where the AFM phase is dominating. In our case, the AFM state is 0.07 eV higher in energy then the FM phase. The relaxation also decreases the symmetry of the cluster. The use of the PBE and PZ exchange-correlation potentials changes the position of the AFM curve (see Fig. 3.7). The PBE calculations shift it to the higher energies. For the PZ results, the AFM ordering is by 0.03 eV more preferable than the FM one. Thus, we confirm a strong sensitivity of the ground state to the exchange-correlation potential.

The transition from the FM to the AFM phase were investigated at d_{Mn-Mn}=2.77 Å (the dash line in Fig. 3.7). We consider the equilateral triangle, because of the small changes of the Mn-Mn bond length after the relaxation. In this case, we fix the magnetization direction on one atom and vary Θ_1 and Θ_2, as shown in Fig. 3.8.

The dependence of the binding energy on Θ_1 and Θ_2 is shown in Fig. 3.9(a). There is one global minimum at $\Theta_1 = \Theta_2 = 0°$ and two local minima at ($\Theta_1 = 90°$, $\Theta_2 = 180°$) and ($\Theta_1 = 180°$, $\Theta_2 = 90°$). Here we have to mention that the adsorption of the Mn_3 molecule on the Cu(111) and Ni(111) surfaces changes the magnetic structure and the ground state corresponds to a non-collinear configuration [100, 101]. At $\Theta_1 = 120°$, $\Theta_2 = 120°$ one can see a maximum, which is related to the state with compressed value of the magnetic moment 3.41 μ_B on each Mn atoms.

In order to understand the magnetic interaction in the cluster we mapped the potential energy surface (Fig. 3.9(a)) to the effective Hamiltonians similarly to the Mn wire. In
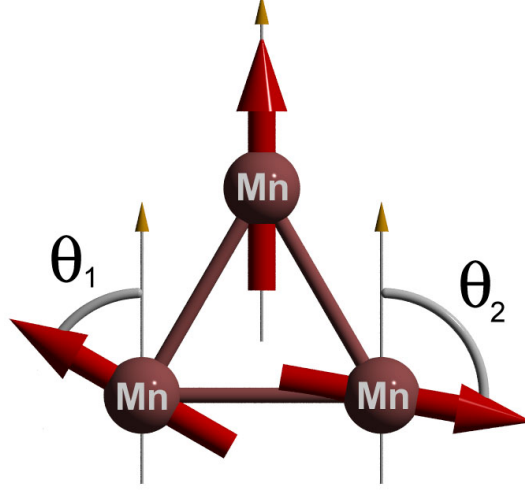
Figure 3.8: Schematic presentation of the non-collinear structure in the Mn_3 cluster. The magnetization direction on one atom is fixed. Θ_1 and Θ_2 define the direction of the magnetic moment on the two other atoms.

case of the Mn_3 cluster, the full Hamiltonian $H = H^{(2)} + H^{(4)}$ consists of nine different terms:

$$
\begin{aligned}
H &= H_0 + H_1 + H_2 + H_3, \quad \text{with} & (3.52) \\
H_1 &= -2 \cdot [J_{12}(\vec{e}_1\vec{e}_2) + J_{13}(\vec{e}_1\vec{e}_3) + J_{23}(\vec{e}_2\vec{e}_3)] \\
H_2 &= -4 \cdot \left[K_{12}(\vec{e}_1\vec{e}_2)^2 + K_{13}(\vec{e}_1\vec{e}_3)^2 + K_{23}(\vec{e}_2\vec{e}_3)^2\right] \\
H_3 &= -8 \cdot [Q_{1213}(\vec{e}_1\vec{e}_2)(\vec{e}_1\vec{e}_3) + Q_{1223}(\vec{e}_1\vec{e}_2)(\vec{e}_2\vec{e}_3) + Q_{1323}(\vec{e}_1\vec{e}_3)(\vec{e}_2\vec{e}_3)].
\end{aligned}
$$

Here, we use a simplified notation: $K_{12} = Q_{1212}$, $K_{13} = Q_{1313}$ and $K_{23} = Q_{2323}$. Note, that during this investigation we also apply the model which takes the magnitude of the magnetic moment into account and obtain practically the same results.

Table 3.2: The interaction parameters in meV for three effective Hamiltonians (H_I^{eff}, H_{II}^{eff} and H_{III}^{eff}).

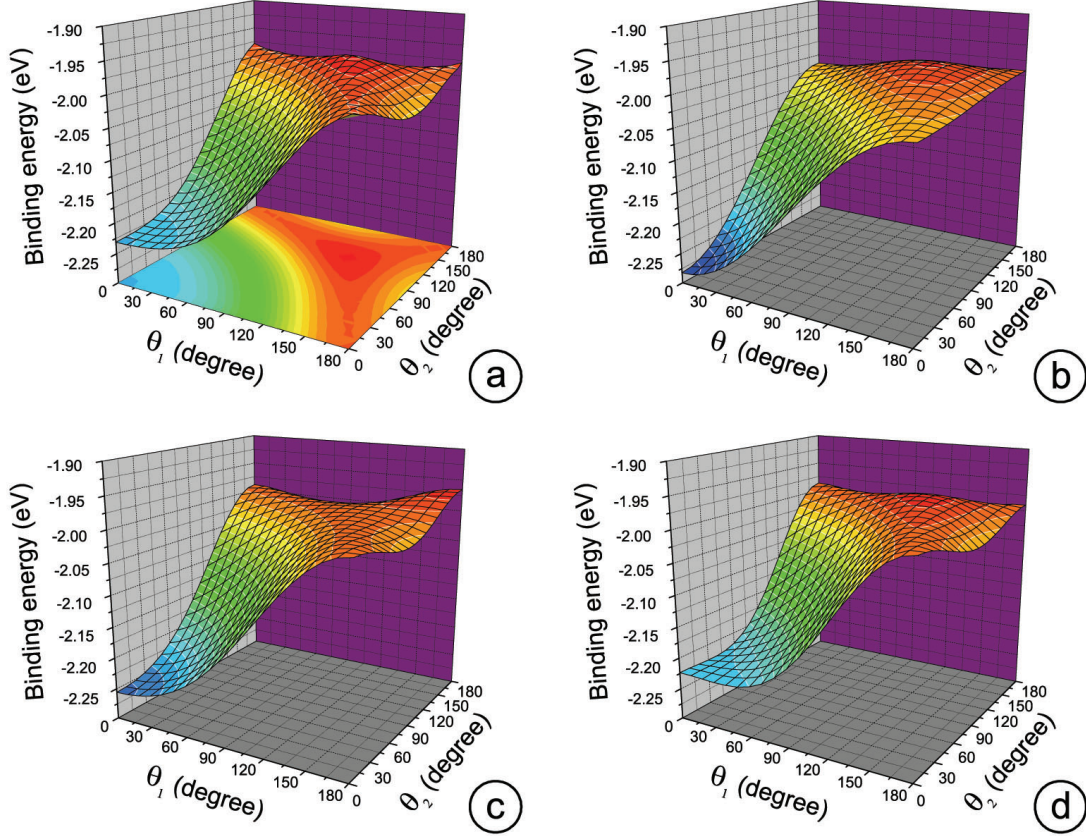| Parameter	H_0	J_{12}	J_{13}	J_{23}	K_{12}	K_{13}	K_{23}	Q_{1213}	Q_{1223}	Q_{1323}
H_I^{eff}	-2076.0	36.3	36.3	30.4						
H_{II}^{eff}	-2103.5	36.3	36.3	30.1	-3.9	-3.9	-5.5			
H_{III}^{eff}	-2134.6	39.2	39.2	47.8	-9.0	-9.0	-3.9	-4.5	-2.5	-2.5

Figure 3.9: Binding energy (eV) of the Mn$_3$ cluster as a function of the magnetization angles Θ_1 and Θ_2. (a) - *ab initio* calculations, (b) - fit with Heisenberg model Eq. (3.53), (c) - fit with Heisenberg model extended with the bi-quadratic terms and (d) - fit with full effective Hamiltonian (Eq. (3.52)). See details in the text.

We split Eq. (3.52) into three models which include different types of interactions. Namely, the classical Heisenberg model (H^I), the Heisenberg model with biquadratic terms (H^{II}) and the model (H^{III}) which combines all interactions:

$$
\begin{aligned}
H_I^{eff} &= H_0 + H_1; & (3.53) \\
H_{II}^{eff} &= H_0 + H_1 + H_2; & (3.54) \\
H_{III}^{eff} &= H_0 + H_1 + H_2 + H_3. & (3.55)
\end{aligned}
$$

The parameters J_{ij}, K_{ij} and Q_{ijkl} were determined by least square fitting the binding energy of the orientational states obtained from calculations to Eqs. (3.53), (3.54) and (3.55) with FUMILI [93] program. The exchange interaction parameters are presented in Table 3.2. And the potential energy surfaces for theoretical models are shown in Figs. 3.9(b)-3.9(d).

First of all, all models are giving good prediction of the main features (minimum and maximum). The other two local minima can be obtained only if some or all four-spin

interaction terms are taken into account. The analysis of the exchange interaction parameters perfectly shows that two atoms in the cluster are equivalent. Finally, the full model provides the best fit of the *ab initio* data. Therefore, we can conclude that for a precise description of the real system with an effective Hamiltonian, the four-spin interaction terms have to be taken into account.

4 Electronic structure of MetPc and MetBz molecules and 1D wires

During the last years, molecular magnets have been attracting enormous attention, because they are considered as potential candidates for future applications in high-density information storage and quantum computing. Among such novel systems, we are focusing on metallophthalocyanines (MetPc, Met=Co,Cu) and metal-benzene (MetBz, Met=Sc-Co, Bz=C_6H_6) molecules and wires.

The family of the MetPc have been intensively studied due to their potential applications in various devices such as organic light-emitting diodes [102], organic field effect transistors [103, 104] and organic photovoltaic cells [105]. They have attracted considerable interest because of their biological significance, catalytic properties and potential technological applications [106]. In addition, MetPc are magnetic materials. Moreover they demonstrate a good compatibility with ultra-high vacuum (UHV) and can be successfully grown as thin, ultra-clean, well ordered films on various substrates which increases the interest in them as promising materials for future spintronic applications. Despite the large number of studies, the question of the electronic structure of the CuPc and CoPc systems is still open.

The metal-benzene clusters Met_nBz_m can be synthesized in a gas phase reaction of laser-vaporized metal atoms with benzene in a He atmosphere [107, 108, 109, 110]. According to Ref. [107], the structures with early transition metals Sc, Ti, V and Mn can be organized in multidecker chains and the late transition metal-benzene complexes of Fe, Co and Ni have rise-ball structures where benzene molecules coat the metal atoms. Recently, Stern-Gerlach-type magnetic deflection experiments [109, 110, 111] suggested monotonic increase of the magnetic moment for V_nBz_{n+1} ($n = 1 - 4$) and Sc_nBz_{n+1} ($n = 1 - 2$), indicating that the magnetic moments of the V and Sc atoms couple ferromagnetically. Then, the theoretical investigations [112, 19] show that the infinite vanadium benzene chains are half-metals and can be used as a nearly perfect spin-filter when the VBz cluster is placed between magnetic electrodes.

4.1 Metallophtalocenes

The molecular structure of the MetPc, Met=Co,Cu molecules is shown in Fig. 4.1. They have a planar structure with D_{4h} point symmetry. Each molecule consists of the central $3d$ atom, which is surrounded by four nitrogen atoms - pyrrole (N_1); four other nitrogen atoms - bridging aza (N_2); 32 carbon atoms - the pyrrole (C_1) and the benzene ones (C_2, C_3 and C_4).
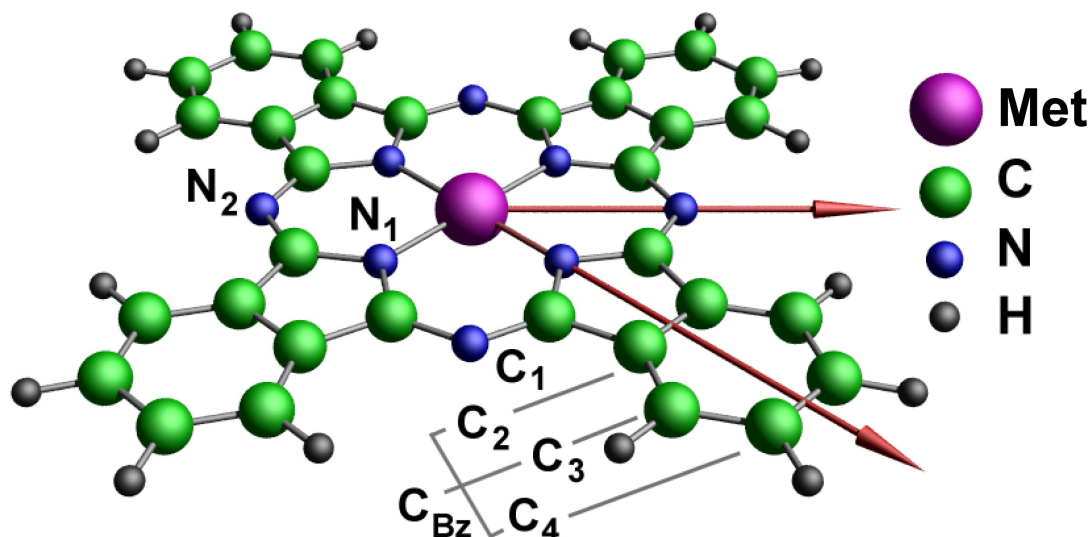
Figure 4.1: Schematic representation of the molecular structure of the MetPc, Met=Co,Cu molecules. The arrows are indicating high-symmetry directions.

Calculations were performed using the linear combination of atomic orbitals (LCAO) formalism based on density-functional theory and realized in the CRYSTAL code [113]. The three-parametric Becke+Lee-Yang-Parr (B3LYP) exchange-correlation functional [55] was applied for the calculations. It partly corrects the self-interaction error inherent in local density (LDA) and generalized gradient approximations (GGA) by mixing the exact Hartree-Fock exchange with the GGA exchange functional. The electronic wave functions were described by 6-311+G** basis sets for C, N and H atoms [114] and the TZVP [115] basis set for copper and cobalt. In addition, we have examined and obtained the same electronic structure with 6-31+G* [116] and Ahlrich PVTZ [117] basis sets for light elements and Ahlrich PVTZ [117] and frozen-core SBKJC [118] basis sets for Cu. The atomic coordinates of the CuPc molecule were optimized by means of a modified conjugate gradient algorithm [119].

The theoretical data were used for analyzing the photoemission (PES), resonant photoemission (RPES) and near-edge x-ray absorption (NEXAFS) spectra [120, 122, 122, 123]. The experiments were performed at the Berliner Speicherring für Synchrotronstrahlung (BESSY) using the soft-x-ray synchrotron light emitted by the Russian-German high energy resolution dipole beam line [124]. The CuPc/CoPc films were evaporated on the Au(100) surface and deposited in a sample preparation chamber (base pressure of 2.5×10^{-10} Torr) directly connected to the analyzer chamber. The core level photoemission spectra showed that CuPc films were grown without traces of contamination. The CuPc and CoPc films were about 70 Å thick, which is large enough to minimize contributions from the gold substrate in the photoemission spectra, and small enough to avoid charging effects. Other details of the sample preparation
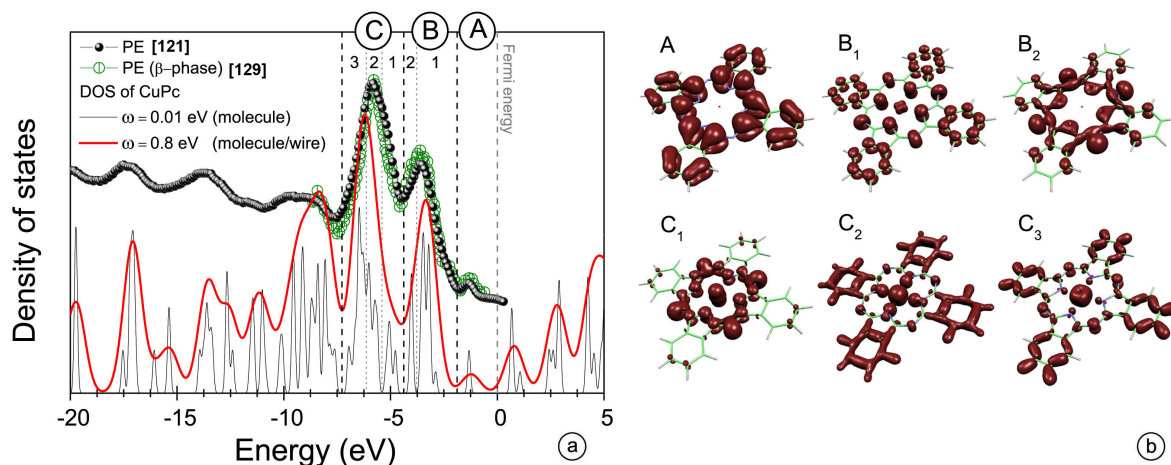
Figure 4.2: (a): Thick/thin line: calculated valence band density of states of isolated CuPc molecules. The DOS is smeared with a Gaussian functions FWHM = 0.8/0.01 eV and it is the sum of the density of states for both spin-channels. Filled circles correspond to PES of the VB of the CuPc film (7 nm) (normal emission, $h\nu = 110$ eV). Open circles are from Ref [129]. Zero corresponds to the Fermi level of a clean gold foil (b): CuPc molecules and calculated charge distribution (red) contributing to the corresponding peaks of the valence bands (as labeled).

procedure as well as of the experimental measurements can be found elsewhere (see e.g. [125]).

4.1.1 CuPc systems

Fig. 4.2(a) shows the photoemission valence band (VB) spectrum taken at normal emission from a thin (7 nm) CuPc film (circles) together with the calculated density of states (DOS) of CuPc molecules (thick and thin lines). In order to align the spectra, the theoretical first occupied peak was shifted to the binding energy position of the experimental peak arising from the highest occupied molecular orbital (HOMO). To ease the comparison, a broadening of the calculated VB states has been carried out by application of a Gaussian function to each calculated state (FWHM = 0.8 eV for the thick line). This procedure takes life time broadening due to defects and instrumental broadening into account. Note, the calculated DOS is the sum of the density of states for both spin-channels.

The experimental photoemission spectrum is in good agreement with previous data of the same system taken at different [127] as well as at similar [128, 129] photon energies. In addition, the photoemission spectra are almost identical for different CuPc film preparations: grown on Au(100) surfaces or on Si surfaces (α and β phase) [129]. For example, Fig. 4.2(a) shows excellent agreement between our PES and one
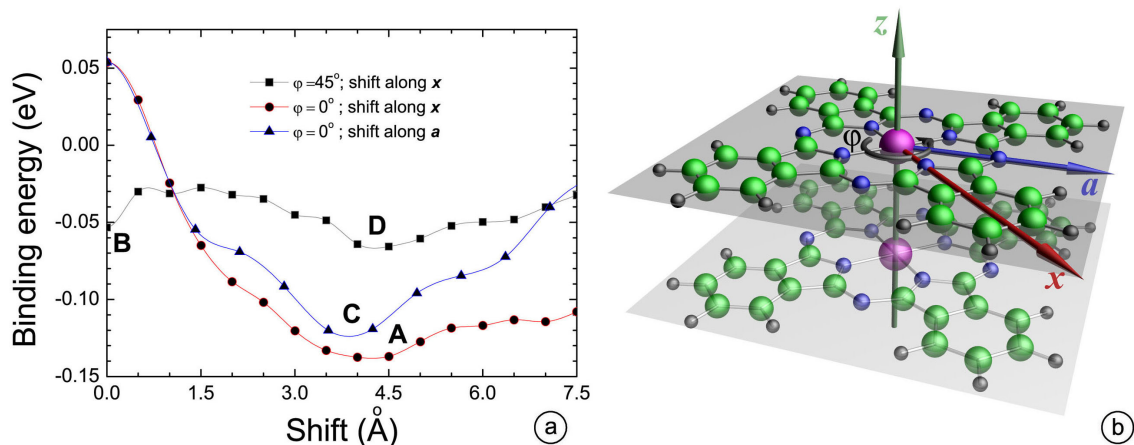
Figure 4.3: (a) Binding energy between two CuPc molecules as a function of displacement of the second one along the a and x axes for two angles $\varphi = 0°$ and $\varphi = 45°$. Angle φ and a, x axes are shown as inset.

taken from Ref. [129] for the β-phase of CuPc. Such agreement of the experimental results proves weak intermolecular bonding in different phases of CuPc films.

In order to perform a generalized investigation, different structures, a free standing molecule and a 1D CuPc wire, were investigated theoretically. The CuPc chains were chosen to simulate different CuPc (α[130], α'[131], β[130], ε[132], γ[132]) phases and the CuPc layer. In addition we investigate the interaction between one CuPc molecule for different positions of the second CuPc. The calculated binding energy between the molecules is shown in Fig. 4.3(a). At the beginning, the Cu atoms sit on top of each other and the distance between the molecular planes was 4 Å, then the second CuPc molecule was shifted along the x or a axes (see Fig. 4.3(b)).

Four energy minima were found. A global minimum, labelled **A**, corresponds to the shift along the x axis at 4.25 Å. The second minimum **B** related to geometry occurs when the molecules sit on top of each other and second molecule is rotated by 45° with respect to the previous one. It can correspond to a new high-pressure phase of CuPc. Two other minima can describe metastable states **C** and **D**. We have to mention that for all structures the binding energy is quite small and has a maximum value of 0.138 eV for **A**. The feature **C** is energetically less preferable by 0.014 eV. The small energy difference between these two structures and the broad shape of feature **A** allows the coexistence of these two phases at high temperature. Therefore, the annealing like in Ref. [133] provides highly ordered CuPc molecules on the gold surface. The analysis of the structural data of different CuPc phases shows that they correspond to the feature **A** with some deviations from the minimum. In this case we can assume that weak interaction between CuPc chains is responsible for different arrangements (Herringbone interaction in the β-CuPc or parallel stacking like in the α'-phase etc.) of the molecules.

The calculations show practically the same electronic structure for all CuPc chains. The difference stems only from the relative positions of the band related to the mixture of Cu ($d_{x^2-y^2}$) and N (p_x, p_y) orbitals. It is well separated and situated in the gap between the highly occupied band and the π bands of the benzene and pyrrole rings for the chains related to the β-, the ε-phases and the minimum **B**. While, it is mixed with π bands of aromatic rings for wires from the α, α', γ-phases and **A** geometry. Therefore, the shoulder at 2.5 eV is well distinguishable for the β-phase (see Fig. 4.2(a)) and badly visible for our CuPc films. In addition, the Cu ($d_{x^2-y^2}$) and N (p_x, p_y) orbitals are responsible for the magnetic moment in the CuPc molecule, they are occupied for one spin channel (situated $\sim$1.5 eV below the top of the valentce band) and unoccupied of other one (situated $\sim$0.5 eV above the bottom of the conduction band).

There is a small dispersion of the HOMO (0.55 eV) and the LUMO (0.27 eV) bands. It is due to the interaction of π or π^* orbitals of the aromatic rings which are responsible for the bonding between CuPc molecules. All other bands have smaller or no dispersion (states corresponding to Cu atoms). The HOMO-LUMO gap of the CuPc molecule (2.2 eV) agrees well with measured transport gaps, 2.1 eV [134] and 2.3 eV [135]. It is slightly larger than the calculated gap of a CuPc wires (1.6 eV for the α-, γ-phases and **A**-structure, 1.8 eV for the α'-phase, 1.3 eV for the β-phase and 1.5 eV for the ε-phase and **B**-geometry) which compares favorably with experimental values obtained from optical or electron energy-loss spectroscopy, 1.5 eV [134].

Figure 4.2 shows very good agreement between experiment and theory. The total DOS of the CuPc wire is broadened by a Gaussian function with FWHM=0.8 eV. Note, the DOS of the CuPc wire (created from the structure related to minimum **A**) in both magnetic configurations (AFM and FM) and of the CuPc molecule are very similar (Fig. 4.2). Differences disappear under application of a Gaussian function with FWHM=0.8 eV. The HOMO (labeled with A) is mainly formed by the spectral weight of the wave functions of carbon pyrrole (C_1) atoms. Additional contributions to the HOMO stem from the benzene atoms C_3 and C_4. The second feature (peak B) has a more complicated structure. The analysis of molecular orbitals allows to separate them into three independent groups. The first two groups situated in the same energy range from -2.55 to -3.77 eV, marked as B_1, reflect contributions from hybrid Cu ($d_{x^2-y^2}$) and N_1 (p_x, p_y) orbitals, and benzene and pyrrole π states. Note that the hybrid Cu($d_{x^2-y^2}$)/N(p_x, p_y) state is occupied for the spin-up channel and unoccupied for the spin-down one. We should emphasize that the position of the d orbital is in contradiction with other theoretical results at LDA level [129, 136], where the HOMO is formed by the Cu ($d_{x^2-y^2}$) state. We have reproduced these results by means of the same local-density exchange-correlation functional. Since it is known that LDA has deficiencies in the description of localized highly correlated electronic states, particularly for $3d$ transition metals, we conclude that the obtained spectra based on LDA are an artifact. We have to mention that even GGA improves the position of the hybrid Cu($d_{x^2-y^2}$)/N(p_x, p_y) state. According to our calculation, it is 0.10 eV below the HOMO and is in good agreement with Ref. [137]. With B3LYP we observe a pronounced charge transfer ($0.7e^-$) from Cu to the pyrrole N and a strong hybridization between the d orbitals of Cu and p orbitals of N. Therefore, every state
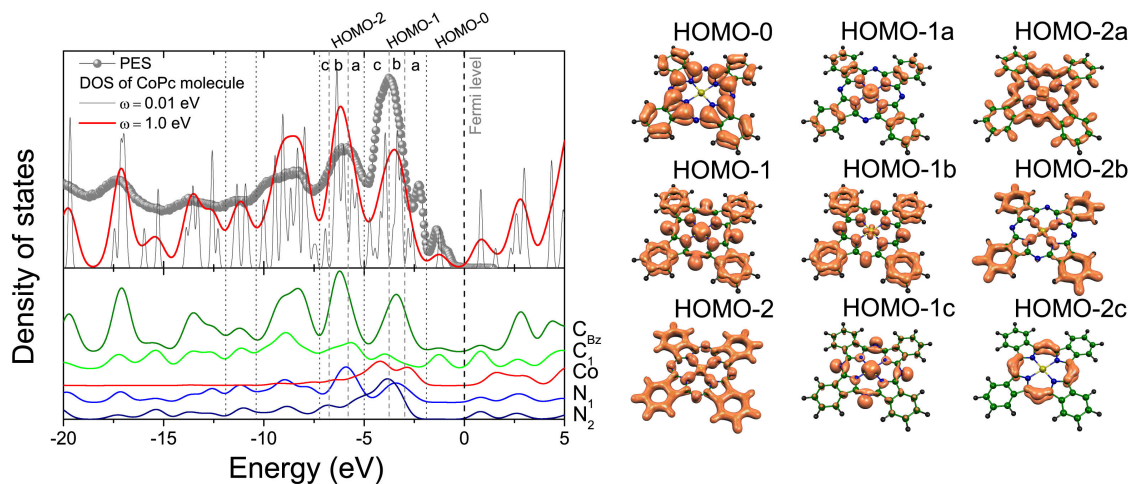
Figure 4.4: (Left upper panel): Circles: PES of the VB of the CoPc film (7 nm, normal emission, $h\nu = 110$ eV). Thick/thin line: calculated DOS of isolated CoPc molecules, after application of a Gaussian function to each calculated state with a FWHM=1.0/0.01 eV. (Left lower panel): the density of states projected onto various atomic species. The DOS is the sum of the density of states for both spin-channels. (Right panel): the charge distribution (orange) contributing to the corresponding peaks of the CoPc valence band (see text for the details).

with predominant N_1 p character induces density on the Cu atom and vice versa. The calculated magnetic moment of Cu is 0.57 μ_B, and on every N_1 atom it is 0.1 μ_B. Similar results were obtained in a previous paper [129]. The third group (Fig. 4.2 - region B_2) arises from σ-bonding orbitals between bridging aza N_2 and pyrrole C_1, with main contributions from the nitrogen atoms. Moreover, these σ-bonding states are also present in the peak C_1 with an energy around -5 eV. In conclusions, σ-bonding orbitals of benzene and 3d orbitals (d_{z^2}, d_{xz}, d_{yz}, d_{xy}) of Cu determine the structure C (C_2 and C_3 regions in Fig. 4.2). There, like for higher energy features, the d orbitals are hybridized with the p orbitals of the N_1 atoms. The charge distribution contributing to the corresponding peaks of the valence band (A, B and C) is shown in Fig. 4.2(b). The densities are normalized to the number of states in the corresponding region. The figures show surfaces of equal charge density ($5 \cdot 10^{-5}$ e/Bohr^3).

4.1.2 CoPc molecule

Fig. 4.4 shows the photoemission VB spectrum taken at normal emission from a thin (7 nm) CoPc film (circles) together with the calculated valence band structure of CoPc molecules (thick and thin lines). The theoretical and experimental spectra were aligned to the position of the first occupied peak. The DOS of the CoPc molecule was broadened with Gaussian functions (FWHM = 1.0 eV). This procedure takes solid state effects and instrumental broadening into account.

The CoPc films prepared are characterized as highly ordered, and the CoPc molecule lies on the single crystalline substrate, *id est* the organic molecular plane is parallel to the substrate surface [139]. Since, according to our results and Ref. [140], there is a week molecule-molecule interaction in the molecular crystals, the electronic structure of the molecular solid state crystals is mainly formed by the electronic structure of the single MetPc molecule.

One can see reasonable agreement between experimental and theoretical data. The features of the experimental spectrum are reflected in the theoretical curve. Here, we have to note, that we perform spin-polarized calculations, but only the sum of spin-up and spin-down densities is shown. For better understanding of the nature of the occupied states, the isodensity surfaces for the HOMO-0, HOMO-1 and HOMO-2 features were plotted and shown in Fig. 4.4. The first feature (HOMO-0) includes π-states situated on both aromatic rings. The analysis of the projected DOS on the atomic species (Fig. 4.4, lower left panel) shows, that mostly the states from pyrolle carbon dominate here. We note that the present calculations do not reproduce the double peak near the Fermi level as seen in the photoemission spectra. This aspect has to be clarified in the future. The CoPc molecule HOMO-LUMO gap is equal to 2.02 eV. We are expecting the smaller bang gap for the CoPc molecular crystals.

The second feature (labeled as HOMO-1) has contributions from π states localized on benzene and hybrid Co-N states. The analysis of the molecular orbitals allows to separate the HOMO-1 region into three independent contributions. The first (HOMO-1a) has contributions from π states localized on benzene and hybrid $Co(d_{xz},d_{yz})/N(p_{x/y})$ orbitals, where the d_{xz}, d_{yz} states are occupied for both spin channels. Here, the density of the $N(p_{x/y})$ orbitals predominates over $Co(d_{xz}, d_{yz})$. The second part (HOMO-1b) consists of π states with equally distributed density on benzene and on hybrid $Co(d_{xy})/N(p_{x/y})$ states which are occupied for the spin-down electrons. The spin-up $Co(d_{xy})/N(p_{x/y})$ orbitals form the last part (HOMO-1c) of this series. Both spin components of the cobalt DOS are completely asymmetric. The spin-down states are shifted towards E_F in comparison with the spin-up states. The $Co(d_{xy})/N(p_{x/y})$, $Co(d_{z^2})$ spin-up densities and $Co(d_{xz}, d_{yz})/N(p_{x/y})$, $Co(d_{x^2-y^2})$ states are related to the third group (HOMO-1c). The magnetic moment of the Co atom is 1.15 μ_B. Other atoms in the molecule are weakly polarized and they share together -0.15 μ_B (up to 0.02 μ_B on N_1 atoms). The third feature (labelled as HOMO-2) consists of σ states of benzene and pyrolle like states in the CuPc molecule [141]. The contribution of the d orbitals of the Co atom to this feature is small, and a separation into individual components is shown in Fig. 4.4 as HOMO-2a to HOMO-2c.

4.2 MetBz molecules and one-dimensional wires

The schematic structures of the MetBz systems are shown in Fig. 4.5. One can see that they have C_{6v} symmetry and can have a half-sandwich (Fig. 4.5(a)), a sandwich (Fig. 4.5(b)) or a chain (Fig. 4.5(c)) structure. Note that here we do not consider
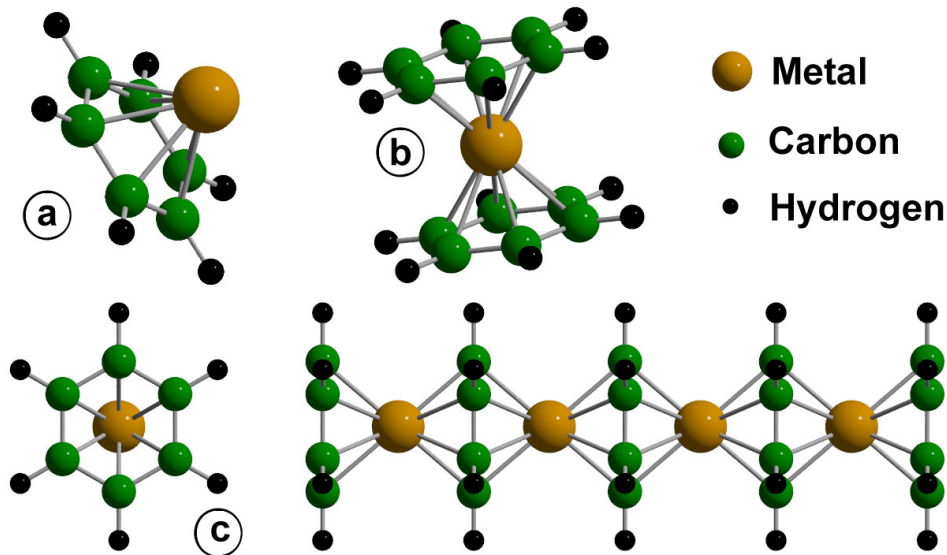
Figure 4.5: The schematic structure of the MetBz clusters. (a) half-sandwich; (b) sandwich; (c) chain.

the MetBz systems with rice-ball structure. Nevertheless, we will analyze why such structures are preferable for MetBz, Met=Fe-Ni compounds.

The theoretical investigation were performed using the LCAO method implemented in the CRYSTAL code [113]. The GGA exchange-correlation functional with Perdew-Wang [48] parametrization was employed. The electronic subsystem was described by Gaussian type basis sets, where a 6-311+G** basis was used for C and H atoms [114] and a frozen-core SBKJC [118] basis was applied for the whole row of transition metals (from Sc to Cu). The influence of the choice of the basis set on the MetBz properties were also investigated. We use different combinations of the 6-31+G* [116] and Ahlrich PVTZ [117] basis sets for light elements and Ahlrich PVTZ [117] and TZVP [115] basis sets for transition metals. We found that the choice of the basis set does not change significantly the ground state of the MetPc systems or their properties within the same exchange-correlation potential. In order to omit the problem of the electron-correlation effects, we additionally use the Vosko-Wilk-Nusair LDA [43] and hybrid B3LYP [55] potentials. We also verify our data of the electronic structure with the local density approximation LDA+U scheme [142] using the projector augmented wave method [143] implemented in the VASP [144] package.

4.2.1 MetBz half-sandwiches

The previous studies [145, 146, 147, 148, 149, 150, 151] have found that the transition metal-benzene complexes have a half-sandwich type structure in which the metal atom is located above the benzene plane on the C_{6v} axis. In our case, we have got the same result. The full relaxation of the MetBz clusters maintain the C_{6v} symmetry. We also
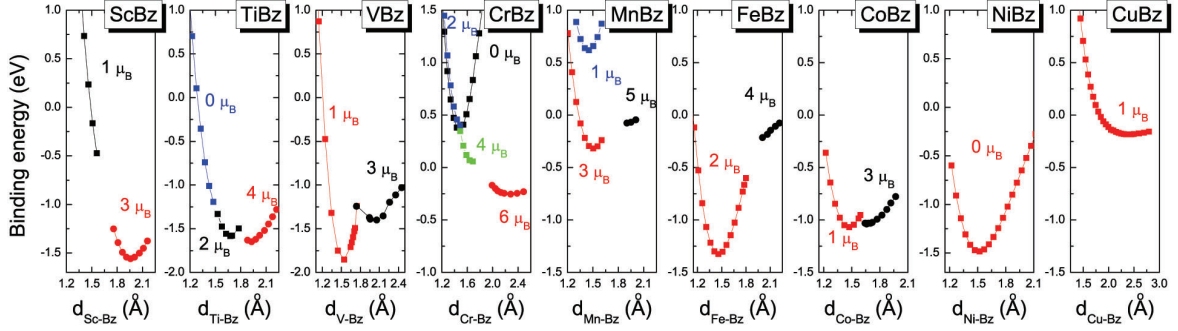
Figure 4.6: The binding energy of the MetBz, Met=Sc-Cu half-sandwiches as a function of the Met-Bz distance for the different magnetic states. The energetically preferred state for each cluster is marked in red.

found that the planes created from hydrogen atoms are shifted away from the carbon atoms less then 0.02 Å in direction of the metal atom. There is a small distortion of the C-C ($\sim$0.02 Å) and C-H ($\sim$0.01 Å) bonds in comparison to the isolated benzene. Nevertheless, all benzene ring deformations are negligible for the binding energy and the electronic structure calculations. Moreover, the local relaxation of the benzene ring during the change of the Met-Bz distance is also not significant.

In the next step of our investigations, we analyze the dependence of the binding energy of the MetBz compounds from the distance between 3d atom and the center of gravity of the benzene ring. In the present study, each of the transition metal atoms was shifted along the C_{6v} axis of the fixed benzene molecule. The binging energy is defined as the energy required to dissociate the molecule into the individual metal atom and the benzene ring:

$$E_{BE}^{MetBz} = E_{MetBz} - E_{Met} - E_{Bz}, \tag{4.1}$$

where E_{MetBz}, E_{Met} and E_{Bz} are the total energies of the MetBz molecule, metal atom and benzene ring, respectively.

The final data are shown in Fig. 4.6. One can see, a variety of the magnetic configurations within a narrow energy and Met-Bz distance ranges. Despite the large number of studies [145, 146, 152, 153], the contradictory results concerning both the geometry and the magnetic moment of the ground state were obtained. Our data are in good agreement with the DFT-level studies of Pandey and co-workers [145, 146] and also agree well with the multireference configuration interaction method data [153] for the ScBz and the NiBz short-range state. In Table 4.1 the results of the calculations of the optimized Met-Bz distance (d_{Met-Bz}), binding energy (E_{BE}^{MetBz}), magnetic moments per molecule μ_{total} and transition metal atom μ_{Met} for the first-row MetBz compounds are summarized.

ScBz: The ScBz molecule can be in low-spin and high-spin states. The second one is energetically preferable. The molecule in the high-spin state has a magnetic moment of 3 μ_B. The scandium atom has a magnetic moments of 2.13 μ_B. The ring has a quite

Table 4.1: The Met-Bz distance (d_{Met-Bz}), binding energy (E_{BE}^{MetBz}) and magnetic moments of the 3d atom (μ_{Met}) and the whole MetBz, Met=Sc-Cu molecule (μ_{total}) in the ground state.

Method	ScBz	TiBz	VBz	CrBz	MnBz	FeBz	CoBz	NiBz	CuBz
d_{Met-Bz} (Å)	1.96	1.93	1.55	2.27	1.50	1.46	1.47	1.51	2.40
E_{BE}^{MetBz} (eV)	-1.56	-1.65	-1.85	-0.25	-0.32	-1.32	-1.07	-1.48	-0.18
μ_{Met} (μ_B)	2.13	3.38	1.21	5.82	3.46	2.23	1.05	0	1
μ_{total} (μ_B)	3	4	1	6	3	2	1	0	1

large induced magnetic moment 0.87 μ_B. Moreover, the carbon atoms have positive magnetic moments of 0.161 μ_B, while the hydrogen atoms have a small negative moments of -0.016 μ_B. There is a small charge transfer of 0.16e from Sc to Bz. Here, we obtain good agreement with DFT data [145] and MP2-level results [154] concerning the geometry, magnetic configurations and the binding energy. The multireference configuration interaction study [153] defines our ground state as a metastable short-range state, which is about 1.6 eV higher in energy than the long-range state (d_{ScBz}=4.96 Å). Such large energy difference between short- and long-range states suppress the formations of the ScBz sandwiches or chains. On the one hand, the Sc atom is situated quite far from the benzene ring and on the other hand the mass-spectrometry data show the presence of Sc_nBz_{n+1} molecules [107, 108]. Therefore, we assume that one needs more detailed correlation-like multireference perturbation studies, which can clarify the formation of the multidecker structures.

TiBz: The ground state of the TiBz half-sandwich is at distance d_{TiBz}=1.93 Å. Here, three magnetic states can be realized: singlet (μ_{total}=0 μ_B), triplet (μ_{total}=2 μ_B) and quintet (μ_{total}=4 μ_B). The ground state is related to the quintet one with μ_{Ti}=3.38 μ_B. Here, the induced magnetic moment on the aromatic ring is also positive (like in ScBz) and equal to 0.62 μ_B. The same magnetic configuration and geometry was obtained in Refs. [145, 155, 151]. In addition, our binding energy for the TiBz molecule (-1.65 eV) is in good agreement with other theoretical -1.71 eV [145] and experimental -1.76 eV [107] results. It is larger then -1.06 eV in [151] and -1.20 eV in [155]. There is also a local minimum related to the triplet state. According to our data, it is only 0.07 eV less preferable then the global minimum.

VBz: The investigation of the VBz molecule has a long history. The electron paramagnetic resonance (ESR) and electron spin resonance (ESR) measurements [156, 157, 158] define a doublet electronic ground state. The theoretical investigations show contradictory results. The LCAO-DFT level calculations define the basis dependence of the ground state, namely the LANL2DZ basis prefers the quartet multiplicity [145], while the doublet ground state was obtained with the 6-311G** basis set [146]. The multireference configuration interaction calculations [153] have found that at short-range, the VBz ground state has a quartet multiplicity and it is metastable with respect to

the dissociation into V and Bz. Our data are closer to the EPR or ESR measurements and theoretical investigations with the 6-311G** basis set, where the doublet ground state was obtained. The potential surface of the VBz molecule (see Fig. 4.6) shows also the quintet state, which is at d_{VBz}=2.04 Å and ∼0.45 eV higher in energy. The vanadium atom has a magnetic moment 1.21 μ_B and the ring is negatively magnetized (μ_{ring}=-0.21 μ_B). The binding energy is -1.85 eV agrees well with -2.09 eV [146] and is larger than the experimental values -1.14 eV [159] and -0.79 eV [146]. Note, the experimental binding energies are empirical data, which are evaluated from

$$E_{BE}^{MetBz} = I_{VBz} + E_{BE}^{V^+Bz} - I_V, \tag{4.2}$$

where I_{VBz} and I_V are the ionization potentials of the VBz molecule and the V atom, respectively, and $E_{BE}^{V^+Bz}$ is the binding energy of the V$^+$Bz cation.

CrBz: Four magnetic configuration can be realized in CrBz system. As one can see from Fig. 4.6, the energetically preferable state is the septet (μ_{total}=6 μ_B). The local magnetic moment of the Cr atom is 5.82 μ_B. Here, like in ScBz and TiBz complexes, the carbon atoms of the ring have also a positive induced magnetic moment. The same state was obtained with the valence configurational interaction method [152]. There, it is defined as a long-range state. The previous DFT level calculations [145] also found the same magnetic moment in the ground state. The binding energy between the Cr atom and the aromatic ring is -0.25 eV, which agrees well with a theoretical value of -0.09 eV and an experimental value of -0.12 eV [145].

MnBz and FeBz: In the ground state, the MnBz molecule has a total magnetic moment of 3 μ_B and its binding energy is -0.32 eV at d_{CoBz}=1.50 Å. Other magnetic states can also be realized, but they are energetically not preferable. The Mn atom induces a negative magnetic moment of -0.46 μ_B on the benzene ring. The FeBz aromatic subsystem has also an induced magnetic moment in the ground state. The optimized structure of FeBz has a Fe-Bz distance of d_{FeBz}=1.46 Å. The binding energy between the Fe atom and the ring is -1.32 eV. In general, our MnBz and FeBz relaxed coordinates and the binding energy data are in good agreement with previous theoretical data from Ref. [145].

CoBz: The lowest-energy structure of the CoBz molecule is found to be doublet (μ_{total}=1 μ_B) and corresponds to d_{CoBz}=1.47 Å. The next magnetic state is quartet (μ_{total}=3 μ_B). It is only 35 meV higher in energy with an optimized distance d_{CoBz}=1.66 Å. The same elongation of the Co-Bz distance for the doublet-quartet transition was found in Ref. [147]. The organic part of the molecule has an induced magnetic moment for both magnetic states. Namely, the doublet state is characterized by an induced moment of μ_{Bz}=0.05 μ_B, while the high-spin structure has a two times large moment μ_{Bz}=0.1 μ_B. Our binding energy of the Co atom to the benzene molecule in the ground state structure is -1.07 eV, which is close to the experimental value of -0.64 eV [160]. Other theoretical investigations report smaller (-0.22 eV [147, 148]) and larger (-1.83 eV [145]) binding energies.

NiBz and CuBz: The optimized distance of NiBz is d_{NiBz}=1.51 Å. The molecule is nonmagnetic and its binding energy is -1.48 eV. In general, our data are in good agreement with [149, 145]. In contrary to NiBz, CuBz is magnetic with a total magnetic

Table 4.2: The Met-Bz distance (d_{Met-Bz}), the displacement of the H atoms plane from the C atoms plane (d_{CC-HH}), binding energy ($E_{BE}^{MetBz_2}$) and magnetic moments of the 3d atom (μ_{Met}) and the whole MetBz$_2$, Met=Sc-Mn molecule (μ_{total}) in the ground state.

Method	ScBz	TiBz	VBz	CrBz	MnBz
d_{Met-Bz} (Å)	1.95	1.73	1.65	1.58	1.64
d_{CC-HH} (Å)	-0.005	0.037	0.045	0.053	0.029
$E_{BE}^{MetBz_2}$ (eV)	-2.26	-3.30	-3.58	-3.07	-1.38
μ_{Met} (μ_B)	0.46	0	1.21	0	1.05
μ_{total} (μ_B)	1	0	1	0	1

moment of 1 μ_B, but there in no induced magnetic moment on the ring and the s-orbitals of the Cu atom are responsible for the magnetism in the molecule. In the ground state, the CuBz molecule has quite large metal-benzene distance d_{CuBz}=2.4 Å. And the potential profile of CuBz (see Fig. 4.6) is very flat around the minimum and allows to assume a very high reactivity of these system. In addition, the complex has a small binding energy -0.18 eV, which agrees well with the experimental value -0.17 eV [107].

4.2.2 Stability of the MetBz$_2$ sandwiches

As was mention before, only some of the transition metal atoms can form the multidecker structures. The mass spectrometry and reactivity experiments [107, 108] showed that the structure of neutral complexes depends on the metal and can be observed in sandwich structure for the early transition metals (Sc, Ti, V, Cr and Mn) and in rice-ball structure for the late transition metals (Fe, Co, and Ni). The theoretical investigations [146, 147, 148, 149, 150, 161] also confirm these results.
Here we extend the previous theoretical investigations and perform extensive and systematic analysis of the stability of the MetBz$_2$ molecules. We concentrated our attention on the interaction of the MetBz half-sandwich with the benzene ring which was placed in different positions. In order to choose the correct magnetic configuration we relaxed the structures of each MetBz$_2$ molecule by using the D_{6h} symmetry. Then, we fix the MetBz structures and move the benzene ring. Two degrees of freedom were considered. The first one is a displacement of the second benzene ring over the MetBz complex keeping it parallel to the first benzene. The second rotational degree of freedom is realized by rotation of the second benzene ring around the transition metal atom with fixed Met-Bz distance. During the investigations we use the same exchange-correlation potentials and the basis sets as for MetBz complexes.
Displacement: The schematic structure of the MetBz molecule and the starting configuration of the aromatic ring are shown in the left-upper corner of Fig. 4.7. The center

of gravity of the benzene was changed in the positive quarter of the xy plane. A grid of 6×6 points with steps of 0.5 Å for each axis was chosen for the potential energy surface calculations. The total energy of the MetBz$_2$ was transformed to the binding energy, which is defined as the energy required to dissociate the MetBz$_2$ molecule into individual benzene and MetBz complex:

$$E_{BE}^{MetBz_2} = E_{MetBz_2} - E_{MetBz} - E_{Bz}, \qquad (4.3)$$

where E_{Bz}, E_{MetBz_2} and E_{MetBz} are the total energies of the benzene ring, MetBz$_2$ and MetBz molecules, respectively.

Because of the similar potential energy surfaces, we can combine MetBz$_2$ molecules in the following three groups: (G1) - early transition metal-benzene complexes of Sc, Ti,
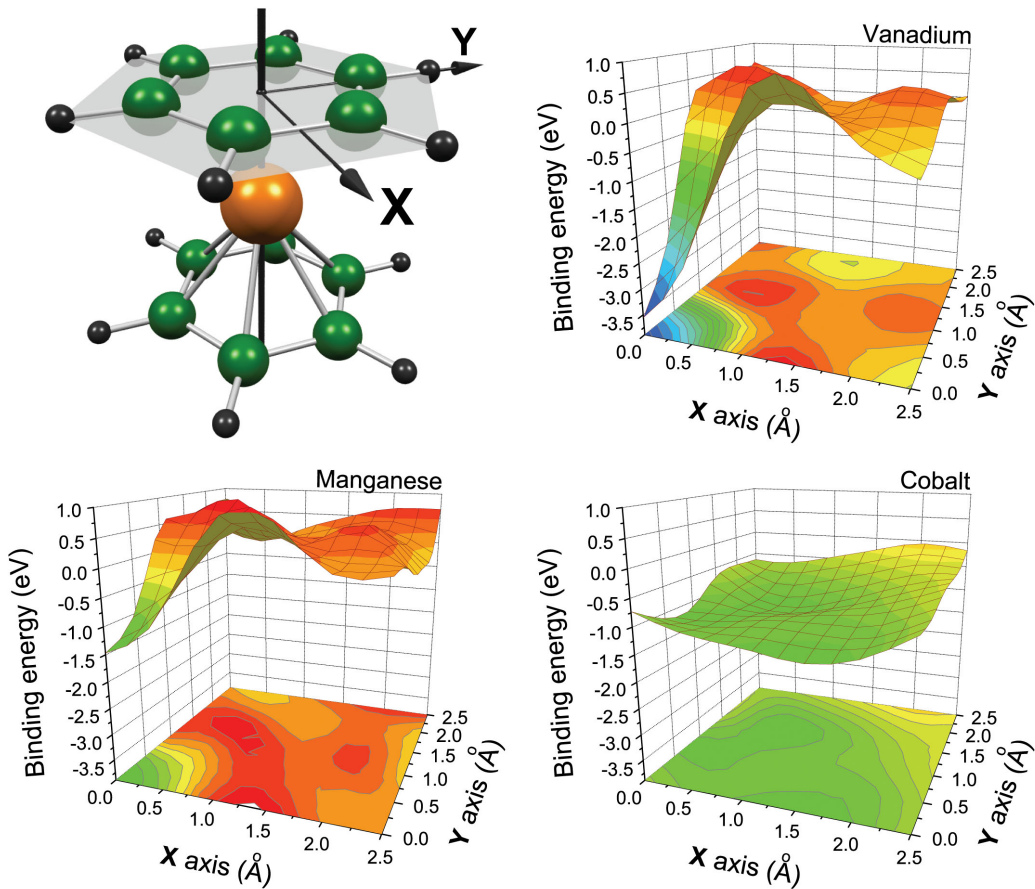
Figure 4.7: Potential energy surfaces of the MetBz$_2$, Met=V, Mn and Co, molecules as a function of the displacement of the second benzene ring in the XY-plane. The schematic structure of the MetBz$_2$ molecule and the position of the X and Y axes are shown in the left-upper corner. Each XY point of the potential surfaces is related to the position of the center of gravity of the second ring. See details in the text.
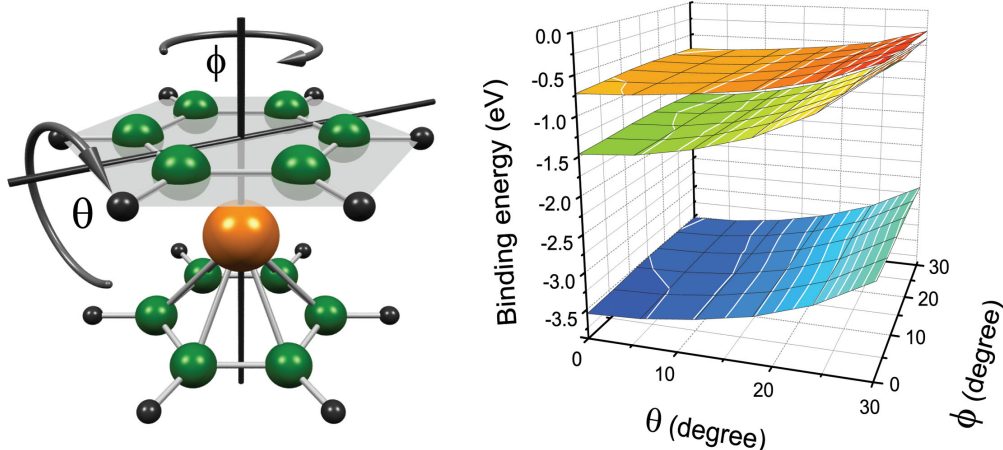
Figure 4.8: Potential energy surfaces of the MetBz$_2$, Met=V, Mn and Co, molecules as a function of the rotation of the second benzene ring by Θ and Φ around the Met atom. Θ and ϕ are shown with respect to the schematic structure of the MetBz$_2$ molecule on the left side. See details in the text.

V and Cr, (G2) - MnBz$_2$ molecule and (G3) - late transition metal-benzene complexes of Fe, Co, and Ni. Fig. 4.7 shows the dependence of the binding energy of the MetBz$_2$ complexes as a function of the position of the second benzene ring for one element of each group, namely V, Mn and Co. One can see that the late transition metal-benzene structures prefer a tilted sandwich structure, in which the transition metal atom is situating below of the C=C bond of the second benzene ring. There is a small energy barrier (>0.2 eV) between two minima related to the nearest Met-C=C structures. The high symmetrical CoBz$_2$ sandwich structure is found to be a transition state. It is 0.57 eV higher in energy then the tilted structure. The ground state of the CoBz$_2$ is a doublet with a binding energy of -1.75 eV that agrees well with previous theoretical results (-1.83 eV [145] and -1.67 eV [147]).

The potential energy surfaces related to the early transition metal-benzene molecules (G1 and G2 groups) have only one energy minimum, which correspond to the sandwich type structure with D_{6h} symmetry (see Fig. 4.7). We present the binding energies, geometrical and magnetic properties of the stable MetBz$_2$, Met=Sc-Mn sandwiches after full optimization in Table 4.2. In general, our data are in good agreement with previous results [145].

The MetBz$_2$, Met=Sc-Mn molecules prefer the magnetic configurations with smallest multiplicity. Namely, the ground state of TiBz and CrBz is singlet and doublet for ScBz$_2$, VBz$_2$ and MnBz$_2$ complexes. The last three systems have induced magnetic moment on the benzene ring. It is negative for VBz$_2$ (-0.21 μ_B) and MnBz$_2$ (-0.05 μ_B) and positive for ScBz$_2$ (0.54 μ_B). Only the VBz$_2$ molecule keeps the magnetic state during the interaction of the VBz half-sandwich with the benzene ring. While, the other MetBz$_2$ molecules change the magnetic configuration. The largest change occurs for

the $CrBz_2$ system, where the Cr atom had a moment of 5.82 μ_B in the CrBz molecule and no magnetization in the sandwich structure. And, as a result, the geometry is also changing drastically. Namely, the Cr-Bz distance is changing from 2.27 Å (for CrBz) to 1.58 Å (for $CrBz_2$). The full relaxation shows that the hydrogen atoms form a plane which is slightly shifted from the plane formed by the carbon atoms. For all $MetBz_2$ molecules (excluding $ScBz_2$), the H plane is closer to the Met atom, which is a result of an attraction between Met and H atoms. Following the same idea, the Sc H interaction is repulsive.

The potential energy surfaces of the early transition metal sandwiches are very similar. Every plot (see Fig. 4.7) has one well pronounced energy minimum and six energy maxima related to the structure, when the carbon atom of the second ring is situated above the Met atom. The main difference between the $MnBz_2$ molecule and other early transition metal-benzene structures is the ground state binding energy (see Fig. 4.7 and Table 4.2). The $MnBz_2$ sandwich has the smallest binding energy of -1.38 eV, which is about 2 eV smaller than for $TiBz_2$, VBz_2 and $CrBz_2$ molecules and about 1 eV smaller than for $ScBz_2$.

Rotation: The rotational degree of freedom of the second benzene molecule were investigated in the following way: the second ring was rotated with fixed Met-Bz distance around the high symmetry axis (angles ϕ) and around the axis which cross the opposite C-C bonds (angles Θ) as shown in the left part of Fig. 4.8. The potential energy surfaces are shown in the right part of Fig. 4.8 for VBz_2, $MnBz_2$ and $CoBz_2$ molecules as representatives of the groups G1, G2 and G3, respectively. Interestingly, for all transition metal-benzene complexes the potential surfaces are very flat. Moreover, the rotation around the high symmetry axis costs little energy of 50 meV for all complexes. The variation of the Θ angle costs more energy (about 30 meV for each of the 6 degrees for Met=Sc-Mn). Nevertheless, it is still small in comparison to the energy losses via displacement of the benzene ring. Therefore, we can assume, that the rotational degree of freedom is responsible for the limitation of the length of the Met_nBz_{n+1} multidecker sandwich structures.

4.2.3 One-dimensional VBz and MnBz wires

In the next step of our investigation, we analyze the electronic properties of the infinite MetBz wires. We consider only early transition metal complexes with Met=Sc-Mn, which can potentially form multidecker structures. The Perdew-Wang [48] GGA exchange-correlation functional was used. In Table 4.3 the calculated data of the magnetic moment per unit cell (m_{Cell}) and the magnetic moment on the Met atom (m_{Cell}), the Met-Bz distance (d_{Met-Bz}), the magnetic phase and character of the band structure, band gap (E_g) and spin-flip gap (Δ_s) for the relaxed MetBz wires are summarized. First of all, our optimized structures of the infinite MetBz chains are in good agreement with other studies [112, 162]. One can see that practically all magnetic phases can be realized in these systems. Namely, TiBz is a metallic antiferromagnet, ScBz and CrBz are nonmagnetic materials with metallic and semiconductor type band structure, respectively, and VBz together with MnBz are ferromagnetic half-metals.

Table 4.3: The phase and character of the band structure, distance between transition metal atom and benzene ring (d_{Met-Bz}), magnetic moment per unit cell (m_{Cell}) and magnetic moment on the Met atom (m_{Met}), band gap (E_g) and spin-flip gap (Δ_s) for the MetBz, Met=Sc-Mn infinite wires.

Method	ScBz	TiBz	VBz	CrBz	MnBz
phase	NM	AFM	FM	NM	FM
	metal	metal	half-metal	semiconductor	half-metal
d_{Met-Bz} (Å)	1.91	1.80	1.69	1.65	1.68
m_{Cell} (μ_B)		0	1		1
m_{Met} (μ_B)		1.21	1.28		1.25
E_g (eV)			1.18 (majority)	0.96	1.16 (minority)
Δ_s (eV)			0.12		0.17

The last two chains are very interesting since they can be used as spin-filters. The electronic structure of these systems has metallic behavior for one spin channel and a band gap for the other spin channel. Therefore, only electrons with one spin-polarization are transmitted through the wire. The VBz and MnBz chains have 1.28 eV majority gap and 1.25 eV minority gap, respectively. The spin-flip gaps, which are defined as the energy difference between the Fermi level and the top of the valence band of the spin-channel with semiconducting behavior, are similar for both wires.

The longitudinal compressing and stretching of the MetBz wires was also investigated. The dependence of the binding energy from the unit cell length is shown in Fig. 4.9 for all early transition metal-benzene chains. Note, the unit cell length is equal to two Met-Bz distances. The ScBz and CrBz have one well pronounced minimum related to the non-magnetic state. While the TiBz, VBz and MnBz have several phases
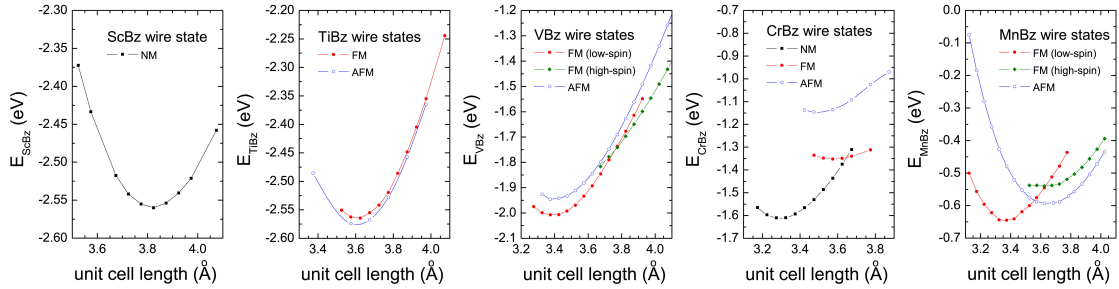

Figure 4.9: Binding energy of the transition metal atom and the benzene ring as a function of the unit cell length for MetBz, Met=Sc-Mn wires. Red and green lines correspond to the low- and high-spin FM states, respectively. The black line refers to the nonmagnetic state. The AFM state is shown by a blue line.
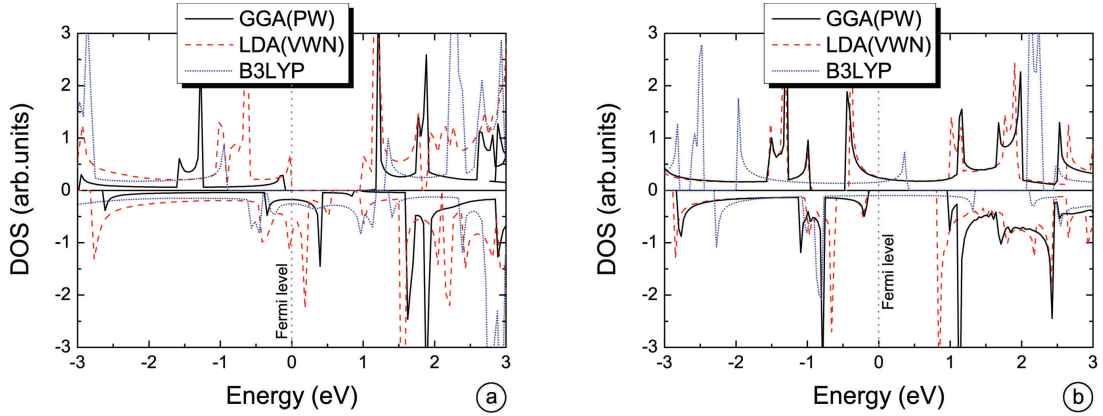
Figure 4.10: The total density of states of the infinite VBz (a) and MnBz (b) chains calculated with different exchange-correlation potentials.

with small differences in energy. The ground state of the TiBz is related to the antiferromagnetic phase, which is only 0.02 eV more preferable than the ferromagnetic one. VBz and MnBz have low-spin and high-spin ferromagnetic phases. The low-spin phase corresponds to the ground state for both VBz and MnBz wires. The antiferromagnetic phase of VBz is about 0.06 eV higher in energy scale for both wires. The MnBz energy minima related to FM and AFM phases are shifted with respect to each other, which allows to expect a magnetoelastic effect.

Taking into account the increasing interest in half-metallic materials, we performed a detailed analysis of the electronic structure of the VBz and MnBz wires. First, in order to verify the validity of the obtained result with respect to a more careful treatment of the on-site correlation effects between d electrons of vanadium and manganese, we performed additional calculations within the LDA and LDA+U scheme, as well as with the hybrid B3LYP exchange-correlation functional. The total density of states (DOS) of the VBz and MnBz wires are shown in Fig. 4.10. One can see that the half-metallic behavior is robust against details of the calculations only for the VBz wire. While the

Table 4.4: Band structure parameters (spin-flip gap Δ_s, direct gap E_g) of the VBz wire together with the lattice constant obtained by different methods.

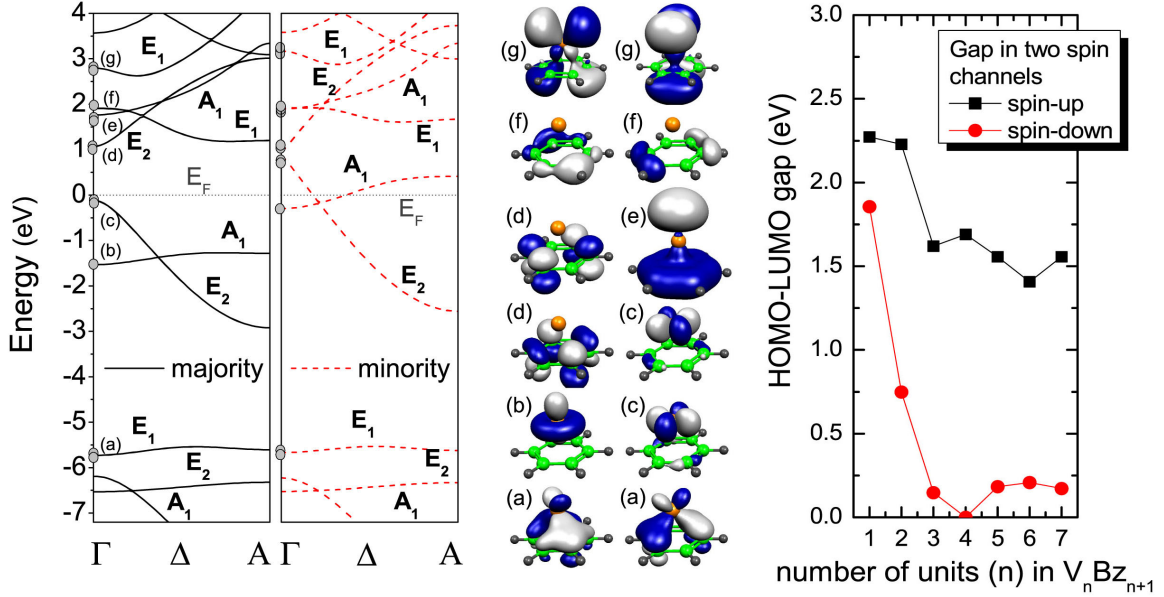| Method	Δ_s, eV	E_g, eV	d_{VBz}, Å
GGA	0.12	1.18	1.695
LDA+U (2 eV)	0.22	1.04	1.663
LDA+U (3 eV)	0.57	1.25	1.676
LDA+U (4 eV)	1.04	1.58	1.696
LDA+U (5 eV)	1.64	2.06	1.720
B3LYP	1.22	2.52	1.760

Figure 4.11: The spin-resolved band structure (left plot). The labels at the band structure refer to crystalline orbitals of the wire calculated for the Γ point. These functions are shown in the center. The corresponding majority and minority spin orbitals have practically the same shape. The right panel shows values of the HOMO-LUMO gap in two spin channels for $V_n(C_6H_6)_{n+1}$ clusters as a function of n.

hybrid B3LYP calculations support the metallic behavior for both spin-channels of the MnBz. The LDA+U calculations with U=1,2,3,4,5 eV shows the same trend as the B3LYP calculations for both wires. Namely, for all U the MnBz wire is metallic and VBz is half-metallic. In Table 4.4, we present the band structure parameters (spin-flip gap Δ_s, direct gap E_g) for the VBz wire together with the optimized lattice constant for different methods. The inclusion of a Hubbard U term results in an increase of the direct band and spin-flip gaps, while the minority bands crossing the Fermi level are unaffected. The B3LYP functional pulls the majority spin bands even stronger away from E_F. In addition, the antiferromagnetic state of the wire was found to be energetically less preferable as compared with the ferromagnetic configuration.

The band structure of the VBz wire and the crystalline orbitals evaluated at the Γ point are shown in Fig. 4.11. The analysis of the bands leads to the following picture of the formation of the ground state. The fully occupied bands below -6 eV with respect to E_F arise from the benzene orbitals which are not spin-split and thus play no role in the formation of the magnetic state. For energies above -6 eV the wire bands are formed from the hybridized states of vanadium and benzene, i.e. from molecular orbitals of the V-Bz cluster. The strong crystalline field splits the vanadium $3d$ states to the singlet A_1 state ($d_{3z^2-r^2}$) and two doublets, of E_1 (d_{xz}, d_{yz}) and E_2 ($d_{xy}, d_{x^2-y^2}$) symmetry. The doubly degenerate E_1 band just above -6 eV is formed
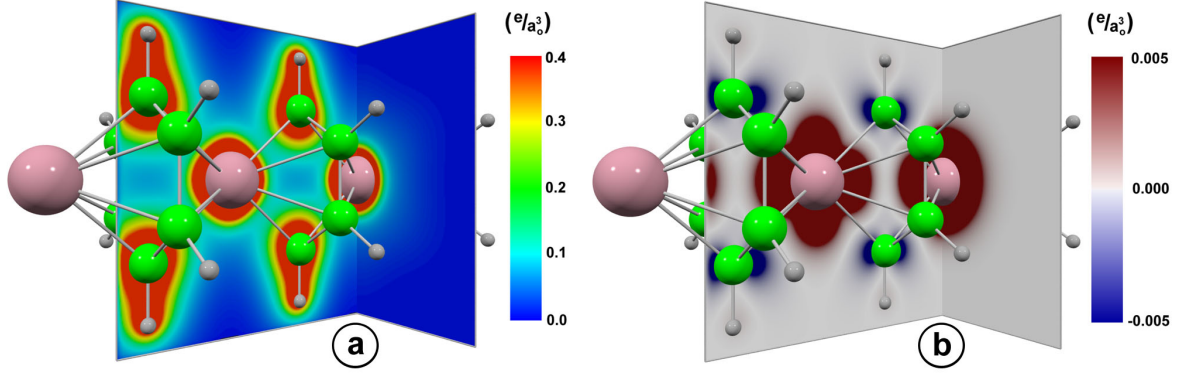
Figure 4.12: Total valence charge-density (a) and spin-density (b) maps for the VBz wire. Local magnetic moments are 1.28 μ_B at V atom, and -0.047 μ_B at each C atom.

mainly from the HOMO and HOMO−1 π-type orbitals of benzene with an admixture of d_{xz}, d_{yz} vanadium states. Due to the strong hybridization effect between the states of the same symmetry, the vanadium d_{xz}, d_{yz} levels are pushed well above the Fermi energy where they are coupled with antibonding benzene LUMO and LUMO−1 states leading to the formation of the two different bands of E_1 symmetry, marked by (f) and (g) in Fig. 4.11. The remaining $d_{3z^2-r^2}$ and $d_{xy}, d_{x^2-y^2}$ vanadium states form two bands nearby the Fermi level, of A_1 and E_2 symmetry, respectively [they are marked by (b) and (c)]. These bands are spin-split. The vanadium atom itself has three $3d$ electrons. It turns out that in the wire the vanadium s states are shifted above E_F and are responsible for the formation of the A_1 band labelled as (e) in Fig. 4.11. Thus, two electrons from s orbitals of vanadium move to the $3d$ shell and five electrons in total wish to occupy three levels (A_1 and E_2) which are available per spin. Finally, the majority spin electrons fill two bands of A_1 and E_2 symmetry completely which therefore are placed below E_F. The remaining two electrons of each unit cell are redistributed among the minority spin A_1 and E_2 bands both of which are crossing the Fermi level. The semiconductor gap in the majority spin channel is formed between two different E_2 bands one of which originates mainly from $d_{xy}, d_{x^2-y^2}$ vanadium states while the upper one comes from the LUMO and LUMO−1 antibonding π^* states of benzene.

We show in Fig. 4.12 the total valence charge density ($\rho_\uparrow + \rho_\downarrow$) and the spin-density ($\rho_\uparrow - \rho_\downarrow$) contour plots for the ferromagnetic V-Bz wire. The density plots are given for two planes: along the wire and perpendicular to it. The electronic charge density in the V-Bz bond critical point is 0.132 e/a_0^3. According to the Bader analysis [163] of the topology of the charge density, the covalent type of bonding is predominant. The vanadium atom is charged negatively ($-0.22e$) due to a charge transfer to benzene that agrees with the findings of Ref. [164], which indicates the presence of an ionic type of bonding. The magnetic density map (Fig. 4.12(b)) shows a quite localized positive magnetic moment at the V atom ($+1.28\ \mu_B$) and a small negative magnetic

moment ($-0.28\ \mu_B$) redistributed over six carbon atoms. Our value of the magnetic moment at the V atom agrees well with the theoretical data of Ref. [164] obtained for finite $V_n Bz_{n+1}$ complexes where these values varied from 1.15 μ_B up to 1.36 μ_B depending on the complex size and the vanadium position in the system. The total magnetic moment of the wire unit cell is equal to 1.0 μ_B. The same integer value of the total magnetic moment was obtained in EPR measurements [156, 157] as well as in the calculations performed for the single V-Bz and multidecker $V_n Bz_{n+1}$ clusters with $n \leq 6$ [164, 165] and VBz infinite wires [166].

Finally, we have found that the half-metallic electronic behavior of the infinite 1D VBz wire is conserved in the $V_n Bz_{n+1}$ molecules of finite length with n≤6. One can see in the right panel of Fig. 4.11, that the HOMO-LUMO gap for the minority spin channel is 1 order of magnitude smaller than the gap in the majority spin channel for clusters with $n \geq 3$. Therefore, we can suggest, that these molecular wires, which have already been synthesized [110, 111], act as highly effective spin filters.

5 Electronic transport in non-collinear magnetic systems with translation invariance

The investigation of the electronic transport through a nanoscale device is a challenging problem. The size of the system is comparable to the Fermi wavelength of the conduction electrons so that the effective-mass approximation is no longer valid. The electrons are scattered by only a few atoms, therefore their arrangement and the electronic structure of the system must be taken into account. As was shown in previous sections, DFT based methods are quite successful for molecules or periodic systems. But, if the system becomes open and an external bias is applied, a more sophisticated *ab initio* treatment is required.

Presently three conceptually quite different schemes of describing electric transport in terms of *ab initio* like methods are available, namely those based on the linearized Boltzmann equation [167, 168], the Kubo-Greenwood equation [3] and the Landauer-type approach [8, 9]. The use of the Boltzmann approach is based on the assumption that the conduction electrons are scattered incoherently at the defects in the sample. The mean free path is short with respect to the characteristic size of the sample. Phase information is lost. Using the Kubo formalism the conductivity is evaluated fully quantum mechanically by the current-current correlation function for the ground state. The formalism gives the transport coefficient in the linear response regime and there are no restrictions concerning the strength of the scattering occurring in the system. Nevertheless, the Kubo formalism cannot be applied when one analyzes non-linear responses, which is beyond its scope [4]. The Landauer-type approaches describe systems in which the nanoscopic conductor acts as a quantum mechanical scatterer for the electrons coming in from one lead and moving out at another. For open systems, the Keldysh formalism [7] is combined with the Landauer-Büttiker formalism [8] by imposing a certain boundary condition. This combination is very often called non-equilibrium Green's function (NEGF) method.

In this chapter, we will concentrate our attention on the last transport scheme. We restate and generalize the non-equilibrium Green's function method for non-collinear magnetic systems with translation invariance. In spite of the large number of papers and implementations of the NEGF method [169, 170, 171, 172, 173, 174, 175, 176] in existing LCAO codes, the last two problems were omitted. Within the chapter, we will mainly follow the arguments presented by M. Branbyge and co-authors in Ref. [170] and M. Paulsson in his introductory paper on the NEGF [177]. In the end
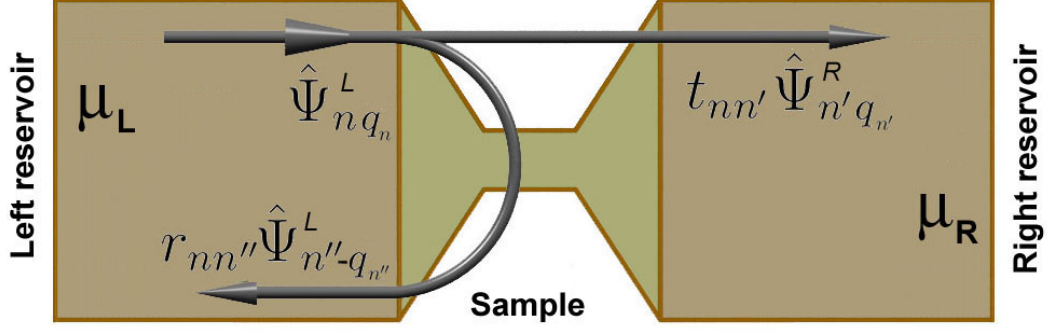
Figure 5.1: Schematic illustration of incoming $\hat{\Psi}^L_{n,q_n}$, outgoing reflected $\hat{\Psi}^L_{n'',-q_{n''}}$ and transmitted $\hat{\Psi}^R_{n',q_{n'}}$ wavefunctions scattered at the mesoscopic sample. The system consists of three regions: mesoscopic sample and two reservoirs with different chemical potentials μ_L and μ_R for left and right reservoirs, respectively. For the meaning of n, n', n'', q, $r_{nn''}$ and $t_{nn'}$, see text.

of the chapter, we are going to apply our method to a perfect graphene sheet and to a one-dimensional iron wire.

5.1 Landauer approach

The Landauer-type formalism considers a mesoscopic sample connected to two electron reservoirs in the form of macroscopic metal contacts (see Fig. 5.1). Here, "mesoscopic" means that the size l of the sample region between the two reservoirs is much smaller than the electron relaxation length l_r ($l \ll l_r$). This implies that we can consider elastic scattering in the sample region. Furthermore, since the metal contact is a macroscopic conductor, we can assume that the electrons inside the contacts can move reflectionless. It can be thermalized at the temperature and chemical potential of every contact. Thus, all electrons entering from the contacts are distributed according to the Fermi- Dirac distribution $f(\varepsilon)$ of the given reservoirs.

Since the scattering is elastic, an incoming wave at some energy ε from the left lead will give rise to a coherent superposition with outgoing reflected and transmitted states of the same energy ε:

$$\hat{\Psi}^L_{n,q_n} - \sum_{n''} r_{nn''}(\varepsilon)\hat{\Psi}^L_{n'',-q_{n''}} + \sum_{n'} t_{nn'}(\varepsilon)\hat{\Psi}^R_{n',q_{n'}}. \tag{5.1}$$

Here $r_{nn''}(\varepsilon)$ is the reflection coefficient between state n with wave vector q_n of an incoming electron and state n'' with wave vector $q_{n''}$ of a reflected electron at energy ε, and $t_{nn'}(\varepsilon)$ is a transmission coefficient between the incoming state nq_n and the transmitted state $n'q_{n'}$ at the same energy.

Thus, the transmitted current density at energy ε and state nq_n is given by:

$$j^t_{n,q_n}(\varepsilon) = \sum_{n'} \|t_{nn'}(\varepsilon)\|^2 j_{n',q_{n'}}(\varepsilon), \qquad (5.2)$$

where $j_{n',q_{n'}}(\varepsilon)$ is a current density for the state n' in the right lead.

It's known that a uniform electron gas with N electrons per unit length moving with velocity v carries a current eNv. In such case, the current propagating in a particular mode n per unit of length is given by the group velocity which in turn is given by the derivative of the dispersion relation for band n

$$j_{n,q_n}(\varepsilon) = ev_{q_n}(\varepsilon_n)f(\varepsilon_n) = \frac{e}{\hbar}\frac{\partial\varepsilon_n}{\partial q}f(\varepsilon_n), \qquad (5.3)$$

where $f(\varepsilon_n)$ is the Fermi-Dirac distribution function, defined as

$$f(\varepsilon_n) = \frac{1}{1 + e^{(\varepsilon_n - \varepsilon_F)/kT}}, \qquad (5.4)$$

here ε_F is the Fermi energy and T is the temperature.

Therefore, the total current from the left to the right reservoirs is

$$\begin{aligned}
I^t_{L\to R} &= \int dq \sum_n j^t_{n,q_n}(\varepsilon) = \int dq \sum_{n,n'} \|t_{nn'}(\varepsilon)\|^2 j_{n',q_{n'}}(\varepsilon) \\
&= \frac{e}{\hbar}\int dq \sum_{n,n'} \|t_{nn'}(\varepsilon)\|^2 \frac{\partial\varepsilon_{n'}}{\partial q} f(\varepsilon_{n'} - \mu_L). \qquad (5.5)
\end{aligned}$$

Now, we are converting the integral over q into an energy integration using the density of states $\rho(\varepsilon)$ and taking into account that for one-dimensional systems $\rho(\varepsilon) = \left(\frac{\partial\varepsilon}{\partial q}\right)^{-1}$ we get

$$\begin{aligned}
I^t_{L\to R} &= \frac{e}{\hbar}\int_{-\infty}^{\infty} d\varepsilon\,\rho(\varepsilon)\frac{\partial\varepsilon}{\partial q}f(\varepsilon - \mu_L)\sum_{n,n'} \|t_{nn'}(\varepsilon)\|^2 \qquad (5.6) \\
&= \frac{e}{\hbar}\int_{-\infty}^{\infty} d\varepsilon\left(\frac{\partial\varepsilon}{\partial q}\right)^{-1}\frac{\partial\varepsilon}{\partial q}f(\varepsilon - \mu_L)\sum_{n,n'} \|t_{nn'}(\varepsilon)\|^2 \qquad (5.7) \\
&= \frac{e}{h}\int_{-\infty}^{\infty} d\varepsilon\, f(\varepsilon - \mu_L)\sum_{n,n'} \|t_{nn'}(\varepsilon)\|^2 \qquad (5.8) \\
&= \frac{e}{h}\int_{-\infty}^{\infty} d\varepsilon\, f(\varepsilon - \mu_L)\sum_{n} T_n(\varepsilon), \qquad (5.9)
\end{aligned}$$

here, we define the transmission per conduction channel n as $T_n(\varepsilon)$ and the Fermi-Dirac distribution function $f(\varepsilon - \mu_L)$ implies that the left electron reservoir injects electrons into the right-moving modes of the left lead up to the chemical potential μ_L.

In the same way, we can find the total current from the right to the left contact:

$$I_{R \to L}^t = \frac{e}{h} \int_{-\infty}^{\infty} d\varepsilon f(\varepsilon - \mu_R) \sum_{n',n} \|t_{n'n}(\varepsilon)\|^2 = \frac{e}{h} \int_{-\infty}^{\infty} d\varepsilon f(\varepsilon - \mu_R) \sum_{n'} T_{n'}(\varepsilon), \quad (5.10)$$

where $T_{n'}(\varepsilon)$ is the transmission probability of channel n' of the right lead.

Because of time inversion symmetry, the transmission probability from the left to the right contact, $t_{nn'}$ is equal to the amplitude $t_{n'n}$ from right to left reservoir. Thus, the relation between the total transmission probabilities from the left and right leads is given by:

$$\sum_n T_n(\varepsilon) = \sum_{n,n'} \|t_{nn'}(\varepsilon)\|^2 = \sum_{n,n'} \|t_{n'n}(\varepsilon)\|^2 = \sum_{n'} T_{n'}(\varepsilon). \quad (5.11)$$

Finally, the total current is given as the difference between the current due to all electrons traveling from L to R and the current due to the electrons traveling vice versa. So, using Eq. (5.6) and (5.10) we obtain

$$I_{tot} = I_{L \to R}^t - I_{R \to L}^t = \frac{e}{h} \int_{-\infty}^{\infty} d\varepsilon \left[\sum_n T_n(\varepsilon) \right] (f(\varepsilon - \mu_L) - f(\varepsilon - \mu_R)). \quad (5.12)$$

Identifying the Fermi-Dirac distribution as a step-function and the difference in the chemical potentials as the applied voltage $eV = \mu_L - \mu_R$, one obtains the following relation for the conductance

$$G = \frac{e^2}{h} \sum_n T_n(eV). \quad (5.13)$$

The last equation is usually called the Landauer formula [178] for the conductance, the coefficient, however, is only half of the fundamental conductance quantum $G_0 = 2e^2/h$. In the case of a spin-degenerate system the transmission for both spin-channels are equal, so that a factor of two appears.

5.2 Non-equilibrium Green's function formalism

The formalism we have discussed so far left out the problem of how to find the transmission T_n matrix for each channel n of a realistic system and how this transmission depends on the applied bias. A solution can be found if we combine the non-equilibrium Green's function approach with the Kohn-Sham single-particle description.

5.2.1 Hamiltonian, overlap matrix and Green's function of the system

The system under consideration consists of three parts (see Fig. 5.2), namely two semi-infinite electrodes (left and right) and the central region. We assume that the

central region is large enough to avoid interactions between the left and right leads. It includes parts from the leads with bulk properties and the scattering region.

When the system is translationally invariant in the planes perpendicular to the transport direction, for the perpendicular components of any $\vec{q}$ point the Hamiltonian is assumed to be given by the matrix:

$$\hat{H}_{\vec{q}} = \begin{bmatrix} \hat{H}_{L,\vec{q}} & \hat{V}_{L,\vec{q}} & 0 \\ \hat{V}_{L,\vec{q}}^{\dagger} & \hat{H}_{C,\vec{q}} & \hat{V}_{R,\vec{q}}^{\dagger} \\ 0 & \hat{V}_{R,\vec{q}} & \hat{H}_{R,\vec{q}} \end{bmatrix}, \tag{5.14}$$

where for matter of simplicity the notation $\vec{q} = \vec{q}_{\perp}$ is used. $\hat{H}_{C,\vec{q}}$ is a Hamiltonian of the central region, $\hat{V}_{L/R,\vec{q}}$ describes the interaction between the central region and the left/right contact and $\hat{H}_{L,\vec{q}}$ and $\hat{H}_{R,\vec{q}}$ are the Hamiltonians of the semi-infinite left and right electrodes, respectively. If we partition the leads into planes of unit cells and assume that every plane is interacting only with the nearest neighbor plane (as shown in Fig. 5.2), the Hamiltonian of the electrodes will look like:

$$\hat{H}_{\vec{q}}^{L} = \begin{bmatrix} \ddots & \ddots & & 0 \\ \ddots & \hat{H}_{l,\vec{q}} & \hat{H}_{ll,\vec{q}} & \\ & \hat{H}_{ll,\vec{q}}^{\dagger} & \hat{H}_{l,\vec{q}} & \hat{H}_{ll,\vec{q}} \\ 0 & & \hat{H}_{ll,\vec{q}}^{\dagger} & \hat{H}_{l,\vec{q}} \end{bmatrix} \quad \text{and} \quad \hat{H}_{\vec{q}}^{R} = \begin{bmatrix} \hat{H}_{r,\vec{q}} & \hat{H}_{rr,\vec{q}}^{\dagger} & & 0 \\ \hat{H}_{rr,\vec{q}} & \hat{H}_{r,\vec{q}} & \hat{H}_{rr,\vec{q}}^{\dagger} & \\ & \hat{H}_{rr,\vec{q}} & \hat{H}_{r,\vec{q}} & \ddots \\ 0 & & \ddots & \ddots \end{bmatrix}. \tag{5.15}$$

The wave function $|\hat{\Psi}_{\vec{q}}\rangle$ of the system can also be positioned into a left ($|\hat{\Psi}_{L,\vec{q}}\rangle$), a central ($|\hat{\Psi}_{C,\vec{q}}\rangle$) and a right ($|\hat{\Psi}_{R,\vec{q}}\rangle$) block such that the Schrödinger equation is of the form:

$$\begin{bmatrix} \hat{H}_{L,\vec{q}} & \hat{V}_{L,\vec{q}} & 0 \\ \hat{V}_{L,\vec{q}}^{\dagger} & \hat{H}_{C,\vec{q}} & \hat{V}_{R,\vec{q}}^{\dagger} \\ 0 & \hat{V}_{R,\vec{q}} & \hat{H}_{R,\vec{q}} \end{bmatrix} \begin{pmatrix} |\hat{\Psi}_{L,\vec{q}}\rangle \\ |\hat{\Psi}_{C,\vec{q}}\rangle \\ |\hat{\Psi}_{R,\vec{q}}\rangle \end{pmatrix} = \varepsilon_{\vec{q}} \begin{pmatrix} |\hat{\Psi}_{L,\vec{q}}\rangle \\ |\hat{\Psi}_{C,\vec{q}}\rangle \\ |\hat{\Psi}_{R,\vec{q}}\rangle \end{pmatrix}. \tag{5.16}$$

Now, we can find the relations between the wave functions of the central region and the leads. From the first and third rows of Eq. (5.16) we can obtain

$$\hat{H}_{L,\vec{q}}|\hat{\Psi}_{L,\vec{q}}\rangle + \hat{V}_{L,\vec{q}}|\hat{\Psi}_{C,\vec{q}}\rangle = \varepsilon_{\vec{q}}|\hat{\Psi}_{L,\vec{q}}\rangle \longrightarrow$$

$$|\hat{\Psi}_{L,\vec{q}}\rangle = \left[z_{\vec{q}} - \hat{H}_{L,\vec{q}}\right]^{-1} \hat{V}_{L,\vec{q}}|\hat{\Psi}_{C,\vec{q}}\rangle, \tag{5.17}$$

$$\hat{V}_{R,\vec{q}}|\hat{\Psi}_{C,\vec{q}}\rangle + \hat{H}_{R,\vec{q}}|\hat{\Psi}_{R,\vec{q}}\rangle = \varepsilon_{\vec{q}}|\hat{\Psi}_{R,\vec{q}}\rangle \longrightarrow$$

$$|\hat{\Psi}_{R,\vec{q}}\rangle = \left[z_{\vec{q}} - \hat{H}_{R,\vec{q}}\right]^{-1} \hat{V}_{R,\vec{q}}|\hat{\Psi}_{C,\vec{q}}\rangle, \tag{5.18}$$

$$z_{\vec{q}} = \varepsilon_{\vec{q}} + i\delta. \tag{5.19}$$

At this stage, we can introduce the Green's function (GF) as a solution of the inhomogeneous Schrödinger equation
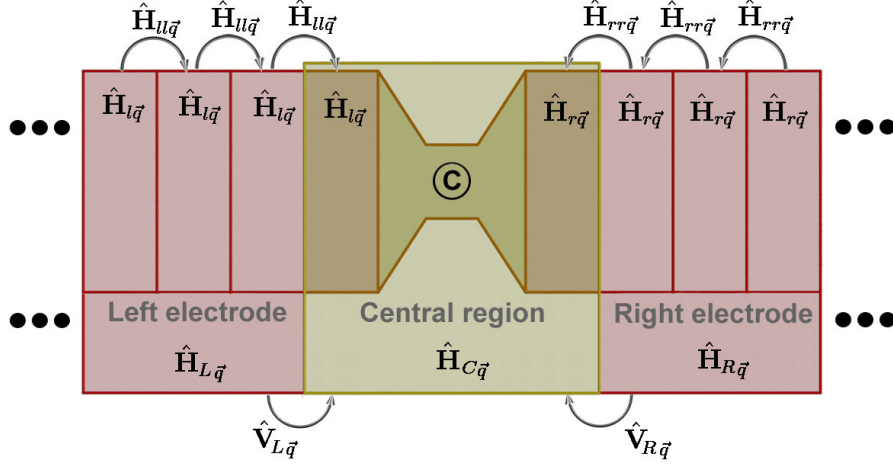
Figure 5.2: Schematic drawing of a system composed of two left and right semi-infinite leads and a central region. The central region includes the interface region so that the left and right leads have bulk properties.

$$(z - H)G(z) = I, \qquad z = \varepsilon + i\delta. \tag{5.20}$$

Depending on the sign of δ we get two different side limits, related to outgoing and incoming waves in the contacts, which usually are called the retarded ($\delta > 0$) and the advanced ($\delta < 0$) Green's function.

Therefore, we can rewrite the Eqs. (5.17) and (5.18) in terms of the unperturbed Green's function of the left/right semi-infinite electrode

$$|\hat{\Psi}_{L,\vec{q}}\rangle = \hat{g}_{L,\vec{q}} \hat{V}_{L,\vec{q}} |\hat{\Psi}_{C,\vec{q}}\rangle \tag{5.21}$$

$$|\hat{\Psi}_{R,\vec{q}}\rangle = \hat{g}_{R,\vec{q}} \hat{V}_{R,\vec{q}} |\hat{\Psi}_{C,\vec{q}}\rangle, \tag{5.22}$$

where

$$\hat{g}_{L/R,\vec{q}} = \left(z - \hat{H}_{L/R,\vec{q}}\right)^{-1}. \tag{5.23}$$

The retarded ($\hat{G}_{\vec{q}}^{+}$) and the advanced ($\hat{G}_{\vec{q}}^{-}$) Green's function can be defined in terms of wave functions (Eq. (3.1)) by using the so-called spectral resolution

$$
\begin{aligned}
\hat{G}_{\vec{q}}^{\pm}(\vec{r}, \varepsilon) &= \sum_{n} f_{n\vec{q}} \frac{\hat{\Psi}_{nq}(\vec{r}) \otimes \hat{\Psi}_{nq}^{\dagger}(\vec{r})}{\varepsilon - \varepsilon_{n} \pm i\eta} = \sum_{u, \mu I_{\mu} \nu I_{\nu}} \left[\sum_{n} f_{n\vec{q}} \frac{\hat{c}_{n\vec{q}\mu I_{\mu}} \otimes \hat{c}_{n\vec{q}\nu I_{\nu}}^{\dagger}}{\varepsilon - \varepsilon_{n} \pm i\eta} \right] \\
&\times \phi_{I_{\mu}}(\vec{r} - \vec{d}_{\mu}) \phi_{I_{\nu}}(\vec{r} - \vec{R}_{u} - \vec{d}_{\nu}) e^{-i\vec{q} \cdot (\vec{d}_{\mu} - \vec{R}_{u} - \vec{d}_{\nu})} \\
&= \sum_{u\mu I_{\mu} \nu I_{\nu}} \hat{G}_{\vec{q}\mu I_{\mu}\nu I_{\nu}}^{\pm}(\varepsilon) \phi_{I_{\mu}}(\vec{r} - \vec{d}_{\mu}) \phi_{I_{\nu}}(\vec{r} - \vec{R}_{u} - \vec{d}_{\nu}) e^{-i\vec{q} \cdot (\vec{d}_{\mu} - \vec{R}_{u} - \vec{d}_{\nu})}, \tag{5.24}
\end{aligned}
$$

where the $\hat{\mathbf{G}}^{\pm}_{\vec{q}\mu I_\mu \nu I_\nu}(\varepsilon)$ is an energy dependent matrix element, $f_{n\vec{q}} = f(\varepsilon_{n\vec{q}} - \varepsilon_F)$ is the Fermi-Dirac distribution function and the $\{\hat{c}_{n\vec{q}\mu I_\mu}\}$ are the expansion coefficients, introduced in Eq. (3.1) of the Chapter 3.

From Eq. (5.24), the relation between the matrix elements of the retarded and advanced Green's functions is

$$\left(\hat{\mathbf{G}}^{+}_{\vec{q}}\right)^\dagger = \hat{\mathbf{G}}^{-}_{\vec{q}} \quad \text{or equivalently} \quad \left(\hat{\mathbf{G}}^{+}_{\vec{q}\nu I_\nu \mu I_\mu}\right)^* = \hat{\mathbf{G}}^{-}_{\vec{q}\mu I_\mu \nu I_\nu}. \tag{5.25}$$

Special care has to be taken if the basis set is non-orthogonal. In this particular case we have to introduce the Hamiltonian and overlap matrices

$$\hat{\mathbf{H}}_{\vec{q}} = \begin{bmatrix} \hat{\mathbf{H}}_{L,\vec{q}} & \hat{\mathbf{V}}_{L,\vec{q}} & 0 \\ \hat{\mathbf{V}}^\dagger_{L,\vec{q}} & \hat{\mathbf{H}}_{C,\vec{q}} & \hat{\mathbf{V}}^\dagger_{R,\vec{q}} \\ 0 & \hat{\mathbf{V}}_{R,\vec{q}} & \hat{\mathbf{H}}_{R,\vec{q}} \end{bmatrix}, \quad \text{and} \quad \hat{\mathbf{S}}_{\vec{q}} = \begin{bmatrix} \hat{\mathbf{S}}_{L,\vec{q}} & \hat{\mathbf{S}}_{LC,\vec{q}} & 0 \\ \hat{\mathbf{S}}^\dagger_{LC,\vec{q}} & \hat{\mathbf{S}}_{C,\vec{q}} & \hat{\mathbf{S}}^\dagger_{RC,\vec{q}} \\ 0 & \hat{\mathbf{S}}_{RC,\vec{q}} & \hat{\mathbf{S}}_{R,\vec{q}} \end{bmatrix}, \tag{5.26}$$

where

$$\begin{aligned} \hat{\mathbf{H}}_{i,\vec{q}} &= \langle \hat{\Psi}_{i,\vec{q}} | \hat{H}_{i,\vec{q}} | \hat{\Psi}_{i,\vec{q}} \rangle, \quad i = \{L, C, R\}; \\ \hat{\mathbf{V}}_{L,\vec{q}} &= \langle \hat{\Psi}_{L,\vec{q}} | \hat{V}_{L,\vec{q}} | \hat{\Psi}_{C,\vec{q}} \rangle; \\ \hat{\mathbf{V}}_{R,\vec{q}} &= \langle \hat{\Psi}_{R,\vec{q}} | \hat{V}_{R,\vec{q}} | \hat{\Psi}_{C,\vec{q}} \rangle; \end{aligned}$$

$$\begin{aligned} \hat{\mathbf{S}}_{i,\vec{q}} &= \langle \hat{\Psi}_{i,\vec{q}} | \hat{\Psi}_{i,\vec{q}} \rangle, \quad i = \{L, C, R\}; \\ \hat{\mathbf{S}}_{LC,\vec{q}} &= \langle \hat{\Psi}_{L,\vec{q}} | \hat{\Psi}_{C,\vec{q}} \rangle; \\ \hat{\mathbf{S}}_{RC,\vec{q}} &= \langle \hat{\Psi}_{R,\vec{q}} | \hat{\Psi}_{C,\vec{q}} \rangle. \end{aligned}$$

The Schrödinger equation in matrix form is then given by

$$\left[\varepsilon_{\vec{q}} \hat{\mathbf{S}}_{\vec{q}} - \hat{\mathbf{H}}_{\vec{q}}\right] \hat{\mathbf{C}}_{\vec{q}} = 0, \tag{5.27}$$

where $\hat{\mathbf{C}}_{\vec{q}} = \left\{\hat{c}_{n\vec{q}\mu I_\mu}\right\}$ is the vector of wave function expansion coefficients which is different for each $\vec{q}$ state. The matrix elements of the Green's function can be obtained from the equation

$$\left[z\hat{\mathbf{S}}_{\vec{q}} - \hat{\mathbf{H}}_{\vec{q}}\right] \hat{\mathbf{G}}_{\vec{q}} = \mathbf{I}. \tag{5.28}$$

If the Green's function of the whole system is given by

$$\hat{\mathbf{G}}_{\vec{q}} = \begin{bmatrix} \hat{\mathbf{G}}_{L,\vec{q}} & \hat{\mathbf{G}}_{LC,\vec{q}} & \hat{\mathbf{G}}_{LR,\vec{q}} \\ \hat{\mathbf{G}}_{CL,\vec{q}} & \hat{\mathbf{G}}_{C,\vec{q}} & \hat{\mathbf{G}}_{CR,\vec{q}} \\ \hat{\mathbf{G}}_{RL,\vec{q}} & \hat{\mathbf{G}}_{RC,\vec{q}} & \hat{\mathbf{G}}_{R,\vec{q}} \end{bmatrix} \tag{5.29}$$

using Eqs. (5.14), (5.26) and (5.28) the GF for the central region is equal to

$$\hat{\mathbf{G}}_{C,\vec{q}}(z) = \left[z\hat{\mathbf{S}}_{C,\vec{q}} - \hat{\mathbf{H}}_{C,\vec{q}} - \hat{\mathbf{\Sigma}}_{L,\vec{q}}(z) - \hat{\mathbf{\Sigma}}_{R,\vec{q}}(z)\right]^{-1}, \tag{5.30}$$

where

$$\hat{\mathbf{\Sigma}}_{L,\vec{q}}(z) = \left[z\hat{\mathbf{S}}_{L,\vec{q}} - \hat{\mathbf{V}}_{L,\vec{q}}\right]^{\dagger} \hat{\mathbf{g}}_{L,\vec{q}}(z) \left[z\hat{\mathbf{S}}_{L,\vec{q}} - \hat{\mathbf{V}}_{L,\vec{q}}\right], \tag{5.31}$$

$$\hat{\mathbf{\Sigma}}_{R,\vec{q}}(z) = \left[z\hat{\mathbf{S}}_{R,\vec{q}} - \hat{\mathbf{V}}_{R,\vec{q}}\right]^{\dagger} \hat{\mathbf{g}}_{R,\vec{q}}(z) \left[z\hat{\mathbf{S}}_{R,\vec{q}} - \hat{\mathbf{V}}_{R,\vec{q}}\right], \tag{5.32}$$

can formally be interpreted as the self-energies of the left and right electrodes, respectively, and

$$\hat{\mathbf{g}}_{\vec{q}}^{L/R}(z) = (z\hat{\mathbf{S}}_{\vec{q}}^{L/R} - \hat{\mathbf{H}}_{\vec{q}}^{L/R})^{-1} \tag{5.33}$$

is the unperturbed Green's function of the semi-infinite left/right electrode in matrix form.

5.2.2 Response to an incoming wave

If each electrode has a different chemical potential, the response ($|\hat{\Phi}_{n\vec{q}}\rangle$) on the incoming wave ($|\hat{\Psi}_{n\vec{q}}\rangle$) of state n from the lead can be obtained from the equation

$$\hat{H}_{\vec{q}}\left(|\hat{\Phi}_{n\vec{q}}\rangle + |\hat{\Psi}_{n\vec{q}}\rangle\right) = \varepsilon_{\vec{q}}\left(|\hat{\Phi}_{n\vec{q}}\rangle + |\hat{\Psi}_{n\vec{q}}\rangle\right). \tag{5.34}$$

For the injection of the electron from the left electrode the incoming wave and the response are defined as

$$|\hat{\Psi}_{n\vec{q}}\rangle = \begin{pmatrix} |\hat{\Psi}_{L,n\vec{q}}\rangle \\ 0 \\ 0 \end{pmatrix} \quad \text{and} \quad |\hat{\Phi}_{n\vec{q}}\rangle = \begin{pmatrix} |\hat{\Psi}_{LL,n\vec{q}}\rangle \\ |\hat{\Psi}_{CL,n\vec{q}}\rangle \\ |\hat{\Psi}_{RL,n\vec{q}}\rangle \end{pmatrix} \tag{5.35}$$

Thus, the response from the central part can be found from Eqs. (5.14) and (5.34)

$$\left(\hat{H}_{\vec{q}} - \varepsilon_{\vec{q}}\right)|\hat{\Phi}_{n\vec{q}}\rangle = \left(\varepsilon_{\vec{q}} - \hat{H}_{\vec{q}}\right)|\hat{\Psi}_{n\vec{q}}\rangle$$

$$|\hat{\Phi}_{n\vec{q}}\rangle = -\hat{G}_{\vec{q}}\begin{pmatrix} \varepsilon_{\vec{q}} - \hat{H}_{L,\vec{q}} \\ -\hat{V}_{L,\vec{q}}^{\dagger} \\ 0 \end{pmatrix}|\hat{\Psi}_{L,n\vec{q}}\rangle = \hat{G}_{\vec{q}}\begin{pmatrix} 0 \\ \hat{V}_{L,\vec{q}}^{\dagger} \\ 0 \end{pmatrix}|\hat{\Psi}_{L,n\vec{q}}\rangle$$

$$\Rightarrow \quad |\hat{\Psi}_{CL,n\vec{q}}\rangle = \hat{G}_{C,\vec{q}}\hat{V}_{L,\vec{q}}^{\dagger}|\hat{\Psi}_{L,n\vec{q}}\rangle, \tag{5.36}$$

here we take into account that $|\hat{\Psi}_{L,n\vec{q}}\rangle$ is a solution for the Schrödinger equation of the left electrode $(\varepsilon_{\vec{q}} - \hat{H}_{L,\vec{q}})|\hat{\Psi}_{L,n\vec{q}}\rangle = 0$. Similarly the response on the m state of the incoming wave from the right lead is

$$|\hat{\Psi}_{CR,m\vec{q}}\rangle = \hat{G}_{C,\vec{q}}\hat{V}_{R,\vec{q}}^{\dagger}|\hat{\Psi}_{R,m\vec{q}}\rangle \tag{5.37}$$

The wave function in the right electrode $|\hat{\Psi}_{R,\vec{q}}\rangle$ (Eq. (5.22)) can therefore be expressed in terms of the left lead incoming wave $|\hat{\Psi}_{L,\vec{q}}\rangle$:

$$|\hat{\Psi}_{R,\vec{q}}\rangle = \hat{g}_{R,\vec{q}}\hat{V}_{R,\vec{q}}|\hat{\Psi}_{CL,\vec{q}}\rangle = \hat{g}_{R,\vec{q}}\hat{V}_{R,\vec{q}}\hat{G}_{C,\vec{q}}\hat{V}_{L,\vec{q}}^{\dagger}|\hat{\Psi}_{L,\vec{q}}\rangle. \tag{5.38}$$

5.2.3 Density matrix

The basic task in the self-consistent DFT cycle for the system under bias is the calculation of the non-equilibrium charge density in the device region. This charge density can be constructed from the wave functions in the device region by the incoming states of the left and right leads:

$$\hat{\rho} = \hat{\rho}_L + \hat{\rho}_R \tag{5.39}$$

where

$$\hat{\rho}_L = \sum_{n,\vec{q}} |\hat{\Psi}_{CL,n\vec{q}}\rangle\langle\hat{\Psi}_{CL,n\vec{q}}|f(\varepsilon_{n\vec{q}} - \mu_L) \tag{5.40}$$

$$\hat{\rho}_R = \sum_{m,\vec{q}} |\hat{\Psi}_{CR,m\vec{q}}\rangle\langle\hat{\Psi}_{CR,m\vec{q}}|f(\varepsilon_{m\vec{q}} - \mu_R). \tag{5.41}$$

Now, combining the Eqs. (5.36) and (5.40) we obtain

$$\begin{aligned}
\hat{\rho}_L &= \sum_{n\vec{q}} \hat{G}_{C,\vec{q}}\hat{V}_{L,\vec{q}}^{\dagger}\left[|\hat{\Psi}_{L,n\vec{q}}\rangle\langle\hat{\Psi}_{L,n\vec{q}}|\right]\hat{V}_{L,\vec{q}}\hat{G}_{C,\vec{q}}^{\dagger}f(\varepsilon_{n\vec{q}} - \mu_L) \\
&= \sum_{\vec{q}} \int d\varepsilon f(\varepsilon - \mu_L)\hat{G}_{C,\vec{q}}\hat{V}_{L,\vec{q}}^{\dagger}\left[|\hat{\Psi}_{L,n\vec{q}}\rangle\langle\hat{\Psi}_{L,n\vec{q}}|\delta(\varepsilon - \varepsilon_{n\vec{q}})\right]\hat{V}_{L,\vec{q}}\hat{G}_{C,\vec{q}}^{\dagger} \\
&= \frac{i}{2\pi}\sum_{\vec{q}} \int d\varepsilon f(\varepsilon - \mu_L)\hat{G}_{C,\vec{q}}\hat{V}_{L,\vec{q}}^{\dagger}\left[\hat{g}_{L,\vec{q}} - \hat{g}_{L,\vec{q}}^{\dagger}\right]\hat{V}_{L,\vec{q}}\hat{G}_{C,\vec{q}}^{\dagger},
\end{aligned} \tag{5.42}$$

where $\hat{g}_{L,\vec{q}}$ is the spectral resolution of the unperturbed retarded Green's function of the left electrode

$$\hat{g}_{L,\vec{q}} \equiv \hat{g}_{L,\vec{q}}^{+} = \sum_{n} \frac{|\hat{\Psi}_{L,n\vec{q}}\rangle\langle\hat{\Psi}_{L,n\vec{q}}|}{\varepsilon - \varepsilon_l + i\eta} \quad \text{and} \tag{5.43}$$

$$\hat{g}_{L,\vec{q}}^{+} - \left(\hat{g}_{L,\vec{q}}^{+}\right)^{\dagger} = \hat{g}_{L,\vec{q}}^{+} - \hat{g}_{L,\vec{q}}^{-} = 2\pi i\sum_{l} \hat{c}_{l\vec{q}\mu I_{\mu}}^{0} \otimes \hat{c}_{l\vec{q}\nu I_{\nu}}^{0\dagger}\delta(\varepsilon - \varepsilon_l). \tag{5.44}$$

The proof of the last equation is based on the properties of the retarded and advanced Green's functions $G(\varepsilon^{-}) = G^{\dagger}(\varepsilon^{+})$, see Eq. (5.25), and on the Sokhotsky's formula [179]:

$$\lim_{\epsilon \to +0} \frac{1}{x \pm i\epsilon} = \mp i\pi\delta(x) + \mathcal{P}\left(\frac{1}{x}\right). \tag{5.45}$$

Here, we can introduce a new quantity which describes the coupling between left electrode and device region

$$\hat{\Gamma}_{L,\vec{q}} = i\hat{V}_{L,\vec{q}}^{\dagger} \left[\hat{g}_{L,\vec{q}} - \hat{g}_{L,\vec{q}}^{\dagger}\right] \hat{V}_{L,\vec{q}} = i\left[\hat{\Sigma}_{L,\vec{q}} - \hat{\Sigma}_{L,\vec{q}}^{\dagger}\right], \tag{5.46}$$

where $\hat{\Sigma}_{L,\vec{q}}$ is the self-energy of the left electrode (Eq. (5.31)).

In the case that the basis set is non-orthogonal we can use the $\vec{q}$-dependent density matrix (3.7) instead of the density and consider that Eqs. (5.28), (5.31) define the Green's function and self-energy of the left lead in matrix form.

Finally, repeating the same procedure for density coming from the right electrode, the $\vec{q}$-dependent non-equilibrium density matrix has the form:

$$\hat{\mathbf{D}}_{\vec{q}} = \frac{1}{\pi} \int_{-\infty}^{\infty} d\varepsilon \left[\hat{\mathbf{G}}_{\vec{q}}\hat{\mathbf{\Gamma}}_{\vec{q}}^{L}\hat{\mathbf{G}}_{\vec{q}}^{\dagger}f(\varepsilon - \mu_L) + \hat{\mathbf{G}}_{\vec{q}}\hat{\mathbf{\Gamma}}_{\vec{q}}^{R}\hat{\mathbf{G}}_{\vec{q}}^{\dagger}f(\varepsilon - \mu_R)\right]. \tag{5.47}$$

Formally, we can split the $\hat{\mathbf{D}}_{\vec{q}}$ in an "equilibrium" and a "non-equilibrium" part:

$$\hat{\mathbf{D}}_{\vec{q}} = \hat{\mathbf{D}}_{\vec{q}}^{L} + \hat{\Delta}_{\vec{q}}^{RL} \tag{5.48}$$

$$= \frac{1}{\pi} \int_{-\infty}^{\infty} d\varepsilon \hat{\mathbf{G}}_{\vec{q}}\left(\hat{\mathbf{\Gamma}}_{\vec{q}}^{L} + \hat{\mathbf{\Gamma}}_{\vec{q}}^{R}\right)\hat{\mathbf{G}}_{\vec{q}}^{\dagger}f(\varepsilon - \mu_L) \tag{5.49}$$

$$+ \frac{1}{\pi} \int_{-\infty}^{\infty} d\varepsilon \hat{\mathbf{G}}_{\vec{q}}\hat{\mathbf{\Gamma}}_{\vec{q}}^{R}\hat{\mathbf{G}}_{\vec{q}}^{\dagger}\left(f(\varepsilon - \mu_R) - f(\varepsilon - \mu_L)\right), \tag{5.50}$$

or, equivalently,

$$\hat{\mathbf{D}}_{\vec{q}} = \hat{\mathbf{D}}_{\vec{q}}^{R} + \hat{\Delta}_{\vec{q}}^{LR} \tag{5.51}$$

$$= \frac{1}{\pi} \int_{-\infty}^{\infty} d\varepsilon \hat{\mathbf{G}}_{\vec{q}}\left(\hat{\mathbf{\Gamma}}_{\vec{q}}^{L} + \hat{\mathbf{\Gamma}}_{\vec{q}}^{R}\right)\hat{\mathbf{G}}_{\vec{q}}^{\dagger}f(\varepsilon - \mu_R) \tag{5.52}$$

$$+ \frac{1}{\pi} \int_{-\infty}^{\infty} d\varepsilon \hat{\mathbf{G}}_{\vec{q}}\hat{\mathbf{\Gamma}}_{\vec{q}}^{L}\hat{\mathbf{G}}_{\vec{q}}^{\dagger}\left(f(\varepsilon - \mu_L) - f(\varepsilon - \mu_R)\right), \tag{5.53}$$

The equilibrium part of the density matrix

In equilibrium, it is possible to combine the density coming from the left and the right lead. Assuming that there are no states that couple the electrodes via the central region we can write

$$\hat{\mathbf{G}}_{\vec{q}}\left(\hat{\mathbf{\Gamma}}_{\vec{q}}^{L} + \hat{\mathbf{\Gamma}}_{\vec{q}}^{R}\right)\hat{\mathbf{G}}_{\vec{q}}^{\dagger} = i\hat{\mathbf{G}}_{\vec{q}}\left(\left(\hat{\mathbf{\Sigma}}_{\vec{q}}^{L} + \hat{\mathbf{\Sigma}}_{\vec{q}}^{R}\right) - \left(\hat{\mathbf{\Sigma}}_{\vec{q}}^{L} + \hat{\mathbf{\Sigma}}_{\vec{q}}^{R}\right)^{\dagger}\right)\hat{\mathbf{G}}_{\vec{q}}^{\dagger}$$

$$= i\hat{\mathbf{G}}_{\vec{q}}\left(\left(\hat{\mathbf{G}}_{\vec{q}}^{\dagger}\right)^{-1} - \left(\hat{\mathbf{G}}_{\vec{q}}\right)^{-1}\right)\hat{\mathbf{G}}_{\vec{q}}^{\dagger}$$

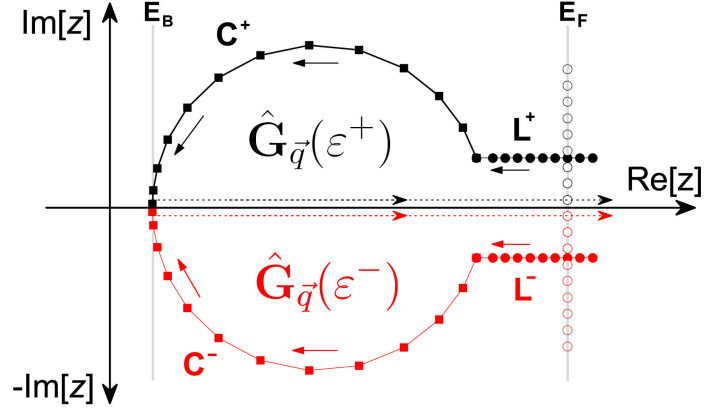$$= i\left(\hat{\mathbf{G}}_{\vec{q}} - \hat{\mathbf{G}}_{\vec{q}}^{\dagger}\right). \tag{5.54}$$

Figure 5.3: Schematic view of the integration contours for the retarded (black color) and the advanced (red color) Green's functions used to calculate the equilibrium part of the $\vec{q}$-dependent density matrix. E_B and E_F are indicating the bottom of the valence band and the Fermi energy respectively. Open circles are related to the Matsubara poles of the Green's functions. Arrows show the direction for integration.

At this stage, it should be noted, that it is impossible to define the density as an imaginary part of the retarded Green's function for a non-collinear magnetic systems. The imaginary part of any complex number is always a real quantity but the matrix element of the density matrix can be complex. Thus, if we take only the imaginary part of the retarded GF we can lose some information about the magnetic properties of the system. One can easily see this from Eq. (3.7).

It is also impossible in the LCAO method to use the way suggested in methods based on spherical approximation of the atom, where the density always can be kept in the local frame for non-colliner magnetic systems.

In the present work, we suggest the way how to overcome this problem. First of all, we divide the integral over energy for the difference of the Green's functions (5.54) into two integrals, one for the retarded GF and one for the advanced GF

$$
\begin{aligned}
\hat{\mathbf{D}}_{\vec{q}}^{L/R} &= \frac{i}{\pi} \int_{-\infty}^{\infty} d\varepsilon \left[\hat{\mathbf{G}}_{\vec{q}}(\varepsilon^+) - \hat{\mathbf{G}}_{\vec{q}}^{\dagger}(\varepsilon^+) \right] f(\varepsilon - \mu_{L/R}) \\
&= \frac{i}{2\pi} \int_{-\infty}^{\infty} d\varepsilon \left[\hat{\mathbf{G}}_{\vec{q}}(\varepsilon^+) - \hat{\mathbf{G}}_{\vec{q}}(\varepsilon^-) \right] f(\varepsilon - \mu_{L/R}) \\
&= \frac{i}{2\pi} \int_{-\infty}^{\infty} d\varepsilon \hat{\mathbf{G}}_{\vec{q}}(\varepsilon^+) f(\varepsilon - \mu) - \frac{1}{\pi} \int_{-\infty}^{\infty} d\varepsilon \hat{\mathbf{G}}_{\vec{q}}(\varepsilon^-) f(\varepsilon - \mu_{L/R}), \quad (5.55)
\end{aligned}
$$

taking into account, that the retarded GF is analytical in the upper half of the complex plane and the advanced one in the lower half. According to the residue theorem, for the complex contour,

$$
\oint dz \hat{\mathbf{G}}(z) f(\varepsilon - \mu) = -2\pi i kT \sum_{z_p} \hat{\mathbf{G}}(z_p), \qquad (5.56)
$$

where T is the temperature and the Matsubara poles are located at energy $z_p = i(2m + 1)\pi kT$, $m=1, 2, ...$ we can perform the integral over the complex contour for every type of Green's function according to equations

$$\int_{EB}^{\infty} d\varepsilon \hat{\mathbf{G}}_{\vec{q}}(\varepsilon^+) f(\varepsilon - \mu) = -\int_{C^++L^+} dz^+ \hat{\mathbf{G}}_{\vec{q}}(z^+) f(z^+ - \mu) - 2\pi i kT \sum_{z_p^+} \hat{\mathbf{G}}(z_p^+) \quad (5.57)$$

$$\int_{EB}^{\infty} d\varepsilon \hat{\mathbf{G}}_{\vec{q}}(\varepsilon^-) f(\varepsilon - \mu) = -\int_{C^-+L^-} dz^- \hat{\mathbf{G}}_{\vec{q}}(z^-) f(z^- - \mu) + 2\pi i kT \sum_{z_p^-} \hat{\mathbf{G}}(z_p^-) \quad (5.58)$$

Now, taking into account that we have a finite number of poles and also a finite number of points on the contours $C^+ + L^+$ and $C^- + L^-$ and assuming the relation between the contours is $z^- = (z^+)^*$, where $z^- \in (C^- + L^-)$ and $z^+ \in (C^+ + L^+)$ (see Fig. 5.3), we finally obtain for the density

$$\hat{\mathbf{D}}_{\vec{q}}^{L/R} = \frac{i}{2\pi} \sum_i \left[w_i^* \hat{\mathbf{G}}_{\vec{q}}^\dagger(z_i^+) - w_i \hat{\mathbf{G}}_{\vec{q}}(z_i^+) \right], \quad \text{where} \quad (5.59)$$

$$w_i = (z_i^+ - z_{i-1}^+) \cdot f(z^+ - \mu_{L/R}) \quad \text{for} \quad z_i^+ \in C^+ + L^+$$

$$w_i = 2\pi i kT \qquad\qquad\qquad \text{for} \quad z_i^+ = z_p^+$$

A similar technique is used for the calculation of the optical conductivity tensor [180].

The non-equilibrium part of the density matrix

The densities $\hat{\Delta}_{\vec{q}}^{RL}$ and $\hat{\Delta}_{\vec{q}}^{LR}$ are non-analytical quantities, since they are related to two different Fermi functions, see e.g. Eq. (5.50). Therefore they must be evaluated by integration close to the real axis using a very fine energy mesh.

Furthermore, because of numerical errors, the results from Eqs. (5.48) and (5.51) are not equivalent. It is therefore reasonable to use a weighted sum,

$$\hat{\mathbf{D}}_{\vec{q}\mu I_\mu \nu I_\nu} = \left(\hat{\mathbf{D}}_{\vec{q}\mu I_\mu \nu I_\nu}^L + \hat{\Delta}_{\vec{q}\mu I_\mu \nu I_\nu}^{RL} \right) w_{\vec{q}\mu I_\mu \nu I_\nu}$$
$$+ \left(\hat{\mathbf{D}}_{\vec{q}\mu I_\mu \nu I_\nu}^R + \hat{\Delta}_{\vec{q}\mu I_\mu \nu I_\nu}^{LR} \right) \left(1 - w_{\vec{q}\mu I_\mu \nu I_\nu,} \right) \quad (5.60)$$

in order to reduce integration error. Taking into account that the trace of the density matrix $\hat{\mathbf{D}}_{\vec{q}\mu I_\mu \nu I_\nu}$ can be interpreted as a $\vec{q}$-resolved charge, we can define the weight as

$$w_{\vec{q}\mu I_\mu \nu I_\nu} = \frac{(\text{Tr}\hat{\Delta}_{\vec{q}\mu I_\mu \nu I_\nu}^{LR})^2}{(\text{Tr}\hat{\Delta}_{\vec{q}\mu I_\mu \nu I_\nu}^{RL})^2 + (\text{Tr}\hat{\Delta}_{\vec{q}\mu I_\mu \nu I_\nu}^{RL})^2}. \quad (5.61)$$

In the case of spin-polarized calculations, the weight for every spin channel has to be calculated independently.

5.2.4 Current and transmission

The current in a system is described by a charge flow. Therefore, we can find the probability current as time derivative of the density in the central region:

$$j \; = \; \frac{\partial \hat{\rho}}{\partial t} = \sum_{i\vec{q}} \frac{\partial \langle \hat{\Psi}_{\vec{q}} | i \rangle \langle i | \hat{\Psi}_{\vec{q}} \rangle}{\partial t}. \tag{5.62}$$

By taking into account that $i\hbar \frac{\partial |\hat{\Psi}_{\vec{q}}\rangle}{\partial t} = \hat{H}_{\vec{q}} |\hat{\Psi}_{\vec{q}}\rangle$ and by grouping together the terms involving the hopping from the left electrode to the central region and the terms involving hopping between the right electrode and the device, we obtain

$$j \; = \; j^L + j^R, \qquad \text{where}$$
$$j^{L/R} \; = \; \frac{i}{\hbar} \sum_{\vec{q}} \left(\langle \hat{\Psi}_{L/R,\vec{q}} | \hat{V}_{L/R\vec{q}} | \hat{\Psi}_{C,\vec{q}} \rangle - \langle \hat{\Psi}_{C,\vec{q}} | \hat{V}^{\dagger}_{L/R,\vec{q}} | \hat{\Psi}_{L/R,\vec{q}} \rangle \right). \tag{5.63}$$

The more detailed derivation of all equation of this section can be found in the work of M. Paulsson [177].

The charge current $i(\varepsilon)$ (at a particular energy point) is the current which can transfer the electron (-e) with the probability equal to the probability current. Therefore, by using Eqs. (5.21), (5.22) and (5.38) we can get the electric current $i^R(\varepsilon)$ flowing from the left electrode to the right,

$$i^R(\varepsilon) \; = \; -\frac{ie}{\hbar} \sum_{\vec{q}} \left(\langle \hat{\Psi}_{R,\vec{q}} | \hat{V}_{R,\vec{q}} | \hat{\Psi}_{C,\vec{q}} \rangle - \langle \hat{\Psi}_{C,\vec{q}} | \hat{V}^{\dagger}_{R,\vec{q}} | \hat{\Psi}_{R,\vec{q}} \rangle \right)$$
$$= \; \frac{e}{\hbar} \sum_{n\vec{q}} \langle \hat{\Psi}_{L,n\vec{q}} | \hat{V}_{L,\vec{q}} \hat{G}^{\dagger}_{C,\vec{q}} \hat{\Gamma}_{R,\vec{q}} \hat{G}_{C,\vec{q}} \hat{V}^{\dagger}_{L,\vec{q}} | \hat{\Psi}_{L,n\vec{q}} \rangle, \tag{5.64}$$

while the total current from the left to the right electrode is given by

$$I^R \; = \; \frac{e}{\hbar} \sum_{\vec{q}} \int_{-\infty}^{\infty} d\varepsilon f(\varepsilon - \mu_L) \sum_n \delta(\varepsilon - \varepsilon_n) \langle \hat{\Psi}_{L,n\vec{q}} | \hat{V}_{L,\vec{q}} \hat{G}^{\dagger}_{C,\vec{q}} \hat{\Gamma}_{R,\vec{q}} \hat{G}_{C,\vec{q}} \hat{V}^{\dagger}_{L,\vec{q}} | \hat{\Psi}_{L,n\vec{q}} \rangle$$
$$= \; \frac{e}{h} \sum_{\vec{q}} \int_{-\infty}^{\infty} d\varepsilon f(\varepsilon - \mu_L) \text{Tr} \left(\hat{G}^{\dagger}_{C,\vec{q}} \hat{\Gamma}_{R,\vec{q}} \hat{G}_{C,\vec{q}} \hat{\Gamma}_{L,\vec{q}} \right). \tag{5.65}$$

Thus, the total current is defined as

$$I \; = \; \frac{e}{h} \sum_{\vec{q}} \int_{-\infty}^{\infty} d\varepsilon \text{Tr} \left[\hat{\Gamma}_{L,\vec{q}} \hat{G}^{\dagger}_{C,\vec{q}} \hat{\Gamma}_{R,\vec{q}} \hat{G}_{C,\vec{q}} \right] \left(f(\varepsilon - \mu_L) - f(\varepsilon - \mu_R) \right), \tag{5.66}$$

which is exactly the Landauer formula, however now $\vec{q}$-resolved:

$$T_{\vec{q}}(\varepsilon) = \text{Tr} \left[\hat{\Gamma}_{L,\vec{q}}(\varepsilon) \hat{G}^{\dagger}_{C,\vec{q}}(\varepsilon) \hat{\Gamma}_{R,\vec{q}}(\varepsilon) \hat{G}_{C,\vec{q}}(\varepsilon) \right]. \tag{5.67}$$

5.2.5 Spin transport

In matrix representation, the transmission for any energy point is given by

$$T(\varepsilon) = \mathrm{Tr}\left[(\hat{\mathbf{\Gamma}}_L(\varepsilon)\hat{\mathbf{G}}_C(\varepsilon))^\dagger \hat{\mathbf{\Gamma}}_R(\varepsilon)\hat{\mathbf{G}}_C(\varepsilon)\right],\tag{5.68}$$

where for matter of simplicity the $\vec{q}$-index was dropped.

Let's consider a particular system where the central region has arbitrary spin polarization and the electrodes have spin polarization along z axis. In such case, the matrices $\hat{\mathbf{\Gamma}}_L$ and $\hat{\mathbf{\Gamma}}_R$ are spin-block diagonal and the Green's function of the central region $\hat{\mathbf{G}}_C$ is a full matrix:

$$\hat{\mathbf{\Gamma}}_{L,R} = \begin{bmatrix} \mathbf{\Gamma}_{L,R}^{\uparrow} & 0 \\ 0 & \mathbf{\Gamma}_{L,R}^{\downarrow} \end{bmatrix} \quad \text{and} \quad \hat{\mathbf{G}}_C = \begin{bmatrix} \mathbf{G}_C^{\uparrow\uparrow} & \mathbf{G}_C^{\uparrow\downarrow} \\ \mathbf{G}_C^{\downarrow\uparrow} & \mathbf{G}_c^{\downarrow\downarrow} \end{bmatrix}\tag{5.69}$$

Based on this equation, we can obtain four independent transmission probabilities describing the transport of the electron from one electrode with spin direction $\pm\vec{z}$ to another with spin direction $\pm\vec{z}$. They contribute to the total transmission additively

$$T = T^{\uparrow\uparrow} + T^{\uparrow\downarrow} + T^{\downarrow\uparrow} + T^{\downarrow\downarrow}.\tag{5.70}$$

In this case the spin-resolved transmission is given by

$$T^{\sigma\sigma'}(\varepsilon) = \mathrm{Tr}\left[(\mathbf{\Gamma}_L^{\sigma}(\varepsilon)\mathbf{G}_C^{\sigma\sigma'}(\varepsilon))^\dagger \mathbf{\Gamma}_R^{\sigma'}(\varepsilon)\mathbf{G}_C^{\sigma\sigma'}(\varepsilon)\right].\tag{5.71}$$

The terms $T^{\uparrow\downarrow}$ and $T^{\downarrow\uparrow}$ are called adiabatic spin-flip transmissions. They are equal to zero if the spin polarization in the central region is also along z axis.

5.3 The application of the NEGF formalism

The theory described above was implemented in the TranSIESTA code [170]. In order to check our implementation we apply the NEGF method to a graphene sheet and to the one-dimensional iron wire.

5.3.1 Graphene sheet

Graphene is a one atom thick plane of carbon atoms which create a honeycomb crystal lattice. The structural setup of the graphene is shown in Fig. 5.4(a). On the other hand, it is the starting point for all calculations on graphite, carbon nanotubes, and fullerenes. In addition, graphene is a perfect system for the verification of our implementation of the translational invariance. Here, we investigate the transport through ideal and defect graphene sheets. Defect in our case means that one carbon layer (in the middle of the scattering region) was replaced by ghost atoms. Such atoms are interpreted as a chemical species with orbitals, but neither pseudopotential nor charge are considered
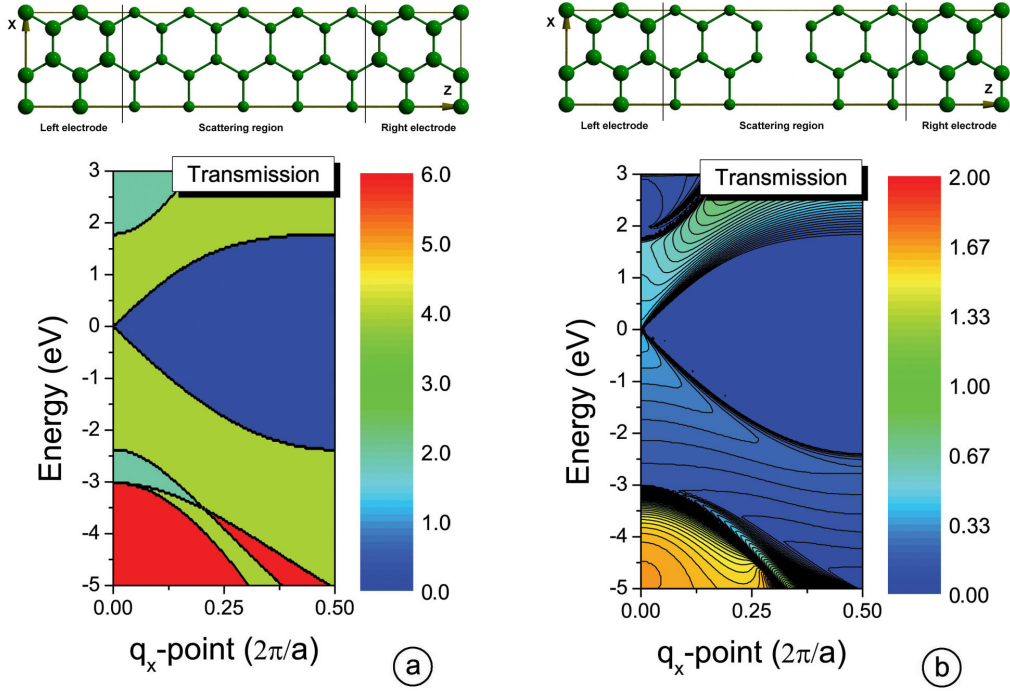
Figure 5.4: The structural setup of the graphene sheet and the q_x- and energy-resolved transmission spectra related to it. (a) - the ideal graphene sheet, (b) - graphene with defect in the middle. The carbon atoms in the electrodes are indicated with slightly larger spheres. Zero corresponds to the Fermi level.

for them. Alternatively, the defect graphene can be considered as a tunnel junction between two semi-infinite graphene electrodes.

Both structural setups of the graphene are shown in Fig. 5.4. The system consists of left and right electrodes and the scattering region in the middle. During the calculation we use the generalized gradient approximation with PBE [52] parametrization for the exchange-correlation potential and double-ζ polarized basis set. The pseudopotential was generated with cut-off radii (in a.u.) 1.2/1.2/1.8/1.9 for $s/p/d/f$ shells, respectively.

The q_x- and energy-resolved transmission spectra for both setups are shown in Fig. 5.4. The transmission probability of the ideal graphene is simply given by the number of electronic states at point (q_x, ε). The zero-bias conductance is equal to 4 G_0, because the double-degenerate band is crossing the Fermi level for each spin channel. The defect graphene has about one order smaller (0.41) transmission probability at the Fermi level. In addition, we have found that the absence of the ghost atoms decreases the conductivity by 7%. That allows us to assume that the use of ghost atoms is important for the correct description of the tunnel junction. The further increase of the numbers of ghost layers leads to an exponential decay of the transmission probability at the Fermi level with a decay length of 1.86 Å.

5.3.2 Magnetic 1D iron wire

The investigation of the transport properties of the monoatomic wire allows us, first, to verify our implementation of the NEGF method for the non-collinear magnetic systems and then opens the question of domain wall (DW) formation in nanoscale systems and the opportunity to analyze their properties. It has been shown that DWs can be quite thin due to the enhanced effective anisotropy of the constricted geometry in nanosystems [181]. In addition, it was observed experimentally that Fe nanowires which grow on W(110) [182], and Mo(110) [183] can have extremely narrow DWs with a width of several lattice constants.

The theoretical investigation was performed using the local density approximation with CA [44] parametrization for the exchange-correlation potential. The pseudo-potential and basis set are described in the Chapter 3. The schematic structure of the monoatomic iron chain is shown in Fig. 5.5. We consider 23 iron atoms, where 9 atoms are related to the scattering region and 2×7 atoms correspond to the left and right electrodes. During the calculations we use the optimized interatomic distance $d_{Fe-Fe} = 2.2$ Å.

First of all, we analyze transport through the wire with parallel magnetization direction of the electrodes. Such setup corresponds to the ground state of the wire, the band structure is shown in the left side of Fig. 5.6. Due to the linear chain symmetry, there are three sets of bands present, namely, the nondegenerate s- and d_{z^2}-dominated bands and doubly degenerate d_{xz}, d_{yz} and $d_{x^2-y^2}$, d_{xy} dominated bands. The d_{z^2}-dominated bands have a contribution from s-orbitals and they are dispersive since both d_{z^2} and s orbitals form strong σ bonds along the chain. We have a perfect agreement with PWscf calculations from Ref. [184]. Other theoretical work Ref. [81] also agrees well with our data. There is only a small difference in the position of the d_{z^2}-dominated band, which in our case is about 0.15 eV lower in energy. The reason for this are different interatomic distances in our (2.2 Å) and their (2.25 Å) calculations.

The transmission probability through the ferromagnetic Fe chain for the spin-polarized and non-collinear calculation is shown in Fig. 5.6. As it was expected, for the perfect wire, each channel has a transmission probability equal to unity and the total transmission is simply given by the number of electronic states at energy ε. If we use the non-collinear description, the total transmission T is equal to the sum of spin-up $T^{\uparrow}$ and spin-down $T^{\downarrow}$ transmissions of the spin-polarised calculations (see right panel in

Left electrode   **Scattering region**   **Right electrode**

Figure 5.5: Schematic structure diagram for the transport calculation through the monoatomic iron chain.
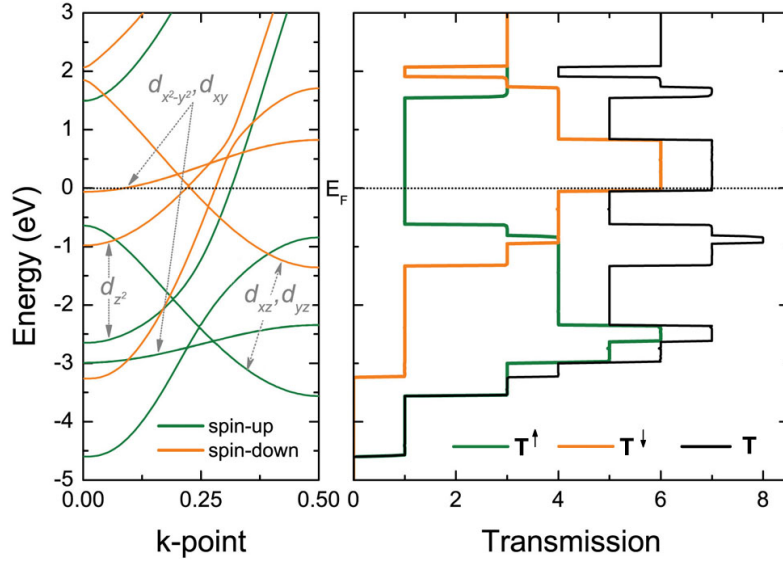
Figure 5.6: Band structure of the monoatomic iron chain and the transmission probabilities through it for the spin-polarized and non-collinear calculaions. The Fermi level is at zero energy.

Fig. 5.6). We, also, have to check that any arbitrary rotation applied for the whole system does not change the results.

Then, we investigate the influence of the domain wall width on the transport properties of the wires. We consider antiparallel magnetization of the electrodes and 1-, 3- and 5-atoms wide domain walls. The atoms which are not related to the domain wall have fixed direction of the magnetic moment via our on-site constrain method. The spin-density and the direction of the magnetic moment of the atoms related to the DW were converged self-consistently.

The different domain wall structures and the magnetization direction of the iron atom magnetic moment in the chain are shown in Fig. 5.7. In our case, the angle φ is varying along the chain (from 0° to 180°) and the Θ angle is fixed to 90°. As one can see, the domain wall is a symmetrical spin spiral with finite width. In general, the magnetization directions in the DW fulfil the rules:

$$\text{for the atom in the middle} \quad - \quad \varphi = \Phi/2$$
$$\text{for other atoms} \quad - \quad \varphi_i + \varphi_{n-i+1} = \Phi,$$

where n is a width of the DW, i is an arbitrary atom index in the first half of the DW and Φ is the magnetization direction in the right electrode (in our case $\Phi = 180°$). Note that the rule for the central atom is only correct for DW with odd number of atoms.

The DW structure can be described on the level of a Heisenberg model Eq. (3.45). We take into account only the nearest neighbor (NN) and next nearest neighbor (NNN)

interactions and assume that all other types of interactions can be neglected. In such case the model Hamiltonian is given as

$$H = J_0 - J_{NN} \sum_i \vec{e}_i \cdot \vec{e}_{i+1} - J_{NNN} \sum_i \vec{e}_i \cdot \vec{e}_{i+2}, \tag{5.72}$$

where J_{NN} and J_{NNN} are the exchange interaction parameters for NN and NNN, respectively, and i is an atomic index. In Chapter 3, we investigated the exchange interaction between Fe atoms in the infinite wire. Assuming that $J_{12} = 191.88$ meV (see Eq. (3.49) and Table 3.1) describes the NN interaction ($J_{NN} = J_{12}$) only, we found the $J_{NNN} = -79.17$ meV by using a least-squares fit.

The magnetic moment profile for 1-, 3- and 5-atom wide domain walls is shown in Fig. 5.8(a). The magnitude of the moment is smaller in the inner part of the DW then in the electrodes. The largest reduction or softening in the magnetic moment is nearly 10% for the one-atomic DW. Then, with increasing of the DW width, the softening decreases because of the reduction of the angle between the nearest-neighbor magnetic moments. The same trend was obtained by Burton *et al.* [186] for Ni monoatomic and 5×4 wires. Taking into account that the AFM phase has the largest degree of canting between neighboring moments and the value of the magnetic moment in the AFM phase is 2.86 μ_B (see Fig. 3.3(b)), we assume that the magnetic moment in the AFM phase is strongly related to the softening of the moment in the DW. Following the same idea, one can expect an enhancement of the value of the magnetic moments in the DW for the systems with larger moment in the AFM phase.

The transmission spectra of the perfect wire and the 1-, 3- and 5-atom wide domain walls are presented in Fig. 5.8(b). One can see that the transmission probability is increasing with increasing width of the DW. The reason for this is based on the fact that the canting angle between nearest Fe atoms is decreasing with increasing width
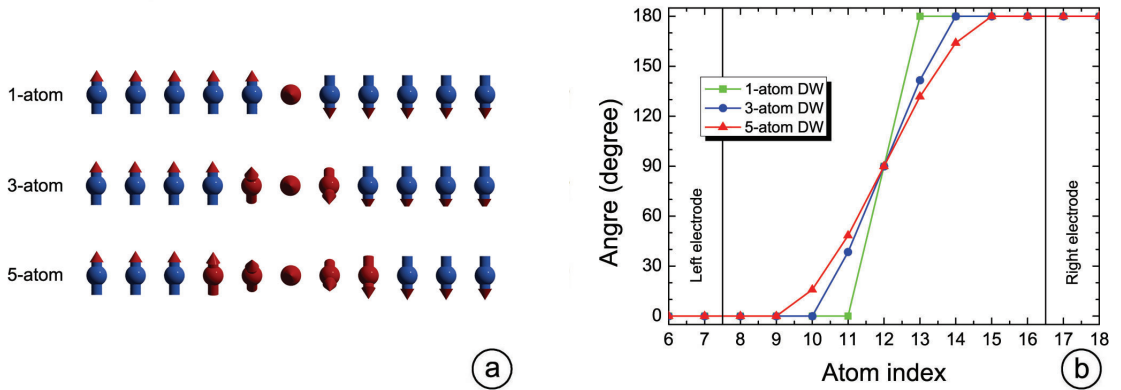
Figure 5.7: (a) Domain wall structures. Atoms related to the domain wall are indicated with red color. (b) The self-consistent magnetization direction of the iron magnetic moment in 1-, 3- and 5-atoms wide domain walls.
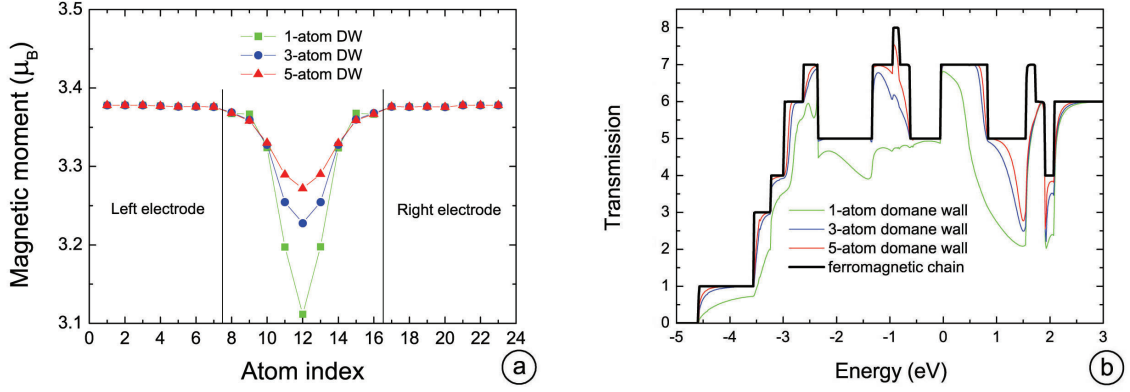
Figure 5.8: (a) - Size of the magnetic moment (in μ_B) of the iron atoms in the 1-, 3- and 5-atom wide domain walls. (b) - Energy dependence of the transmission probability for different domain wall width. The Fermi level is at zero energy.

of the DW. And therefore, the propagating wave can be transmitted through the DW with smaller losses. Here, we have the same trend as in the Ref. [185], were the tight-binding method was used for transport property calculations of a Fe-chain. It is hard to compare the absolute values, because the tight-binding model has a slightly different band structure than PWscf calculations (see Ref. [184]).

As was mentioned before, the transmission spectra can be decomposed in four spin-resolved components ($T^{\sigma\sigma'}$, where $\sigma,\sigma' = \uparrow$ or $\downarrow$) for systems with either parallel or antiparallel alignment of the lead magnetization. Using Eq. (5.71) we get the individual spin-channel transmission for the 5-atom wide DW. They are shown in Fig. 5.9. In addition, we compare each spin-channel transmission probability $T^{\sigma\sigma'}$ through the chain with a maximal transmission through it. The understanding of the maximal transmission probability stems from Fig. 5.10, where the schematic presentation of

Table 5.1: The maximal spin-resolved transmission probability through systems with different (C_L, c_L and C_R, c_R) and the same ($C=C_L=C_R$ and $c=c_L=c_R$) number of channels in the leads with antiparallel magnetization. For the meaning of C_L, c_L and C_R, c_R, see Fig. 5.10 and text.

components	different electrodes	the same electrodes
$T^{\uparrow\uparrow}$	$\min(C_L,c_R)$	$\min(C,c)$
$T^{\uparrow\downarrow}$	$\min(C_L,C_R)$	C
$T^{\downarrow\uparrow}$	$\min(c_L,c_R)$	c
$T^{\downarrow\downarrow}$	$\min(c_L,C_R)$	$\min(c,C)$
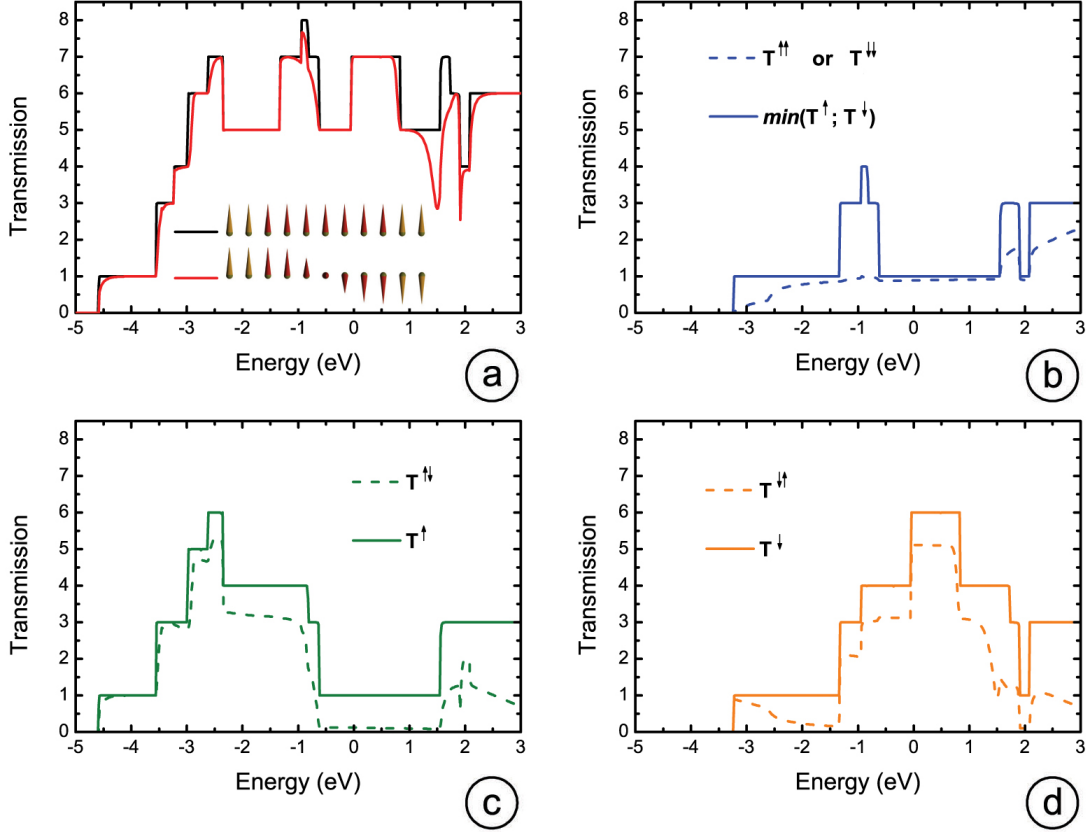
Figure 5.9: The total transmission (a) probability and its individual spin-channel components ((b) - $T^{\uparrow\uparrow}$ or $T^{\downarrow\downarrow}$, (c) - $T^{\uparrow\downarrow}$ and (d) - $T^{\downarrow\uparrow}$) for the iron wire with a 5-atom wide domain wall in comparison with maximal transmission through them. See details in the text.

the scattering processes in the magnetic system with parallel (Fig. 5.10(a)) and antiparallel (Fig. 5.10(b)) magnetization in the electrodes is shown. Note we consider a general case, where the system could have a different number of channels for the left (L) and the right (R) lead, each of which can be decomposed in two spin-channels, namely $C_{L/R}$ for spin-up and $c_{L/R}$ for spin-down. The spin-directions correspond to the global coordinate system are related to the left electrode (see Fig. 5.10). Here, we have to remember that the number of channels is generally energy dependent.

It is known that the maximal spin-up/spin-down transmission for the spin-polarized system with different electrodes and parallel magnetization is a minimum value over C_L/c_L and C_R/c_R. Now, following the same idea, we assert that the maximal value of the spin-resolved transmission probability $T^{\sigma\sigma'}$ is the minimum over the number of channels in the left lead, with spin-direction σ, and in the right lead, with spin-direction σ'. We combine the maximal spin-resolved transmission probabilities for systems with different and the same number of channels and antiparallelly magnetized electrodes in Table 5.1.
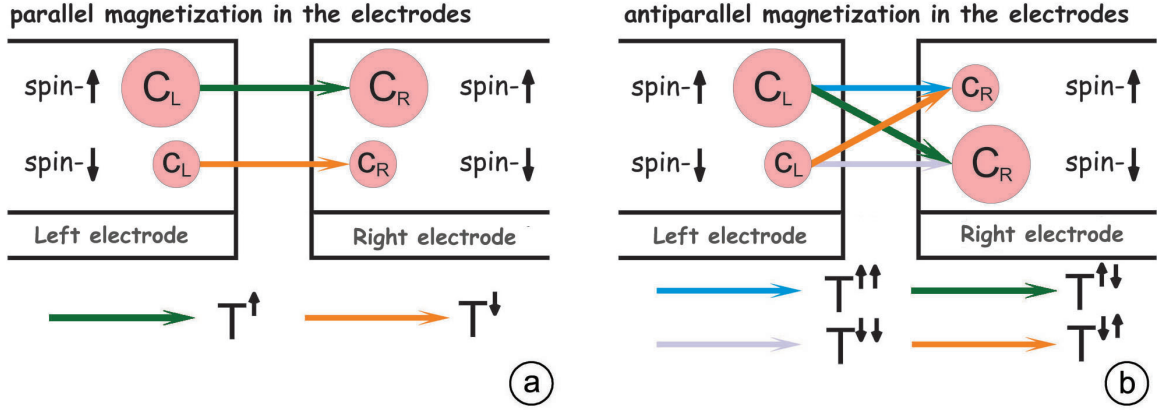
Figure 5.10: The schematic presentation of the electron scattering in the magnetic system with parallel (a) and antiparallel (b) magnetization in the electrodes. The system with parallel alignment of the lead magnetization is spin-polarized. See details in the text.

Now, we can return to the analysis of the spin-polarized transport through the Fe chain. One can see that the direct components of the transmission $T^{\uparrow\uparrow}$ and $T^{\downarrow\downarrow}$ [Fig. 5.9(a)] are identical. They are very close to the maximal transmission probability which is equal to $\min(T^{\uparrow}, T^{\downarrow})$, where $T^{\uparrow}/T^{\downarrow}$ is the spin-up/spin-down transmission for the ferromagnetic chain (see Fig. 5.6). The main contribution to $T^{\uparrow\uparrow}$ or $T^{\downarrow\downarrow}$ stems from the channel related to the s- and d_{z^2}-orbitals. In the ferromagnetic Fe wire, these orbitals create the d_{z^2}-dominant bands which give the smallest contribution ($\sim$10 %) to the total magnetic moments of the Fe atoms. Therefore, the electron with s/d_{z^2}-symmetry can be transmitted through the DW without scattering or with small scattering.

As illustrated in Fig. 5.10, the spin-flip transmission $T^{\uparrow\downarrow}$ (or $T^{\downarrow\uparrow}$) gives the probability of spin-up (or spin-down) electrons coming from the left electrode and being transmitted to the right electrode with opposite spin direction. In our case, the electrons with d_{xz}-, d_{yz}- and $d_{x^2-y^2}$-, d_{xy}-symmetries are dominating in both $T^{\uparrow\downarrow}$ and $T^{\downarrow\uparrow}$. The maximal transmission probability for these transmissions are $T^{\uparrow}$ and $T^{\downarrow}$, respectively. At this stage it is reasonable to make some remarks. First of all, the standard approach of Eqs. (5.69)-(5.71) for the investigation of the individual spin-channel components of the transmission probability can be applied only for non-collinear system with either parallel or antiparallel magnetization in the leads. Moreover, the magnetization in the electrodes must be directed along the z axis. Then, we always have to choose the spin-quantization axis which is common for both electrodes and must be coupled to one of them. Taking into account that the choice of this electrode is arbitrary, one can have problems with the data interpretation or with comparison.

In order to omit these problems, we suggest a new procedure to obtain the components of the transmission spectra for non-collinear systems with arbitrarily magnetized electrodes. Note that the $\vec{q}$-index is dropped for matter of simplicity. First, the system must satisfy two conditions:

1) the leads have to be materials with well defined spin-quantization axes via two polar angles (Θ_L, φ_L) for the left electrode and (Θ_R, φ_R) for the right one;

2) the central region of the scattering setup (Fig. 5.2) has to include a sufficient number of surface layers with the same spin-quantization axes as the electrodes.

Now, we can assume that there is a unitary transformation with matrix $\hat{\mathbf{U}}_{L/R}$ which can diagonalize the $\hat{\boldsymbol{\Gamma}}_{L/R}$ in spin-space:

$$\hat{\boldsymbol{\Gamma}}_L = \hat{\mathbf{U}}_L^\dagger \hat{\boldsymbol{\Gamma}}_L^d \hat{\mathbf{U}}_L = \hat{\mathbf{U}}_L^\dagger \begin{bmatrix} \boldsymbol{\Gamma}_L^\uparrow & 0 \\ 0 & \boldsymbol{\Gamma}_L^\downarrow \end{bmatrix} \hat{\mathbf{U}}_L; \tag{5.73}$$

$$\hat{\boldsymbol{\Gamma}}_R = \hat{\mathbf{U}}_R^\dagger \hat{\boldsymbol{\Gamma}}_R^d \hat{\mathbf{U}}_R = \hat{\mathbf{U}}_R^\dagger \begin{bmatrix} \boldsymbol{\Gamma}_R^\uparrow & 0 \\ 0 & \boldsymbol{\Gamma}_R^\downarrow \end{bmatrix} \hat{\mathbf{U}}_R. \tag{5.74}$$

If $\hat{\mathbf{U}}_{L/R}$ is a spin-$\frac{1}{2}$ rotation matrix for the left/right electrode so that $\hat{\mathbf{U}}_{L/R} = \hat{\mathbf{U}}(\Theta_{L/R}, \varphi_{L/R})$, then $\boldsymbol{\Gamma}_{L/R}^\uparrow$ and $\boldsymbol{\Gamma}_{L/R}^\downarrow$ are spin-up and spin-down components, respectively, in the local coordinate system of the left/right electrode defined with $\Theta_{L/R}, \varphi_{L/R}$ angles.

The proof of our assumption is as follows (for matter of simplicity the L and R indices were dropped):

$$\hat{\boldsymbol{\Gamma}}^d = \hat{\mathbf{U}} \hat{\boldsymbol{\Gamma}} \hat{\mathbf{U}}^\dagger \xrightarrow{Eq.(5.46)} i \left[\hat{\mathbf{U}} \hat{\boldsymbol{\Sigma}} \hat{\mathbf{U}}^\dagger - \left(\hat{\mathbf{U}} \hat{\boldsymbol{\Sigma}} \hat{\mathbf{U}}^\dagger \right)^\dagger \right], \tag{5.75}$$

$$\hat{\mathbf{U}} \hat{\boldsymbol{\Sigma}}(z) \hat{\mathbf{U}}^\dagger \xrightarrow{Eq.(5.31)} \hat{\mathbf{U}} \left(z\hat{\mathbf{S}} - \hat{\mathbf{V}} \right)^\dagger \hat{\mathbf{g}}(z) \left(z\hat{\mathbf{S}} - \hat{\mathbf{V}} \right) \hat{\mathbf{U}}^\dagger$$

$$= \left(z\hat{\mathbf{S}} - \hat{\mathbf{U}} \hat{\mathbf{V}} \hat{\mathbf{U}}^\dagger \right)^\dagger \hat{\mathbf{U}} \hat{\mathbf{g}}(z) \hat{\mathbf{U}}^\dagger \left(z\hat{\mathbf{S}} - \hat{\mathbf{U}} \hat{\mathbf{V}} \hat{\mathbf{U}}^\dagger \right), \tag{5.76}$$

here we use the fact that the overlap matrix $\hat{\mathbf{S}}$ is diagonal in spin-space (see Eq. (3.28)). Now, using the first of the above two conditions and taking into account that $\hat{\mathbf{U}}$ is a spin-$\frac{1}{2}$ rotation matrix, we can write for the unperturbed Green's function of the semi-infinite electrode:

$$\hat{\mathbf{U}} \hat{\mathbf{g}}(z) \hat{\mathbf{U}}^\dagger \xrightarrow{Eq.(5.33)} \left(z\hat{\mathbf{S}} - \hat{\mathbf{U}} \hat{\mathbf{H}} \hat{\mathbf{U}}^\dagger \right) \xrightarrow{\hat{\mathbf{U}} = \hat{\mathbf{U}}(\Theta, \varphi)} \left(z\hat{\mathbf{S}} - \hat{\mathbf{H}}^d \right) = \hat{\mathbf{g}}^d(z), \tag{5.77}$$

where the index d means diagonal in spin-space.

Our second condition allows to diagonalize the overlap matrix $\hat{\mathbf{V}}$

$$\hat{\mathbf{U}} \hat{\mathbf{V}} \hat{\mathbf{U}}^\dagger \xrightarrow{\hat{\mathbf{U}} = \hat{\mathbf{U}}(\Theta, \varphi)} \hat{\mathbf{V}}^d. \tag{5.78}$$

Finally, the multiplication of the spin-diagonal matrices, see Eqs. (5.75) and (5.76), gives the spin-diagonal matrix $\hat{\boldsymbol{\Gamma}}^d$.

Now, taking into account that we can define the spin-up and spin-down components of $\hat{\boldsymbol{\Gamma}}_L$ and $\hat{\boldsymbol{\Gamma}}_R$, the individual spin-resolved component of the transmission is given by:

$$T^{\sigma\sigma'}(\varepsilon) = \mathrm{Tr} \left[(\hat{\boldsymbol{\Gamma}}_L^\sigma(\varepsilon) \hat{\mathbf{G}}_C(\varepsilon)^\dagger \hat{\boldsymbol{\Gamma}}_R^{\sigma'}(\varepsilon) \hat{\mathbf{G}}_C(\varepsilon) \right], \tag{5.79}$$

where the spin indices σ and σ' define the spin components ($\uparrow$, $\downarrow$) in the local coordinate system of each electrode and

$$\hat{\mathbf{\Gamma}}^{\uparrow}_{L/R} = \hat{\mathbf{U}}^{\dagger}(\Theta_{L/R}, \varphi_{L/R}) \begin{bmatrix} \mathbf{\Gamma}^{\uparrow}_{L/R} & 0 \\ 0 & 0 \end{bmatrix} \hat{\mathbf{U}}(\Theta_{L/R}, \varphi_{L/R}); \tag{5.80}$$

$$\hat{\mathbf{\Gamma}}^{\downarrow}_{L/R} = \hat{\mathbf{U}}^{\dagger}(\Theta_{L/R}, \varphi_{L/R}) \begin{bmatrix} 0 & 0 \\ 0 & \mathbf{\Gamma}^{\downarrow}_{L/R} \end{bmatrix} \hat{\mathbf{U}}(\Theta_{L/R}, \varphi_{L/R}). \tag{5.81}$$

In some cases, it is difficult to include a large number of surface layers in the central part of the scattering region. Therefore, the V_L or V_R matrices are not diagonal in the local coordinate system of each electrode. And, in turn, we can not get the spin-up and spin-down components of $\hat{\mathbf{\Gamma}}$ for the left and right leads. Nevertheless, we still can use the equations (5.79), (5.80) and (5.81) for $T^{\sigma\sigma'}$ calculations and then estimate the error

$$\Delta = T - \left(T^{\uparrow\uparrow} + T^{\uparrow\downarrow} + T^{\downarrow\uparrow} + T^{\downarrow\downarrow} \right), \tag{5.82}$$

where T is the total transmission. If Δ is much less then any of the components at the Fermi energy or in the bias window, we assume that it is not necessary to enlarge the scattering region.

In addition, our procedure allows to calculate the spin-current components for non-collinear systems with arbitrary magnetized electrodes. Using Eqs. (5.66) and (5.79), the up and down components of the current flowing from the left electrode to the right in the local coordinate system of the right electrode can be given by

$$I^{\sigma'}_{LR} = \frac{e}{h} \int_{-\infty}^{\infty} d\varepsilon \left[\sum_{\sigma} T^{\sigma\sigma'} \right] (f(\varepsilon - \mu_L) - f(\varepsilon - \mu_R)), \quad \text{where} \quad \sigma' = \uparrow, \downarrow . \tag{5.83}$$

Then, following the ideas of P. Levy and A. Fert [187, 188], we can construct the spin current matrix in the global coordinate system

$$\hat{\mathbf{I}}_{LR} = \frac{1}{2} \begin{bmatrix} I^{\uparrow\uparrow}_{LR} & I^{\uparrow\downarrow}_{LR} \\ I^{\downarrow\uparrow}_{LR} & I^{\downarrow\downarrow}_{LR} \end{bmatrix} = \hat{\mathbf{U}}^{\dagger}(\Theta_R, \varphi_R) \frac{1}{2} \begin{bmatrix} I^{\uparrow}_{LR} & 0 \\ 0 & I^{\downarrow}_{LR} \end{bmatrix} \hat{\mathbf{U}}(\Theta_R, \varphi_R), \tag{5.84}$$

which, in analogy to the spin-density matrix, see Eq. (3.19), can be characterized via the charge current (I^c_{LR}) and the components of the spin current (I^x_{LR}, I^y_{LR} and I^z_{LR})

$$I^c_{LR} = \frac{1}{2} \text{Tr} \left(\hat{\mathbf{I}}_{LR} \right); \qquad I^i_{LR} = \frac{1}{2} \text{Tr} \left(\hat{\sigma}_i \hat{\mathbf{I}}_{LR} \right), \quad i = x, y, z; \tag{5.85}$$

$$\hat{\mathbf{I}}_{LR} = \frac{1}{2} \begin{bmatrix} I^c_{LR} + I^z_{LR} & I^x_{LR} - iI^y_{LR} \\ I^x_{LR} + iI^y_{LR} & I^c_{LR} - I^z_{LR} \end{bmatrix}, \tag{5.86}$$

where ($\hat{\sigma}_i$, $i = x, y, z$) are the Pauli spin matrices.

6 Electronic transport through organometallic V_nBz_{n+1} wires

The investigation of the electronic transport through devices with small amount of atoms is becoming one of the most fascinating branches of modern solid state physics. The transport through organometallic molecules already shows new phenomena like single-molecule switching [18]. Here we continue the work in direction of molecular spintronics and suggest a molecular spin filter based on VBz wires.

In this chapter, we combine our theoretical development and knowledge about VBz sandwich structures in order to investigate their electronic transport properties. The V_nBz_{n+1}, $n = 1, ..., 4$ molecules are placed between Co(100) electrodes with face centered cubic (fcc) symmetry. We consider electrodes with both parallel and antiparallel magnetic configurations. Our simulations are performed on the level of GGA with Perdew-Burke-Ernzerhof [52] parametrization for electron exchange and correlation. We have found that a TZP basis set for vanadium and DZP basis set for Co, C and H gives reasonable results, which are in good agreement with our all electron calculations based on the CRYSTAL [77] code. For the calculation of the transport properties, we use 28 energy points for the complex contour integration and 25 points for the bias window. We have to mention that the increase of the number of energy points does not affect the electronic and transport properties of the Co-VBz-Co systems.

The schematic structure of the V_nBz_{n+1} wires suspended between Co electrodes is shown in Fig. 6.1. The VBz molecules are attached at the hollow site position of the surface, and two C-H bonds oriented along (100) direction. The aromatic rings remain parallel to the surface. Then, we have found a small buckling of the surface of about 0.04 Å for all wires. After adsorption, the structure of the benzene next to the electrodes is deformed, while the structure of the second benzene ring remains unchanged. Here we have to note that all benzene rings of the V_nBz_{n+1}, $n = 1, ..., 4$ wires next to the surface change their structure in the same way. There are two inequivalent positions for the carbon atoms in the first benzene: four C atoms are close to the substrate atoms at distance of 1.72 Å; the remaining two are located over the bridge positions 0.2 Å lower than the four carbon atoms. The hydrogen atoms have the same trend as the carbons, only that they are shifted about 0.2 Å away form the surface in direction of vanadium. Because of the adsorption, the first aromatic ring is expanded. Namely, two carbon bonds parallel to the substrate rows are stretched to about 1.51 Å and the other four bonds are stretched to about 1.56 Å. In general, the adsorbed VBz molecules on Co(100) have a similar structure as the adsorbed benzene on the Ni(100) surface [189].
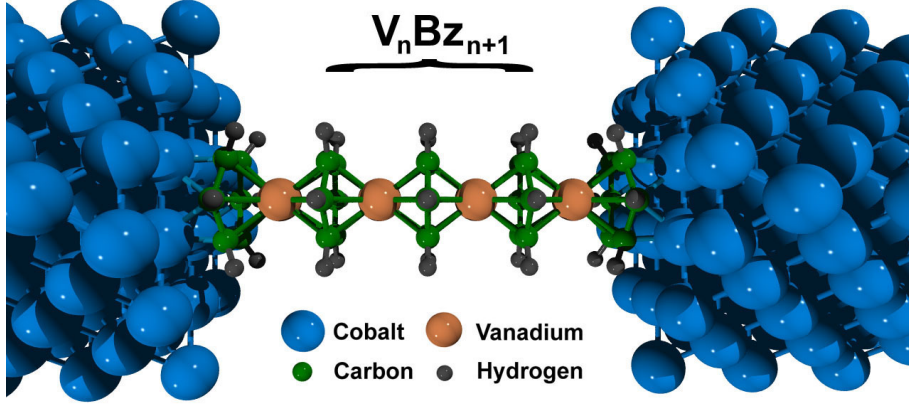
Figure 6.1: Schematic structure of the V_nBz_{n+1} wires suspended between Co(001) electrodes.

6.1 Electrodes with parallel magnetic configuration

The calculated transmission spectra for both spin-channels of the V_nBz_{n+1} wires with $n = 1, ..., 4$ are presented in Fig. 6.2. Here we consider the electrodes with parallel magnetization. In Table 6.1 we show the spin polarized conductance and its spin polarization at the Fermi energy. The spin polarization of the conductance (SPC) is defined as

$$\text{SPC} = \frac{|G_{up} - G_{down}|}{G_{up} + G_{down}}, \tag{6.1}$$

where G_{up} and G_{down} are conductances for the spin-up and the spin-down channel, respectively.

One can see that the VBz chains with $n = 3, 4$ show strong spin-polarization at the Fermi energy, which is about 80% for both wires. Therefore, we can expect that these wires will work as highly effective spin filters under applied bias. The shorter chains show smaller spin-polarization. The large transmission probabilities and spin-polarization of 50% for the VBz_2 molecule can be explained by the large spin-polarized

Table 6.1: Zero bias spin-polarized conductance (in G_0) and spin-polarization of the conductance of the V_nBz_{n+1} wires.

	n=1	n=2	n=3	n=4
G_{up}	0.67	0.12	0.07	0.07
G_{down}	0.27	0.17	0.62	0.76
G_{tot}	0.94	0.29	0.69	0.83
SPC(%)	42.6	17.2	79.7	83.1
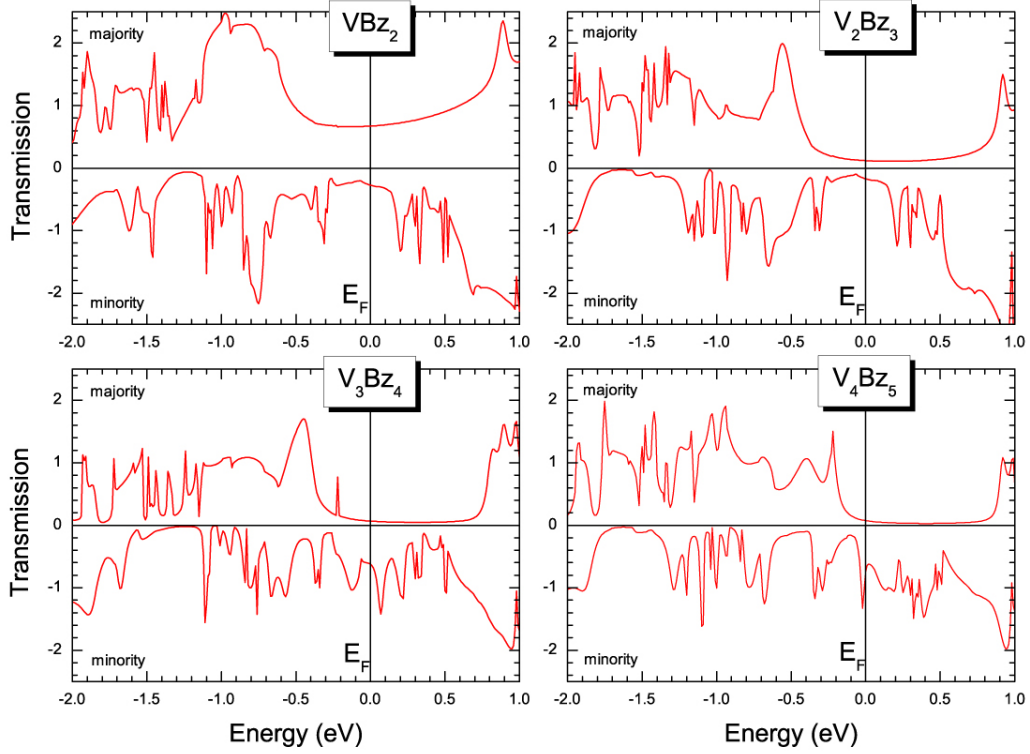
Figure 6.2: Transmission spectra of the V_nBz_{n+1}, $n = 1, ..., 4$ molecules suspended between Co electrodes.

tunneling from one electrode to another. This agrees with the fact that, if we increase the number of VBz units by one, the transmission decreases for both spin-channels (see Table 6.1). The difference between the transmission probabilities of the first two ($n = 1, 2$) and the second two ($n = 3, 4$) molecules can be explained with the strong influence of the electrodes on the VBz units next to the surface. The analysis of the vanadium magnetic moments confirms this explanation and shows their increase at both ends of the wire (2.3 μ_B for VBz_2, 1.8 μ_B for V_2Bz_3 and about 1.7 μ_B for V_3Bz_4 and V_4Bz_5) with respect to the moments of the free standing molecules (about 1.2 μ_B). The magnetic moments of the vanadium atoms in the central part of the chains (for $n = 3, 4$) are decreasing with increasing number of VBz units, which is clear since they have a smaller interaction with the electrodes. The analysis of the spin- and space-resolved local density of states calculated around the Fermi level (± 0.05 eV) for the four molecules also confirms the strong influence of the electrodes on the VBz units next to the surface. In Fig. 6.3, one can see a strong reconfiguration of the local density around the VBz in the electrode regions in comparison to the density in the middle of the V_4Bz_5 molecule which is nearly the same as the density of the molecule in the vacuum.

In order to understand the influence of the half-metallic character on the transport properties, we performed a transmission eigenchannel analysis [20, 190] for the V_4Bz_5
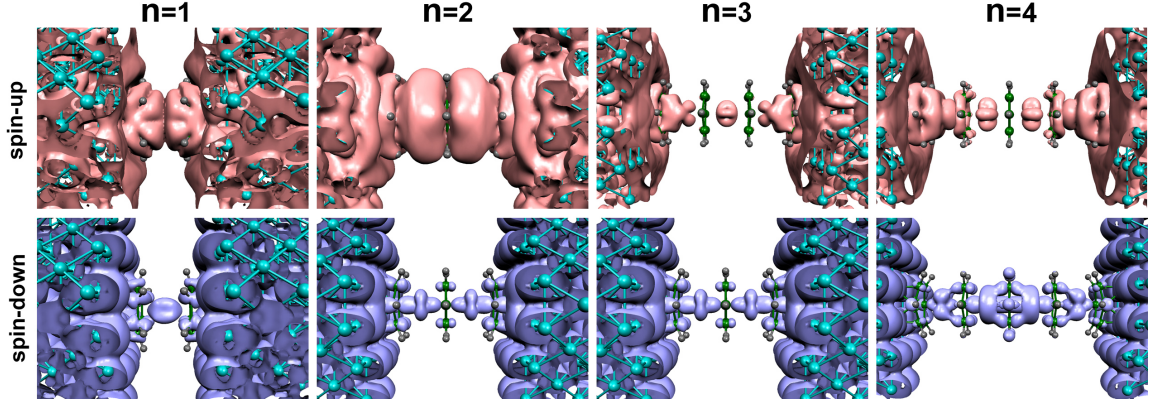
Figure 6.3: The spin- and space-resolved local density of states calculated around the Fermi level (± 0.05 eV) for the V_nBz_{n+1}, $n = 1, ..., 4$ molecules suspended between Co electrodes. The isodensity surfaces are defined by the values of $0.0005/0.005$ e/Bohr^3 for majority/minority spins.

molecule. In Fig. 6.4 we present the eigenchannels of the transmission and their three scattering states with highest transmittion probability at the Fermi level for each of the two spin components. The corresponding transmission eigenvalues are $T^{up}_{d_{x^2-y^2}}=0.06$, $T^{up}_{d_{xy}}=0.02$, $T^{up}_{d_{xz}}=10^{-5}$ and $T^{down}_{d_{z^2-r}}=0.35$, $T^{down}_{d_{x^2-y^2}}=0.40$, $T^{down}_{d_{xy}}=0.01$ for the majority and minority spin components, respectively. One can see that all majority-spin wave functions have a decaying behavior through the cluster. The decaying behavior is also observed for the minority-spin scattering states with d_{xy} symmetry. We have to note that the $d_{x^2-y^2}$ and d_{xy} vanadium states correspond to the same symmetry group E_2
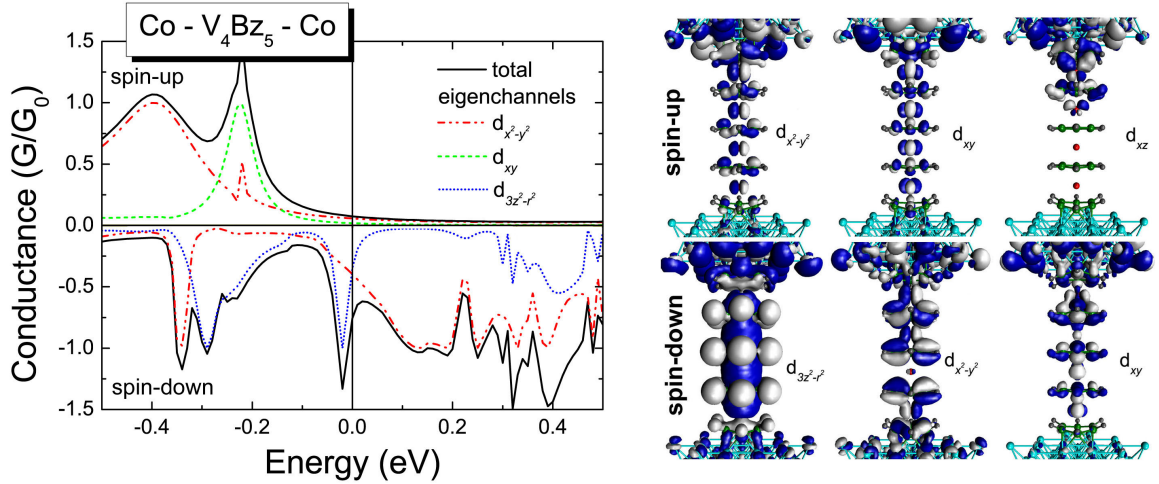
Figure 6.4: (Left side) The transmission eigenchannels of the V_4Bz_5 wire. (Right side) The real part of the scattering states of the Co-V_4Bz_5-Co system for the three high-conducting channels at the Fermi energy.
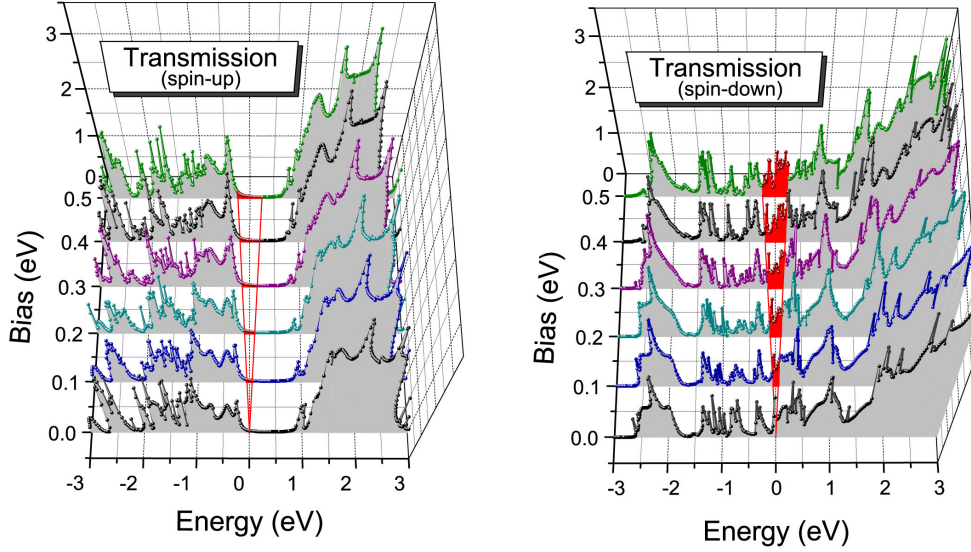
Figure 6.5: The bias dependence of the transmission probability for both spin-channels of the V$_4$Bz$_5$ wire suspended between Co electrodes. The part of the transmission related to the bias window is marked with red. Left side - spin-up channel, right side - spin-down channel.
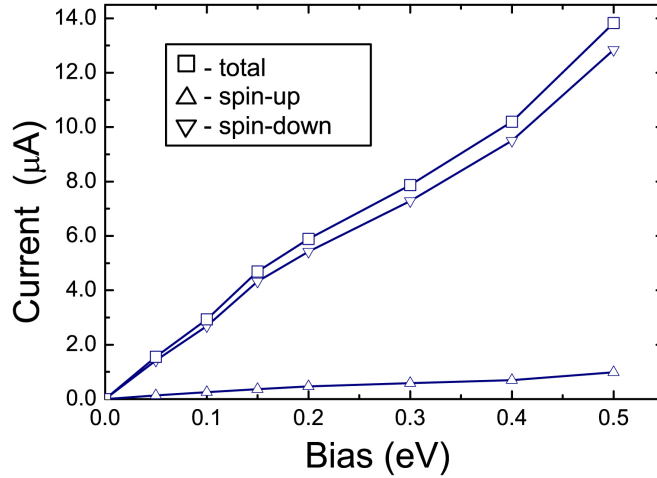
Figure 6.6: The current-voltage characteristics through the V$_4$Bz$_5$ molecule .

in the infinite VBz wire (see Ref. [20] and Chapter 4). After the adsorption of the VBz molecules on the Co(100) surfaces, these states become nonequivalent and related to different symmetry groups. Finally, the transmission eigenchannel analysis shows that the scattering states with d_{z^2-r} and $d_{x^2-y^2}$ character have the highest contribution to the transmission and are responsible for the strong spin-polarization at the Fermi energy.

In Fig. 6.5 we show the calculated spin-polarized transmission spectra of the V_4Bz_5 molecule as functions of electron energy and bias voltage. The related I-V curve is presented in Fig. 6.6. We observe a linear current-voltage characteristics and the conservation of the high spin-polarization of the current for the whole voltage region. The evolution of the transmission probability with the bias shows that resonant peaks closely follow the chemical potentials of either left or right leads. The reason for this becomes clear from the analysis of the non-equilibrium density. Because of the symmetry of the V_4Bz_5 molecule, each electronic state is dominating in the left (ρ_L) or in the right (ρ_R) non-equilibrium densities. Therefore, if the bias is applied, these states are moved together with the corresponding chemical potential what also leads to the shift of the resonant peaks in the transmission spectra. Thus, following this idea, we can assume that the high spin-polarization of the current will be conserved while the bias window is smaller then the majority band gap (~ 1 eV).

6.2 Electrodes with antiparallel magnetic configuration

In order to investigate the electronic transport through the VBz wire suspended between the Co(100) leads with antiparallel magnetic configuration, we consider three types of domain walls (DWs): two symmetric and asymmetric collinear abrupt DWs and one non-collinear DW. The calculations were performed for the V_4Bz_5 molecule,
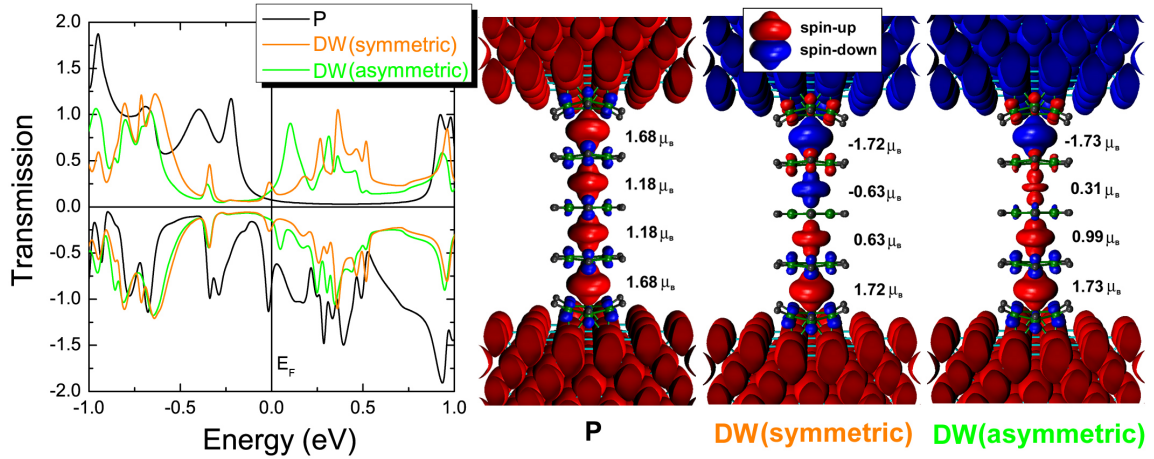
Figure 6.7: Left side: The transmission spectra of the V_4Bz_5 with symmetric and asymmetric collinear abrupt DWs in comparison to the transmission through the wire coupled to the leads with parallel magnetic configuration (P). Right side: The isosurface of the spin-density for three different magnetic configuration in the V_4Bz_5 molecule. The isodensity value is 0.003 e/Bohr^3. The numbers correspond to the magnitude of the magnetic moments at the vanadium atoms.
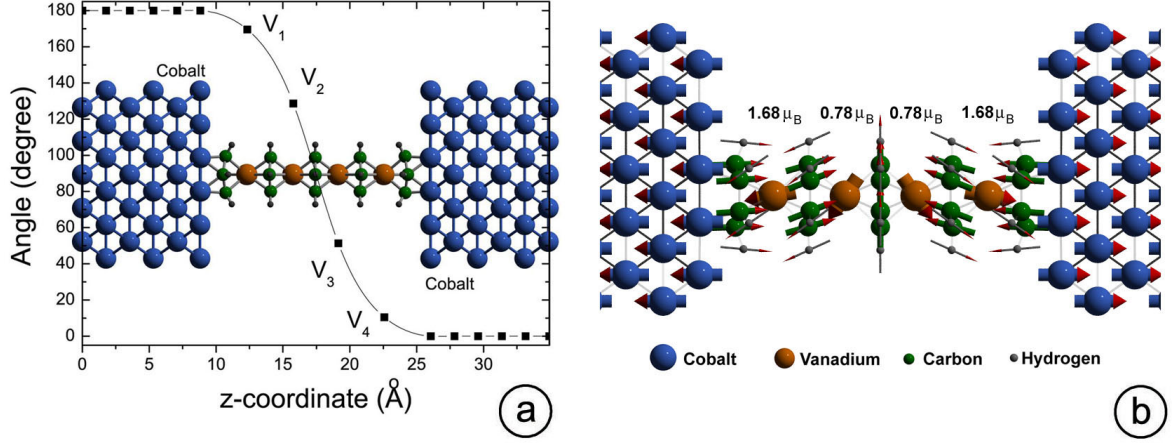
Figure 6.8: (a) The magnetization direction of the magnetic moments of V in the V_4Bz_5 molecule coupled to the electrodes with antiparallel magnetization. (b) The non-collinear domain wall structure in the V_4Bz_5 wire. The numbers correspond to the magnitude of the magnetic moments of vanadium.

which shows the strongest spin-polarization of the conductance at zero bias for the electrodes with parallel magnetization.

In the left side of Fig. 6.7 the transmission spectra of V_4Bz_5 with two collinear abrupt DWs are shown. We compare these transmissions with the spectra related to the wire without DW (electrodes with parallel magnetization). First of all, we observe that the half-metallic behavior in the transmission is destroyed. The 'optimistic' magneto-resistance ratio is 152% for the symmetric DW and 80% for asymmetric one. The symmetric DW shows total absence of spin polarization and identical transmissions $T_{up} = T_{down}$=0.23 for both spin channels, while the asymmetric DW has a spin-polarization of 11% with T_{up}=0.18 and T_{down}=0.15. The magnetic moments at the V atoms in the middle of the DW are decreased (see right side of Fig. 6.7). For the symmetric DW they become very close to the values of the infinite VBz wire with antiferromagnetic ordering ($0.62\mu_B$). The asymmetric DW shows the influence of the electrodes much stronger. For the vanadium next to the electrodes the magnitude of the magnetic moment remains, while for the second vanadium the value of the moment drastically decreases to 0.31 μ_B. The spin-density redistribution is reflected on the transmission spectra where the resonant peaks are shifted above the Fermi energy. From energetic point of view the asymmetric DW is more preferable than the symmetric one. The energy difference between these two magnetic configurations is 0.15 eV.

The non-collinear DW in the VBz chain was investigated by using our on-site constraint method and our generalization of the NEGF method for the non-collinear systems. The magnetization in the left lead was turned by 180° and the local magnetization along the wire rotates between the lead magnetizations in constant steps of $180°/(N + 1)$, where N is the number of vanadium atoms. We fix the magnetization direction in the

bulk part of the system. All other moments were free with respect to the variation of the direction of the magnetic moment during the self-consistent procedure.

The final structure of the domain wall is shown in Fig. 6.8. For the angular dependence we obtain similar behavior as for the monoatomic Fe chain (see Chapter 5). The vanadium magnetization directions in the DW confirm the rules:

$$\Theta_1 + \Theta_4 = 180°$$
$$\Theta_2 + \Theta_3 = 180°,$$

where Θ_i, $i = 1, 2, 3, 4$ are the polar angles responsible for the direction of the magnetic moment of the V atoms. The total induced moment on the benzene rings is negative with the main contribution from the carbon subsystem. In general, the direction of the induced magnetic moment on the C and H is close to the average of the moment directions of the nearest vanadium atoms. The magnitude of the V magnetic moments in the middle of the non-collinear DW is about $0.15\mu_B$ larger then for symmetric configuration of the abrupt DW. As was shown in the in Chapter 5 and in Ref. [186], this increase of the magnetic moments is a result of their softening with an increase of the width of the DW.

The transmission probability for the non-collinear DW is 0.58. This value is about two times large then for collinear DWs. Therefore, the 'optimistic' magnetoresistance ratio is decreased to 33%. The increase of the transmission and decrease of the magneto-resistance was also observed in Ref. [31], where the Ni, Co, and Fe nanowires were investigated.

7 Conclusions

The LCAO method is one of the most precise computational schemes regularly applied in biology, chemistry and physics. It is applicable to all elements of the periodic table and to molecules and solids with low symmetry, structural and chemical complexity. In this thesis we have suggested an extension of the LCAO method for non-collinear magnetic systems by introducing the novel on-site constraint approach which allows to fix the direction of the magnetic moments on any atom and to investigate not only the ground state of the non-collinear systems but also their spin excitations. Furthermore, we have presented a generalization of the NEGF method for non-collinear systems with translational invariance based on the LCAO method which gives the opportunity to investigate the non-equilibrium transport in non-collinear systems. Finally, our ideas were implemented in the DFT based SIESTA and TranSIESTA codes and were applied for the investigation of the electronic, magnetic and transport properties of realistic magnetic molecules and wires. Within our investigations, priority was given to organometallic molecules and wires.

The possibility to fix the direction of the magnetic moment at any atom opens a new way to investigate non-collinear systems, like complex magnetic molecules, domain walls, magnetic surfaces etc. In combination with theory of spin-dynamics, it also allows to analyze time-dependent processes. The problem to fix the direction of the magnetic moment in the LCAO method is strongly related to the definition of the atom. In our case we are not analyzing the atomic volume, but we manipulate with the density matrix which defines the charge and magnetization for any species. Since some elements of the density matrix are only related to one site, we can average the direction of the magnetic moment and fix it for these elements, assuming that the magnetization is the same for all orbitals related to the same atom. Because of the site-dependent nature of the constraint, we call our procedure "on-site constraint method". In addition, our method allows to drastically accelerate the self-consistent field procedure by defining different convergence criteria for the density matrix elements in the local coordinate system and for the polar angles (Θ_μ, φ_μ, where μ is atomic index) related to the magnetization of the atoms.

The accuracy, precision and correctness of the code was validated by the Mn and Fe monoatomic wires and the Mn_3 molecular cluster. We have shown that the systems are invariant with respect to rotations in spin space. Excellent agreement was obtained between our results and all electron calculations with the CRYSTAL code for spin-polarized solutions. We have also investigated the ferromagnetic-antiferromagnetic transition in the wires and the Mn_3 molecule by varying the direction of the magnetic moment on the atoms. We map the orientational energy dependence to the effective

spin-Hamiltonians and show that the four-spin interaction terms have to be taken into account in order to have a precise description of realistic magnetic systems.

The second theoretical part of the thesis is related to the simulation of the electronic, magnetic and transport properties of non-collinear systems with translation invariance in non-equilibrium. For this, we have restated and generalized the NEGF method. We have derived the equations for the equilibrium and non-equilibrium parts of the density matrix and for the current and transmission. In addition, we have suggested the straightforward procedure for the calculation of the four spin-resolved components of the transmission for the system with arbitrary magnetization in the electrodes. Following the ideas of P. Levy and A. Fert, we have introduced the spin-current matrix.

The verification of the implementation was performed for the perfect and defect graphene sheet and monoatomic Fe wire. We have shown that the transmission spectra of the perfect graphene reproduce the q-resolved band structure and the defected graphene has about one order smaller transmission probability at the Fermi level than the ideal one. With the monoatomic iron wire we have analyzed the narrow domain wall (DW) formation. We have calculated the self-consistent domain wall structures for 1-, 3- and 5-atoms wide domain walls. We have found that the largest reduction in the magnetic moment is for the one-atomic DW, and it decreases with the increase of its width. We have also shown that the transmission probability is increasing with the increasing width of the DW. The reason for this is based on the fact that the canting angle between nearest Fe atoms is decreasing. Therefore, the propagating wave can be transmitted through the DW with smaller losses.

Next, we presented a detailed picture of the electronic and magnetic properties of the metallophthalocyanines (MetPc, Met=Co,Cu) and multidecker metal-benzene (MetBz, Met=Sc-Co, Bz=C_6H_6) half-sandwiches, sandwiches and wires. The CoPc and CuPc molecules correspond to the doublet electronic ground state with magnetic moments 1.15 μ_B on Co and 0.58 μ_B on Cu. Our results show that the interaction between two MetPc molecules is rather weak. We also have shown that the electronic structures of the molecules and molecular wires are very similar. Our density of states of the CuPc and CoPc molecules are in very good agreement with experimentally obtained electronic valence band structures. This agreement allowed to resolve the nature of the main features observed in the experimental spectra. Also, we have performed a systematic analysis of the electronic structure of CuPc-polymorphs and have suggested a new CuPc-phase.

Then, we have analyzed the stability of the half-sandwich MetBz and the sandwich MetBz$_2$ structures. High concentration of the MetBz magnetic states in small intervals of Met-Bz distances was obtained. In the case of MetBz$_2$ molecules, the magnetic configuration in the ground state have the smallest multiplicity. The displacement of the second aromatic ring out of the symmetry axis shows that the complexes with late-transition metals (Met=Fe,Co,Ni) prefer a tilted sandwich structure, in which the transition metal atom is situating below the C-C bond of the benzene. Then, we have found that the rotation of the benzene around high symmetry axis costs a little energy (less then 50 meV for all complexes), while the rotation of the ring around the metal

atom needs more energy (about 30 meV per each 6 degree for Met=Sc-Mn), but it is still small in comparison to the Bz displacement. Therefore, we have assumed that the rotational degree of freedom is responsible for the limitation of the length of the Met_nBz_{n+1} multi-decker sandwich structures. Practically all magnetic phases can be realized in the early-transition metal benzene wires. We reveal that the organometallic VBz wire is half-metalic. We have found that the electronic structure is robust against details of the calculations. Moreover, the unusual electronic properties of the infinite 1D wire remain in the V_nBz_{n+1} molecules of finite length. We also have found that the LDA- and GGA-based half-metallic electronic structure of the infinite MnBz wire is an artifact related to the deficiencies in the description of localized highly correlated electronic states.

In the end of the work, we combine all our previous theoretical development and knowledge about vanadium-benzene multidecker structures. We have studied the electronic transport properties of the V_nBz_{n+1} chains suspended between Co(001). We have shown that these systems with $n \geq 3$ can work as highly effective spin filters under applied bias. The analysis of the local density of states of the Co-V_nBz_{n+1}-Co systems around the Fermi level shows the strong influence of the electrodes on the nearest VBz units of the chains. According to the transmission eigenchannel analysis, the eigenchannels related to the d_{z^2-r} and $d_{x^2-y^2}$ orbital of V make the main contribution to the transmission. In the case of electrodes with antiparallel magnetization, the VBz wire has non-collinear magnetic structure with larger magnetic moments on the V atoms in comparison to the collinear solution. We have also found that the zero bias conductance for the non-collinear domain wall in the V_4Bz_5 chain is about 1.5 times larger then for the collinear one.

Bibliography

[1] A. Aviram, M.A. Ratner, Chem. Phys. Lett. **29**, 277 (1974).

[2] T.J. Kealy, P.L. Pauson, Nature (London) **168**, 1039 (1951).

[3] R. Kubo and K. Tomita: J. Phys. Soc. Japan, **9**, 888 (1954).

[4] R. Kubo, J. Phys. Soc. Japan, **12**, 570 (1957).

[5] S. Onoda, N. Sugimoto and N. Nagaosa, Progress of Theoretical Physics, **116**, 61 (2006).

[6] L. V. Keldysh, JETP **20**, 1018 (1965).

[7] R.van Leeuwen, N.E.Dahlen, G.Stefanucci, C.-O.Almbladh and U.von Barth, Lecture Notes in Physics N706: Time-Dependent Density Functional Theory, Springer, (2006).

[8] S. Datta, Electronic Transport in Mesoscopic Systems, Cambridge University Press, Cambridge, (1997).

[9] R. Landauer, IBM J. Res. Dev. **1**, 233 (1957); R. Landauer, Philos. Mag. **21**, 863 (1970).

[10] R.A. de Groot, F.M. Mueller, P.G. van Engen and K.H.J. Buschow, Phys. Rev. Lett., **50**, 2024 (1983).

[11] C. Heiliger, P. Zahn, B.Yu. Yavorsky, and I. Mertig, Phys. Rev. B, **77**, 224407 (2008).

[12] I. Rungger, O. Mryasov, and S. Sanvito, Phys. Rev. B, **79**, 094414 (2009).

[13] N. Néel, J. Kröger, L. Limot, T. Frederiksen, M. Brandbyge, and R. Berndt, Phys. Rev. Lett., **98**, 065502 (2007).

[14] T. Frederiksen, M. Paulsson, M. Brandbyge, A.-P. Jauho, Phys. Rev. B, **75**, 205413, (2007).

[15] M. Paulsson, T. Frederiksen, H. Ueba, N. Lorente, and M. Brandbyge, Phys. Rev. Lett., **100**, 226604 (2008).

[16] K. Tsukagoshi, B.W. Alphenaar, and H. Ago, Nature, **401**, 572 (1999).

[17] A.R. Rocha, V.M. García-Suárez, S.W. Bailey, C.J. Lambert, J. Ferrer and S. Sanvito, Nature Materials, **4**, 335 (2005).

[18] R. Liu, S.-H. Ke, H.U. Baranger, and W. Yang, NanoLetters, **5**, 1959 (2005).

[19] V.V. Maslyuk, A. Bagrets, V. Meded, A. Arnold, F. Evers, M. Brandbyge, T. Bredow, I. Mertig, Phys. Rev. Lett., **97**, 097201 (2006).

[20] M. Koleini, M. Paulsson, and M. Brandbyge, Phys. Rev. Lett. **98**, 197202 (2007).

[21] Ph. Kurz, G. Bihlmayer, K. Hirai, and S. Blügel, Phys. Rev. Lett.**86**, 1106 (2001).

[22] D. Hobbs, G. Kresse, and J. Hafner, Phys. Rev. B **62**, 11556 (2000).

[23] T. Oda, A. Pasquarello, and R. Car, Phys. Rev. Lett. **80**, 3622 (1998).

[24] L.M. Sandratskii, Adv. Phys. **91**, 47 (1998).

[25] L. Nordström, D.J. Singh, Phys. Rev. Lett. **76**, 4420 (1996).

[26] A. Bergman, L. Nordström, A. B. Klautau, S. Frota-Pessôa and O. Eriksson, Phys. Rev. B **75**, 224425 (2007).

[27] J. Korringa, Physica, **13**, 392 (1947).

[28] W. Kohn, N. Rostoker, Phys. Rev. **94**, 1111 (1954).

[29] L.M. Sandratskii, Phys. Stat. Sol. (b) **135**, 167 (1986).

[30] S.V. Faleev, F Léonard, D.A. Stewart, and M. van Schilfgaarde, Phys. Rev. B **71**, 195422 (2005)

[31] M. Czerner, B.Yu. Yavorsky, and I. Mertig , Phys. Rev. B **77**, 104411 (2008)

[32] P. Ordejón, E. Artacho and J. M. Soler, Phys. Rev. B, **53**, 10441 (1996).

[33] D. Sánchez-Portal, P. Ordejón, E. Artacho and J. M. Soler, Int. J. Quantum Chem., **65**, 453 (1997).

[34] J.M. Soler, E. Artacho, J.D. Gale, A. García, J. Junquera, P. Ordejón and D. Sánchez-Portal, J. Phys.: Condens. Matter, **14**, 2745 (2002).

[35] E. Fermi, Z. Phys., **48**, 73, (1928).

[36] L.H. Thomas, Proc. Cambridge Philos. Soc., **23**, 542 (1927).

[37] P. Hohenberg and W. Kohn, Phys. Rev. B, **136**, B864, (1964).

[38] W. Kohn and L. J. Sham, Phys. Rev., **140**, A1133 (1965).

[39] U. von Barth and L. Hedin, J. Phys. C: Solid State Phys., **5**, 1629 (1972).

[40] K. Capelle and G. Vignale, Phys. Rev. Lett., **86**, 5546 (2000).

[41] H. Eschrig and W.E. Pickett, Solid State Commun., **118**, 123 (2001).

[42] W. Kohn, A. Savin, and C.A. Ullrich, Int. J. Quantum Chem., **100**, 20 (2004).

[43] S. H. Vosko, L. Wilk, and M. Nusair, Can. J. Phys., **58**, 1200 (1980).

[44] D.M. Ceperley and B.J. Alder. Phys. Rev. Lett., **45**, 566, (1980).

[45] J. P. Perdew and A. Zunger, Phys. Rev. B, **23**, 5048 (1981).

[46] J. P. Perdew and A. Zunger, Phys. Rev. B, **23**, 5048 (1981).

[47] J. P. Perdew and Y. Wang, Phys. Rev. B, **33**, 8800 (1986).

[48] J. P. Perdew and Y. Wang, Phys. Rev. B, **40**, 3399 (1989).

[49] J. P. Perdew, Phys. Rev. B, **33**, 8822 (1986).

[50] A. D. Becke, Phys. Rev. A, **38**, 3098 (1988).

[51] C. Lee, W. Yang, and R. G. Parr, Phys. Rev. B, **37**, 785 (1988).

[52] J. P. Perdew, K. Burke, and M. Ernzerhof, Phys. Rev. Lett., **77**, 3865 (1996).

[53] A. D. Boese and N. C. Handy, J. Chem. Phys., **114**, 5497 (2001).

[54] B. G. Johnson, P. M. W. Gill, and J. A. Pople, J. Chem. Phys. **97**, 7846 (1992); **98**, 5612 (1993).

[55] A. D. Becke, J. Chem. Phys., **98**, 5648 (1993).

[56] J. Paier, M. Marsman, and G. Kresse, J. Chem. Phys., **127**, 024103 (2007).

[57] J.E. Lennard-Jones, Transactions of the Faraday Society, **25**, 668 (1929)

[58] C.C.J. Roothaan, Reviews of Modern Physics, **23**, 69, (1951)

[59] J.C. Slater, Phys. Rev., **36**, 57 (1930).

[60] S.F. Boys, Proc. R. Soc. London Ser. A, **200**, 542 (1950).

[61] D.R. Hamann, M. Schlüter and C. Chiang, Phys. Rev. Lett., **43**, 1494 (1979).

[62] O.F. Sankey and D.J. Niklewski, Phys. Rev. B, **40**, 3979 (1989).

[63] D. Sánchez-Portal, J. M. Soler, and E. Artacho, J. Phys.: Condens. Matter, **8**, 3859 (1996).

[64] E. Artacho, D. Sánchez-Portal, P. Ordejón, A. García, and J. M. Soler, Phys. Status Solidi B, **215**, 809 (1999).

[65] L. Kleinman and D.M. Bylander, Phys. Rev. Lett., **48**, 1425 (1982).

[66] D. Vanderbilt, Phys. Rev. B, **32**, 8412 (1985).

[67] J. Perdew and A. Zunger, Phys. Rev. B **23**, 5048 (1981).

[68] V. I. Anisimov, J. Zaanen, and O. K. Andersen, Phys. Rev. B **44**, 943 (1991); A. I. Liechtenstein, V. I. Anisimov, and J. Zaanen, Phys. Rev. B **52**, R5467 (1995).

[69] P. Novák, J. Kuneá, L. Chaput, and W. E. Pickett, Phys. Stat. Sol. (B) **243**, 563 (2006).

[70] L. Fernandez-Seivane, M. A. Oliveira, S. Sanvito, and J. Ferrer, J. Phys C: Cond. Matt. **18**, 7999 (2006).

[71] J. Kübler, K.H. Höck, and J. Sticht, J. Appl. Phys. **63**, 3482 (1988).

[72] J. Kübler, K.H. Höck, J. Sticht, and A.R. Williams, J. Phys. F: Met. Phys. **18**, 469 (1988).

[73] V.M. García-Suárez, C.M. Newman, C.J. Lambert, J.M. Pruneda, and J. Ferrer, Eur. Phys. J. B, **40**, 371 (2004).

[74] K. Knöpfle, L.M. Sandratskii, and J. Kübler, Phys. Rev. B, **62**, 5564 (2000).

[75] N. Troullier and J. L. Martins, Phys. Rev. B, **43**, 1993 (1991).

[76] S.G. Louie, S. Froyen, and M.L. Cohen, Phys. Rev. B, **26**, 1738 (1982).

[77] V. R. Saunders, R. Dovesi, C. Roetti, R. Orlando, C. M. Zicovich-Wilson, N. M. Harrison, K. Doll, B. Civalleri, I. Bush, Ph. D'Arco, M. Llunell, CRYSTAL2003 User's Manual, University of Turin, Turin, 2003.

[78] A. Schläfer, C. Huber and R. Ahlrichs; J. Chem. Phys., **100**, 5829 (1994).

[79] T. Nautiyal, T.H. Rho, K.S. Kim, Phys. Rev. B **69**, 193404 (2004).

[80] D. Spisak and J. Hafner, Phys. Rev. B **65**, 235405 (2002).

[81] J.C. Tung and G.Y. Guo, Phys. Rev. B, **76**, 094413 (2007).

[82] G. Autès, C. Barreteau, D. Spanjaard and M.-C. Desjonquères, J. Phys.: Condens. Matter, **18**, 6785 (2006).

[83] R.F.W. Bader, Atoms in Molecules, (Clarendon Press, Oxford, 1990).

[84] R.F.W. Bader, Chem. Rev. (Washington, D.C.) **91**, 893 (1991).

[85] R.S. Mulliken, J. Chem. Phys. **36**, 3428 (1962)

[86] R.S. Mulliken, W.C. Ermler, Diatomic molecules: Result of ab initio calculations (Academic Press, New York, 1977)

[87] P.-O. Löwdin, Adv. Quantum Chem. **5**, 185 (1970).

[88] A.E. Reed, L.A. Curtiss, and F. Weinhold, Chem. Rev. (Washington, D.C.) **88**, 899 (1988).

[89] L. Gagliardi, R. Lindh, and G. Karlstrom, J. Chem. Phys. **121**, 4494 (2004).

[90] A.J. Stone, Chem. Phys. Lett. **83**, 233 (1981).

[91] M. Takahashi, J. Phys. C, **10**, 1289 (1977).

[92] A. H. MacDonald, S. M. Girvin, and D. Yoshioka, Phys. Rev. B **37**, 9753 (1988).

[93] I.N. Silin, FORTRAN program library (Dubna, JINR, D-520, 1970).

[94] R.C. Longo, M.M.G. Alemany, J. Ferrer, A. Vega, L.J. Gallego, J. Chem. Phys. **128**, 114315 (2008).

[95] S.K. Nayak, P. Jena, Chem.Phys.Lett. **289** 473 (1998).

[96] P. Bobadova-Parvanova, K.A. Jackson, S. Srinivas, M. Horoi, J. Chem. Phys. **122**, 014310 (2005).

[97] G.L. Gutsev, M.D. Mochena, and C.W. Bauschlicher, J. Phys. Chem. A, **110**, 9758 (2006).

[98] M.R. Pederson, F. Reuse, S.N. Khanna, Phys. Rev. B **58**, 5632 (1998).

[99] J. Mejía-López, A.H. Romero, M.E. Garcia, J.L. Morán-López, Phys. Rev. B **74**, 140405(R) (2006).

[100] S. Lounis, P. Mavropoulos, R. Zeller, P.H. Dederichs, and S. Blügel, Phys. Rev. B **75**, 174436 (2007).

[101] A. Bergman, L. Nordström, A. B. Klautau, S. Frota-Pessôa and O. Eriksson, Phys. Rev. B **73**, 174434 (2006).

[102] R.H. Friend, R.W. Gymer, A.B. Holmes, J.H. Burroughes, R.N. Marks, C. Taliani, D.D.C. Bradley, D.A. Dos Santos, J.L. Bredas, M. Lögdlund, and W. R. Salaneck, Nature (London) **397**, 121 (1999).

[103] W. Clemens, W. Fix, J. Ficker, A. Knobloch, and A. Ullmann, J. Mater. Research **19**, 1963 (2004).

[104] G. Horowitz, J. Mater. Research **19**, 1946 (2004).

[105] H. Hoppe and N.S. Sariciftci, J. Mater. Research **19**, 1924 (2004).

[106]   S.R. Forrest, Chem. Rev. **97**, 1793 (1997), and references therein.

[107]   T. Kurikawa, H. Takeda, M. Hirano, K. Judai, T. Arita, S. Nagao, A. Nakajima, K. Kaya, Organometallics, **18**, 1430 (1999).

[108]   A. Nakajima, K. Kaya, J. Phys. Chem. A, **104**, 176 (2000).

[109]   K. Miyajima, A. Nakajima, S. Yabushita, M.B. Knickelbein, K. Kaya, J. Am. Chem. Soc. **126**, 13202 (2004).

[110]   K. Miyajima, M.B. Knickelbein, A. Nakajima, Eur. Phys. J. D **34**, 177 (2005).

[111]   K. Miyajima, S. Yabushita, M.B. Knickelbein, A. Nakajima, J. Am. Chem. Soc., **129**, 8473 (2007).

[112]   H. Xiang, J. Yang, J.G. Hou, Qingshi Zhu, J. Am. Chem. Soc. **128**, 2310 (2006).

[113]   V.R. Saunders, R. Dovesi, C. Roetti, R. Orlando, C.M. Zicovich-Wilson, N.M. Harrison, K. Doll, B. Civalleri, I. Bush, Ph. D'Arco, M. Llunell CRYSTAL2003 User's Manual, (University of Turin, Turin, 2003).

[114]   R. Krishnan, J.S. Binkley, R. Seeger and J.A. Pople, J. Chem. Phys. **72**, 650 (1980).

[115]   A. Schäfer, C. Huber and R. Ahlrichs, J. Chem. Phys., **100**, 5829 (1994); (ftp://ftp.chemie.uni-karlsruhe.de/pub/basen).

[116]   W.J. Hehre, R. Ditchfield and J.A. Pople, J. Chem. Phys. **56**, 2257 (1972).

[117]   A. Schäfer, H. Horn and R. Ahlrichs, J. Chem. Phys. **97**, 2571 (1992); Basis sets were obtained from the Extensible Computational Chemistry Environment Basis Set Database, Version 02/02/06.

[118]   W.J. Stevens, M.Krauss, H.Basch, P.G.Jasien, Can. J.Chem. **70**, 612 (1992).

[119]   B. Civalleri, Ph. D'Arco, R. Orlando, V.R. Saunders, R. Dovesi, Chem. Phys. Lett. **348**, 131 (2001).

[120]   V.Yu. Aristov, O.V. Molodtsova, V. Maslyuk, D.V. Vyalikh, V.M. Zhilin, Yu.A. Ossipyan, T. Bredow, I. Mertigc and M. Knupfer, Appl. Surf. Sci. **254**, 20 (2007).

[121]   V.Yu. Aristov, O.V. Molodtsova, V.V. Maslyuk, D.V. Vyalikh, V.M. Zhilin, Yu.A. Ossipyan, T. Bredow, I. Mertig, M. Knupfer, J. Chem. Phys. **128**, 034703 (2008).

[122]   O.V. Molodtsova, M. Knupfer, V.V. Maslyuk, D.V. Vyalikh, V.M. Zhilin, Y.A. Ossipyan, T. Bredow, I. Mertig, V.Yu. Aristov, J. Chem. Phys. **129**, 154705 (2008).

[123] V.V. Maslyuk, V.Y. Aristov, O.V. Molodtsova, D.V. Vyalikh, V.M. Zhilin, Y.A. Ossipyan, T. Bredow, I. Mertig, M. Knupfer, Appl. Phys. A **94**, 485 (2009).

[124] S. I. Fedoseenko, D. V. Vyalikh, I. E. Iossifov, R. Follath, S. A. Gorovikov, R. Püttner, J.-S. Schmidt, S. L. Molodtsov, V. K. Adamchuk, W. Gudat, and G. Kaindl, Nucl. Instr. and Meth. in Phys. Res. A **505**, 718 (2003).

[125] V. Yu. Aristov, O. V. Molodtsova, V. M. Zhilin, D. V. Vyalikh, and M. Knupfer, Phys. Rev. B **72**, 165318 (2005).

[126] S.R. Forrest, Chem. Rev. 97, 1793 (1997), and references therein.

[127] H. Peisert, M. Knupfer, T. Schwieger, J. M. Auerhammer, M. S. Golden, and J. Fink, J. Appl. Phys. **91**, 4872 (2002).

[128] O.V. Molodtsova, V.M. Zhilin, D.V. Vyalikh, V.Yu. Aristov , M. Knupfer, J. Appl. Phys. **98**, 093702 (2005).

[129] L. Lozzi, S. Santucci, S. La Rosa, B. Delley, and S. Picozzi, J. Chem. Phys. **121**, 1883 (2004).

[130] M. Ashida, M. Uyeda and E. Suito, J. Cryst. Growth, **8**, 45 (1971).

[131] A. Hoshino, Y. Takenaka and H. Miyaji, Acta Cryst. **B59**, 393 (2003).

[132] P. Erk, H. Hengelsberg, M.F. Haddowb and R. van Gelder, Cryst.Eng.Comm, **6**, 474 (2004).

[133] K. T. Park, A. Miller, K. Klier, R. L. Opila and J. E. Rowe, Surf. Sci. Lett. **529**, L285 (2003); T. S. Ellis, K. T. Park, S. L. Hulbert, M. D. Ulrich, J. E. Rowe, J. Appl. Phys. **95**, 982 (2004).

[134] T. Schwieger, H. Peisert1, M. S. Golden, M. Knupfer, and J. Fink, Phys. Rev. B, **66**, 155207 (2002).

[135] I. G. Hill, A. Kahn, Z. G. Soos, and R. A. Pascal, Jr., Chem. Phys. Lett. **327**, 181 (2000).

[136] M.-S. Liao, S. Scheinera, J. Chem. Phys. **114**, 9780 (2001).

[137] B. Białek, In G. Kim, J. Il Lee, Thin Solid Films **436**, 107 (2003).

[138] X-ray Photoelectron Spectroscopy (XPS) Database, Version 3.4 (http://srdata.nist.gov/xps/).

[139] O.V. Molodtsova, M. Knupfer, Yu.A. Ossipyan, V.Yu. Aristov, J. Appl. Phys. in press (2008).

[140] S.R. Forrest, Chem. Rev. **97**, 1793 (1997), and references therein.

[141] V.Yu. Aristov., O.V. Molodtsova, V. Maslyuk, D.V. Vyalikh, V.M. Zhilin, Yu. A. Ossipyan, T. Bredow, I. Mertig, M. Knupfer, J. Chem. Phys., **128**, 034703 (2008).

[142] S.L. Dudarev, G.A. Botton, S.Y. Savrasov, C.J. Humphreys, and A.P. Sutton, Phys. Rev. B 57, 1505 (1998).

[143] P.E. Blöchl, Phys. Rev. B 50, 17 953 (1994).

[144] G. Kresse, J. Hafner, Phys. Rev. B 47, 558(R) (1993); G. Kresse and J. Furthmüller, Phys. Rev. B 54, 11169 (1996)

[145] R. Pandey, B.K. Rao, P. Jena, M.A. Blanco, J. Am. Chem. Soc., **123**, 3799 (2001); J. Am. Chem. Soc., **123**, 7744 (2001).

[146] A.K. Kandalam, B.K. Rao, P. Jena, R. Pandey, J. Chem. Phys., **120**, 10414 (2004).

[147] X. Zhang, J. Wang, J. Phys. Chem. A, **112**, 296 (2008).

[148] J. Wang, L. Zhu, X. Zhang, M. Yang, J. Phys. Chem. A, **112**, 8226 (2008).

[149] B.K. Rao, P. Jena, J. Chem. Phys. **116**, 1343 (2002);

[150] B.K. Rao, P. Jena, J. Chem. Phys. **117**, 5234 (2002).

[151] J. Kua, K.M. Tomlin, J. Phys. Chem. A, **110**, 11988 (2006).

[152] T. Yasuike, A. Nakajima, S. Yabushita, K. Kaya, J. Phys. Chem. A, Vol. **101**, 5360 (1997).

[153] F. Rabilloud, J. Chem. Phys. **122**, 134303 (2005).

[154] S. Kambalapalli, J.V. Ortiz. J. Phys. Chem. A, **108**, 2988 (2004).

[155] P.k Chaquin, D. Costa, C. Lepetit, M. Che, J. Phys. Chem. A, **105**, 4541 (2001).

[156] M.P. Andrews, S.M. Mattar, G.A. Ozin, J. Phys. Chem. **90**, 744 (1986).

[157] M.P. Andrews, S.M. Mattar, G.A. Ozin, J. Phys. Chem. **90**, 1037 (1986).

[158] F.G.N. Cloke, A.N. Dix, J.C. Green, R.N. Perutz, E.A. Seddon, Organometallics, **2**, 1150 (1983).

[159] K. Hoshino, T. Kurikawa, H. Takeda, A. Nakajima, K. Kaya, J. Phys. Chem., **99**, 3053 (1995).

[160] T. Kurikawa, M. Hirano, H. Takeda, K. Yagi, K. Hoshino, A. Nakajima, K. Kaya, J. Phys. Chem., **99**, 16248 (1995).

[161]   D. Rayane, A.-R. Allouche, R. Antoine, M. Broyer, I. Compagnon, P. Dugourd, Chem. Phys. Lett., **375**, 506 (2003).

[162]   L. Shen, S.-W. Yang, M.-F. Ng, V. Ligatchev, L. Zhou, Y. Feng, J. Am. Chem. Soc., **130**, 13956 (2008).

[163]   R.F.W. Bader, *Atoms in molecules: a quantum theory.* Oxford University Press, New York, 1990

[164]   J. Wang, P.H. Acioli, J. Jellinek, J. Am. Chem. Soc. **127**, 2812 (2005).

[165]   R. Muhida1, W. A. Diňo, Md.M. Rahman, H. Kasai and H. Nakanishi, J. Phys. Soc. Jpn. **73** 2292 (2004).

[166]   Y. Mokrousov, N. Atodiresei, G. Bihlmayer, S. Heinze, S. Blügel, Nanotechnology, **18**, 495402 (2007).

[167]   D.A. Greenwood, Proc. Phys. Soc., **71** (1958) 585.

[168]   I. Mertig, R. Zeller, and P.H. Dederichs, Phys. Rev. B, **47**, 16178 (1993)

[169]   J. Taylor, H. Guo, J. Wang, Phys. Rev. B, **63**, 245407 (2001)

[170]   M. Brandbyge, J.-L. Mozos, P. Ordejon, J. Taylor, K. Stokbro, Phys. Rev. B, **65**, 165401 (2002).

[171]   Y. Xuea, S. Datta, M.A. Ratner, Chemical Physics, **281**, 151 (2002).

[172]   E. Louis, J.A. Vergés, J.J. Palacios, A.J. Pérez-Jiménez, E. SanFabián, Phys. Rev. B, **67**, 155321 (2003).

[173]   D. Jacob, Ph.D. thesis, Universidad de Alicante, (2007)

[174]   S.-H.Ke, H.U. Baranger, W. Yang, Phys. Rev. B, **70**, 085410 (2004).

[175]   A.R. Rocha, V.M. García-Suárez, S.W. Bailey, C. Lambert, J. Ferrer, S. Sanvito, Phys. Rev. B, **73**, 085414 (2006).

[176]   A.R. Rocha, Ph.D. thesis, Trinity College Dublin (2007).

[177]   M. Paulsson, cond-mat/0210519 (unpublished).

[178]   M. Büttiker, Y. Imry, R. Landauer, S. Pinhas, Phys. Rev. B, **31**, 6207 (1985).

[179]   V.S. Vladimirov, Equations of Mathematical Physics. New York: Dekker, 1971.

[180]   L. Szunyogh, P. Wenberger, J. Phys..: Condens. Matter, **11**, 10451 (1999).

[181]   P. Bruno, Phys. Rev. Lett., **83** 2425 (1999).

[182] M. Pratzer, H.J. Elmers, M. Bode, O. Pietzsch, A. Kubetzka, R. Wiesendanger, Phys. Rev. Lett., **87** 127201 (2001).

[183] J. Prokop, A. Kukunin, and H. J. Elmers, Phys. Rev. Lett., **95**, 187202 (2005)

[184] G. Autès, C. Barreteau, D. Spanjaard, M.-C. Desjonquères, J. Phys.: Condens. Matter **18**, 6785 (2006).

[185] G. Autès, C. Barreteau, D. Spanjaard, M.-C. Desjonquères, Phys. Rev. B, **77**, 155437 (2008).

[186] J.D. Burton, R.F. Sabirianov, S.S. Jaswal, E.Y. Tsymbal, O.N. Mryasov, Phys. Rev. Lett., **97**, 077204 (2006).

[187] P. Levi, A. Fert, Phys. Rev. Lett., **97**, 097205 (2006).

[188] P. Levi, A. Fert, Phys. Rev. B, **74**, 224446 (2006).

[189] F. Mittendorfer and J. Hafner, Surface Science, **472** 133 (2001).

[190] M. Paulsson, M. Brandbyge, Phys. Rev. B, **76**, 115117 (2007).

Acknowledgements

Eidesstattliche Erklärung

Hiermit erkläre ich gemäß §5 Abs. 2b der Promotionsordnung der Mathematisch-Naturwissenschaftlich-Technischen Fakultät der Martin-Luther-Universität Halle-Wittenberg vom November 13, 2009, daß ich die vorliegende Arbeit

Simulation of the electronic transport through organometallic molecules

selbständig und ohne fremde Hilfe verfaßt, andere als die von mir angegebenen Quellen und Hilfsmittel nicht benutzt und die den benutzten Werken wörtlich oder inhaltlich entnommenen Stellen als solche kenntlich gemacht habe.

Halle (Saale), den July 6, 2009

Volodymyr Maslyuk